

**UCGE Reports  
Number 20316**

Department of Geomatics Engineering

**Implementation of a Close Range Photogrammetric  
System for 3D Reconstruction of a Scoliotic Torso**

(URL: <http://www.geomatics.ucalgary.ca/graduatetheses>)

**by**

**Ivan Denislavov Detchev**

**September 2010**



UNIVERSITY OF CALGARY

IMPLEMENTATION OF A CLOSE RANGE PHOTOGRAMMETRIC SYSTEM FOR  
3D RECONSTRUCTION OF A SCOLIOTIC TORSO

by

IVAN DENISLAVOV DETCHEV

A THESIS

SUBMITTED TO THE FACULTY OF GRADUATE STUDIES  
IN PARTIAL FULFILMENT OF THE REQUIREMENTS FOR THE  
DEGREE OF MASTER OF SCIENCE

DEPARTMENT OF GEOMATICS ENGINEERING

CALGARY, ALBERTA

SEPTEMBER, 2010

© IVAN DENISLAVOV DETCHEV 2010

## **Abstract**

Scoliosis is a deformity of the human spine most commonly encountered with children. After being detected, periodic examinations via x-rays are traditionally used to measure its progression. However, due to the increased risk of cancer, a non-invasive and radiation-free scoliosis detection and progression monitoring methodology is needed. Quantifying the scoliotic deformity through the torso surface is a valid alternative, because of its high correlation with the internal spine curvature. This work proposes a low-cost multi-camera photogrammetric system for semi-automated 3D reconstruction of a torso surface with sub-millimetre level accuracy. The thesis describes the system design and calibration for optimal accuracy. It also covers the methodology behind the reconstruction and registration procedures. The experimental results include the complete reconstruction of a scoliotic torso mannequin. The final accuracy is evaluated through the goodness of fit between the reconstructed surface and a more accurate set of points measured by a coordinate measuring machine.

## Acknowledgements

First of all, I am very thankful to my supervisor, Dr. Ayman Habib, who willingly accepted me as a graduate student on a short notice and has been guiding me through my studies for the last three years. Second, this thesis would have not been possible if it was not for Bruce Wright, who helped me with the system hardware. I am also grateful to David Chang, who started the project and was always there to answer any of my questions on the software side. I am indebted to three individuals who took the time to assist me with the camera calibration board: Ken Fortney (construction), Bozhidar Marinov (painting), and Axel Ebeling (surveying). I also would like to thank another three individuals who posed for the face reconstruction experiment: Alif Zaman, Stephanie Coupal, and Sanam Jamtsho. In addition, I would like to show my gratitude to Dr. Derek Lichti for answering my questions related to photogrammetry and laser scanning, and Ki In Bang for giving me helpful programming tips. Also, it has been a pleasure to work with my colleagues: Dr. Changjae Kim (a.k.a. CJ), Anna Jarvis, Eunju Kwak, Anna Paula and Juliano Kersting, Erwan Renaudin, Dr. Ruifang Zhai, Mohannad Al-Dugham, and Jacky Chow. Last but not least, I am thankful to Lu-Anne Markland for keeping me on top of my deadlines, and Garth Wannamaker for being kind when signing out equipment. I would also like to mention my instructors from the University of New Brunswick without whom I would not have made it to graduate school: Dr. Sue Nichols, Dr. Yun Zhang, Dr. David Coleman, Dr. Kevin Pegler, Dr. Marcelo Santos, Dr. James Secord, Petra Menz, Rick Wightman, Dr. Jason Bond, Dr. Mustafa Berber, and Dr. Jonathan Beaudoin.

## **Dedication**

I dedicate this thesis to my sister Miroslava, who has always inspired me academically.

## Table of Contents

Approval Page.....	ii
Abstract.....	iii
Acknowledgements.....	iv
Dedication.....	v
Table of Contents.....	vi
List of Tables.....	viii
List of Figures.....	x
List of Abbreviations.....	xv
CHAPTER ONE: INTRODUCTION.....	1
1.1 Background information on scoliosis.....	1
1.2 Research objectives.....	7
1.3 Thesis outline.....	8
CHAPTER TWO: LITERATURE REVIEW.....	10
2.1 Torso surface measurements for estimating the spinal deformity.....	10
2.2 Brief history of surface measurements for scoliotic torsos.....	13
2.3 Commercially available systems for 3D reconstruction.....	15
2.3.1 Time-of-flight systems.....	15
2.3.2 Triangulation systems.....	18
2.3.3 Summary of the commercially available systems for 3D reconstruction.....	22
2.4 Custom-built photogrammetric systems for 3D reconstruction.....	25
2.5 Summary of the literature review.....	27
CHAPTER THREE: PROPOSED SYSTEM DESIGN.....	29
3.1 Proposed system setup.....	29
3.2 System calibration.....	31
3.2.1 Camera calibration and stability analysis.....	31
3.2.2 Exterior orientation parameter estimation.....	41
3.3 Camera synchronization and pattern projection.....	42
3.4 Balance between intersection accuracy and matching reliability.....	47
3.5 Summary of the proposed system design.....	50
CHAPTER FOUR: PROCESSING METHODOLOGY.....	52
4.1 Surface reconstruction.....	53
4.1.1 Corner detection and image matching.....	54
4.1.1.1 Epipolar resampling.....	56
4.1.1.2 Hierarchical matching strategy.....	57
4.1.2 Tracking and intersection.....	61
4.2 Surface registration.....	62
4.2.1 Pairwise surface registration.....	66
4.2.1.1 Coplanarity constraint method for the pairwise surface registration.....	68
4.2.1.2 Modified weight matrix method for the pairwise surface registration.....	71
4.2.2 Multiple surface registration.....	76
4.2.2.1 Coplanarity constraint method for the multiple surface registration.....	78

4.2.2.2 Modified weight matrix method for the multiple surface registration...	79
4.3 Summary of the processing methodology .....	80
<b>CHAPTER FIVE: SYSTEM IMPLEMENTATION AND EXPERIMENTAL</b>	
<b>RESULTS .....</b>	<b>82</b>
5.1 Camera calibration .....	82
5.1.1 Surveying the portable calibration board .....	83
5.1.2 Image collection for the camera calibration .....	84
5.1.3 Test on the choice for a distortion model .....	86
5.1.4 Test on the choice for image space observations .....	89
5.1.5 Test on the choice for datum definition.....	91
5.1.6 Camera calibration findings .....	92
5.2 Camera stability analysis .....	92
5.3 Sensor arm setup and exterior orientation parameters determination.....	93
5.4 Flat metal plate reconstruction.....	96
5.5 Human face reconstruction .....	98
5.6 Artificial torso mannequin reconstruction .....	102
5.6.1 Single projector torso reconstruction.....	102
5.6.2 Dual projector torso reconstruction .....	114
5.6.3 Test on the coplanarity constraint vs. the modified weight matrix methods.	120
5.7 Summary of the experimental results .....	125
<b>CHAPTER SIX: CONCLUSIONS AND RECOMMENDATIONS FOR FUTURE</b>	
<b>WORK .....</b>	<b>127</b>
6.1 Conclusions.....	129
6.2 Recommendations for future work .....	131
<b>REFERENCES .....</b>	<b>132</b>

## List of Tables

Table 2.1 Comparison of commercially available systems regarding the 3D reconstruction of a human torso.....	23
Table 3.1 Binary encoding and corresponding images for the 3 x 3 pixel block patterns used.....	44
Table 5.1 A-posteriori variance factors and RMSE of the bundle similarity in the calibration results for using all six distortion parameters against using only $k_1$ .....	87
Table 5.2 RMSE between photogrammetric reconstruction and surveying measurements for calibration results when using all six distortion parameters against using only $k_1$ ; all units are mm.....	88
Table 5.3 IOP differences for using tie points only against using tie points and linear features.....	90
Table 5.4 RMSE between photogrammetric reconstruction and surveying measurements for calibration results when using points only against using points and linear features as observations; all units are mm.....	90
Table 5.5 IOP differences for using control points against using distance constraints ....	91
Table 5.6 Example of two sets of camera calibration results for the same camera.....	93
Table 5.7 Stability results for the two calibration sets for all the cameras.....	93
Table 5.8 Number of points in the four reconstructed surfaces for the new dataset compared to the ones published in Chang (2008) and Chang <i>et al.</i> (2009).....	107
Table 5.9 Goodness of fit after the pairwise registration for the four reconstructed surfaces in the new dataset compared to the ones published in Chang (2008) and Chang <i>et al.</i> (2009); the number of matched point-patch pairs in the overlapping areas is shown in brackets.....	107
Table 5.10 Goodness of fit after the multiple-surface registration for the four reconstructed surfaces in the new dataset compared to the ones published in Chang (2008) and Chang <i>et al.</i> (2009).....	107
Table 5.11 Estimated normal distances between the 25 centroid targets and their corresponding patches.....	113
Table 5.12 Summary of the absolute accuracy evaluation for the new dataset compared to the previous ones published in Chang (2008) and Chang <i>et al.</i> (2009).....	113

Table 5.13 Number of points in the reconstructed surfaces for the datasets with dual projector compared to the one with a single projector.....	116
Table 5.14 Goodness of fit after the pairwise registration for the four reconstructed surfaces in the datasets with dual projector compared to the ones with a single projector; the number of matched point-patch pairs in the overlapping areas is shown in brackets.....	117
Table 5.15 Goodness of fit after the multiple-surface registration for the four reconstructed surfaces in the datasets with dual projector compared to the ones with a single projector.....	117
Table 5.16 Summary of the absolute accuracy evaluation for the dual projector datasets compared to the one with a single projector.....	118
Table 5.17 Estimated normal distances between the 25 centroid targets and their corresponding patches for the dual projector datasets .....	118
Table 5.18 Transformation parameters and their standard deviations after multiple surface registration using the coplanarity constraint for the July dataset .....	122
Table 5.19 Transformation parameters and their standard deviations after multiple surface registration using the modified weight matrix constraint for the July dataset .....	122
Table 5.20 RMSE between point clouds registered by the coplanarity constraint and the modified weight matrix methods for the July dataset .....	123
Table 5.21 Transformation parameters and their standard deviations after multiple surface registration using the coplanarity constraint for the October dataset.....	124
Table 5.22 Transformation parameters and their standard deviations after multiple surface registration using the modified weight matrix constraint for the October dataset .....	124
Table 5.23 RMSE between point clouds registered by the coplanarity constraint and the modified weight matrix methods for the October dataset.....	124

## List of Figures

Figure 1.1 Lateral (left) and posterior (right) views for the regions of the spine .....	1
Figure 1.2 Scoliotic spine (left) vs. normal spine (right).....	2
Figure 1.3 Rib cage deformity (a), and other visible symptoms of scoliosis (b).....	2
Figure 1.4 Adams forward bend test (a), and the use of a scoliometer (b).....	4
Figure 1.5 Spinal x-ray (a), and measurement of the Cobb angle (b).....	5
Figure 1.6 Examples of a Boston brace (a), and a Milwaukee brace (b).....	5
Figure 2.1 Two examples of the correlation between the torso surface deformity (a, c) and the internal spinal curvature (b, d) .....	12
Figure 2.2 Examples of Moiré topography (a), and rasterstereography (b).....	14
Figure 2.3 Examples of pulse-based (a), and phase-based (b, c) laser ranging .....	17
Figure 2.4 Trimble GX 3D Scanner (a), Leica HDS6100 (b), and SwissRanger SR4000 (c) .....	18
Figure 2.5 Setup of a triangulation scanning system .....	19
Figure 2.6 Linear scanner setup (a) and an encoded block pattern with a different resolution (b).....	21
Figure 2.7 InSpeck 3D Mega Capturor II (a), Konica Minolta VIVID 9i (b), and Polhemus FastSCAN Scorpion (c).....	22
Figure 2.8 Traditional stereo photography setup .....	25
Figure 3.1 Sensor arm prototype comprised of a projector and multiple cameras rotating vertically through a swivel mechanism (a); design of system setup comprised of four sensor arms (b) .....	30
Figure 3.2 Patient entering the system (a), and patient being ready for data acquisition (b) .....	31
Figure 3.3 Illustration of the principal point offset (a); example of the collinearity condition and the relation between the object and the image space coordinate systems (b) .....	32
Figure 3.4 Examples of pincushion (a), and barrel (b) lens distortion .....	34
Figure 3.5 Examples of cross (a), circle (b), and checker-board (c) signaled targets....	36

Figure 3.6 Examples of control point (a-b), and distance measurement (c-d) distribution in the image format.....	36
Figure 3.7 Examples of 2D (a), and 3D (b-c) calibration test fields.....	37
Figure 3.8 Example of a portable calibration board (a), with collected points (b) and linear features (c) .....	38
Figure 3.9 Perspective transformation between image and object space straight lines ....	40
Figure 3.10 Visual representation of the ROT bundle similarity method.....	41
Figure 3.11 Example of a cable splitter for the camera remote trigger .....	42
Figure 3.12 Excerpt from the designed pattern for projection.....	43
Figure 3.13 Example of an artificial torso mannequin imaged without (a) and with (b) a projected pattern.....	43
Figure 3.14 Example stereo pairs of a human face taken without (a-b), and with (c-d) a projected pattern.....	46
Figure 3.15 Small differences in relief displacement between images with a short baseline (a-b); significant differences in relief displacement between images with a large baseline (c-d);.....	48
Figure 3.16 Intersection of conjugate light rays with a short baseline between the two camera perspective centres (a); intersection of two conjugate light rays at an angle close to 90° (b); multiple light ray intersection (c) .....	49
Figure 3.17 Surface reconstructed using a stereo pair with an intersection angle smaller than 45° (B = 0.3m, and Z = 1.6m) (a); surface reconstructed using a stereo pair with a larger baseline (B = 1.3m, and Z = 1.4m) (b).....	50
Figure 4.1 The proposed procedure for 3D surface reconstruction .....	53
Figure 4.2 Example of an original image of an artificial torso mannequin (a), and a region of interest mask (b) .....	54
Figure 4.3 Illustration of area-based image matching .....	55
Figure 4.4 Conjugate points appear on different rows in the original stereopair (a), and on the same row after normalization according to epipolar geometry (b) .....	57
Figure 4.5 Example of a normalized stereo pair, where sample corresponding points in the left and right images have significantly different x-parallax values.....	58
Figure 4.6 Hierarchical image matching examples for a given stereopair: first iteration – detected corners in the left (a) and right (b) images, and matched corners in the	

left (c) and right (d) images; second iteration – detected corners in the left (e) and right (f) images, and matched corners in the left (g) and right (h) images.....	60
Figure 4.7 Sample look-up tables of x-parallax values: after first iteration (a), and after second iteration (b) .....	61
Figure 4.8 Example of a reconstructed surface, i.e. the back side of an artificial torso mannequin, from one of the sensor arms .....	62
Figure 4.9 Examples of point cloud registration algorithms in 2D: minimizing distances between points and points (i.e. ICPPoint) (a), points and planes (i.e. ICPlane) (b), and points and triangular patches (i.e. ICPatch) (c) .....	64
Figure 4.10 Surface model representation (a), and criteria for accepting correspondence between conjugate primitives (b).....	67
Figure 4.11 Illustration of the transformation between the (X,Y,Z) and the (U,V,W) coordinate systems .....	73
Figure 4.12 Example of a pairwise registration of two overlapping surfaces (light gray: non-matched area in the TIN surface; black: matched area in the overlap between the point cloud and the TIN surface; dark gray: non-matched area in the point cloud) .....	76
Figure 4.13 Illustrations of the torso surface (a), sequential pair-wise surface registration (b), and simultaneous multiple surface registration (c) in 2D .....	77
Figure 5.1 Observing of the targets on the portable calibration board (a) with a high precision total station (b) .....	85
Figure 5.2 Camera calibration setup: camera stations (circles) and board targets (crosses) .....	86
Figure 5.3 Sensor arm setup showing all the cameras pointed towards a target board ....	94
Figure 5.4 Histogram plots showing image coordinate residuals in x (a), and y (b) for the bundle adjustment to establish the EOPs of the camera exposure stations.....	95
Figure 5.5 EOP determination: the camera positions shown with circles and the targets on the board with crosses .....	95
Figure 5.6 Example photo of the flat metal plate used in the experiment (a); the same plate imaged with a pattern projection (b); final 3D reconstruction of the flat metal plate (c).....	97
Figure 5.7 Histogram of the normal distances for the plane fitting of the flat metal plate reconstruction (a); Z-X plot of the normal distances above (black) and below (gray) the fitted plane (b) .....	98

Figure 5.8 The first (a) and second (b) subjects, and the irregular point clouds of their respectful face reconstructions (c), and (d) using the small (fine) pattern.....	99
Figure 5.9 Iterative solution for the transformation parameters for the facial reconstruction of the first (a) and the second (b) subject.....	101
Figure 5.10 Sensor arm setup showing all the cameras pointed towards the torso mannequin.....	104
Figure 5.11 The central images from the sensor arm for the four torso mannequin surfaces – the front/S <sub>1</sub> (a), the right side/S <sub>2</sub> (b), the back/S <sub>3</sub> (c), and the left side/S <sub>4</sub> (d).....	104
Figure 5.12 The reconstructed torso front/S <sub>1</sub> (a), right side/S <sub>2</sub> (b), back/S <sub>3</sub> (c), and left side/S <sub>4</sub> (d) surfaces.....	105
Figure 5.13 FaroArm .....	105
Figure 5.14 3D model of the entire reconstructed torso mannequin (left), and example cross section profile (right) .....	106
Figure 5.15 Iterative solution for the transformation parameters in the pairwise surface registration between S <sub>2</sub> and S <sub>1</sub> (a), S <sub>3</sub> and S <sub>2</sub> (b), S <sub>4</sub> and S <sub>3</sub> (c), and S <sub>4</sub> and S <sub>1</sub> (d) for the new dataset .....	110
Figure 5.16 Visual aid for the pairwise surface registration of S <sub>2</sub> and S <sub>1</sub> (a), S <sub>3</sub> and S <sub>2</sub> (b), S <sub>4</sub> and S <sub>3</sub> (c), and S <sub>4</sub> and S <sub>1</sub> (d) for the new dataset (light gray: non-matched area in the TIN surface; black: matched area in the overlap between the point cloud and the TIN surface; dark gray: non-matched area in the point cloud) .....	111
Figure 5.17 Example of a torso target (a), and the approximate distribution of measured control points (b).....	111
Figure 5.18 Registration of the FaroArm control points to the fully reconstructed 3D torso model.....	112
Figure 5.19 Iterative solution for the transformation parameters in the registration between the FaroArm control points and the fully reconstructed 3D torso model. .	114
Figure 5.20 Dual projector sensor arm setup showing all the cameras pointed towards the torso mannequin.....	115
Figure 5.21 Example images without (a) and with (b) a pattern overlap; zoomed in example view without (c) and with (d) the pattern overlap .....	116
Figure 5.22 Iterative solution for the transformation parameters in the registration between the FaroArm control points and the fully reconstructed torso models in the July (a) and the October (b) 2009 datasets.....	119

Figure 5.23 Iterative solution for the transformation parameters in the registration  
between the July and the October 2009 datasets ..... 120

## List of Abbreviations

Abbreviation	Definition
2D	Two-dimensional
3D	Three-dimensional
ANN	Artificial neural network
CMM	Coordinate measuring machine
CMOS	Complementary metal oxide semiconductor
DLP	Digital light processing
DLT	Direct linear transformation
DSLR	Digital single-lens reflex (camera)
EDM	Electronic distance measurement
EOPs	Exterior orientation parameters
GIS	Geographical information system
ICP	See ICPPoint
ICPatch	Iterative closest patch
ICPlane	Iterative closest plane
ICPoint	Iterative closest point
IOPs	Interior orientation parameters
MRI	Magnetic resonance imaging
NCC	Normalized cross correlation
PC	Perspective centre
RMS	Root mean square
RMSE	Root mean squared error
ROI	Region of interest
ROT	Rotation (bundle similarity method)
SMAC	Simultaneous multiframe analysis calibration
TIN	Triangular irregular network
TOF	Time of flight
USGS	United States geological survey
XGA	Extended graphics array

## Chapter One: Introduction

“Every valley shall be filled, and every mountain and hill shall be brought low; and the crooked shall be made straight, and the rough ways *shall be* made smooth;”

Luke 3:5, KJV

### 1.1 Background information on scoliosis

Scoliosis is an abnormal lateral curvature of the human spine (Roach, 1999). The spine is a flexible backbone column, which consists of 33 vertebrae. The vertebrae are divided into five regions: cervical, thoracic, lumbar, sacrum, and coccyx (see Figure 1.1).

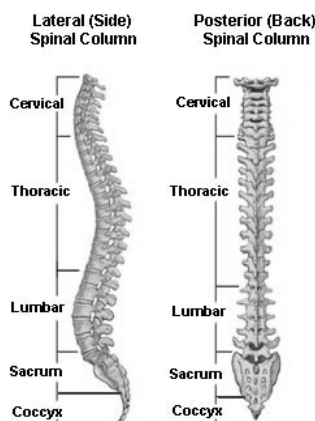


**Figure 1.1 Lateral (left) and posterior (right) views for the regions of the spine**

Source: <http://bioliscious.blogspot.com/2008/04/compendium-iii-chapter-11-skeletal.html>

The name for the disease comes from the Greek word *σκολιός* (transliteration: *skolios*; pronunciation: *skol-ee-os*), which means crooked. In essence, while a normal spine appears straight when seen from behind, a scoliotic spine appears “S” or “C” shaped (see Figure 1.2). Other than being simply curved, the scoliotic spine might also be rotated, which causes a deformity of the rib cage in three dimensions (see Figure 1.3a). This



and thus it is referred to as an idiopathic disease. It affects about 2-3% of the population, and it is more common in females than in males (Rogala et al., 1978; Weinstein, 1999). The disease is most commonly found in children between the ages of ten to sixteen, i.e. it appears at the onset of puberty, and then it progresses during the periods of rapid growth. If it is left untreated, scoliosis can negatively impact the patient's quality of life. For example, it can cause chronic back pain, respiratory problems, and impeded heart function (Nachemson, 1968). It is thus important to detect abnormal spinal curvatures as early as possible, and then to monitor the progression of the disease as closely as possible.

Scoliosis is usually first detected, or at least suspected, during a school screening session. The method most widely practiced during such a session is the Adams forward bend test (Adams, 1882). This test involves the child bending forward, while dangling arms and keeping feet together and having knees straight (see Figure 1.4a). This way the examiner could qualitatively indicate the presence or absence of any trunk asymmetry. The presence of any visible asymmetry is often quantified by measuring the angle of trunk rotation. This is the angle between the horizontal plane and the line across the back going through the point with maximum deformity. The angle of trunk rotation is usually estimated with a surface measuring device called a scoliometer (see Figure 1.4b) (Bunnell, 1984). Even though the scoliometer measurements are not considered accurate and reliable enough to guide scoliosis treatment, the instrument is still useful as a tool for preliminary diagnosis and further x-ray referral (Côté et al., 1998). So, once scoliosis is detected, or at least suspected, at the screening stage, a full-length standing spinal x-ray is taken in order to better quantify the spinal curvature (see Figure 1.5a). This is done by

measuring what is referred to as the Cobb angle (Cobb, 1948). The measurement involves drawing two lines. The first line is the one tangential to the superior endplate of the superior end vertebra (i.e. the top part of the top most angled vertebra). The second line is the one tangential to the inferior endplate of the inferior end vertebra (i.e. the lower part of the lowest most angled vertebra). The Cobb angle is the angle of intersection between the two lines (see Figure 1.5b).

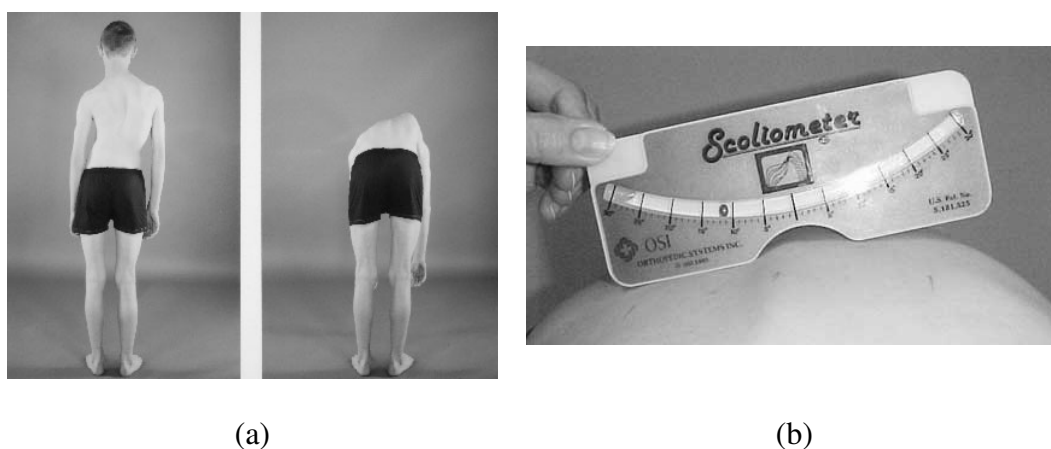


**Figure 1.4 Adams forward bend test (a), and the use of a scoliometer (b)**

Source for (a): <http://www.britscoliosissoc.org.uk/images/uploaded/scoliosis1.jpg>

Source for (b): <http://www.uthscsa.edu/scoliosis/images/Scoliometer.jpg>

The degree of the curvature and the speed of its progression are essential factors for assigning optimal scoliosis treatment. A curvature between  $25^{\circ}$  and  $40^{\circ}$  could be treated conservatively with exercises or bracing (see Figure 1.6). However, rapidly changing curvature or curvature exceeding  $40^{\circ}$ - $50^{\circ}$  requires surgery (Roach, 1999). This is why the disease progression must be monitored by periodic examinations (Montgomery and Willner, 1993; Torell et al., 1981). Unfortunately, these examinations involve taking additional spinal x-rays. Usually, a series of radiographs needs to be obtained as often as every three to four months for a period of time as long as five to six

years. This may amount to a significant exposure to ionizing radiation and a potential risk of cancer (Doody et al., 2000; Levy et al., 1996).

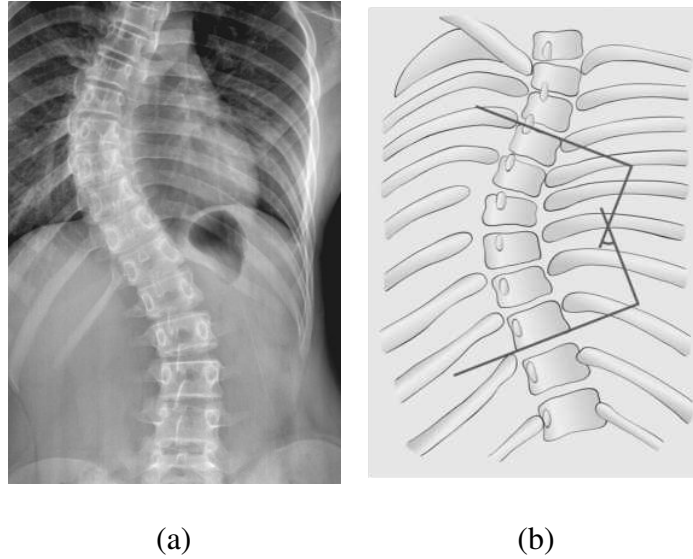


**Figure 1.5 Spinal x-ray (a), and measurement of the Cobb angle (b)**

Source for (a): <http://www.planetcl.com/images/scoliosis-xray-female.jpg>

Source for (b): <http://www.e-radiography.net/radpath/c/cobb-angle.jpg>

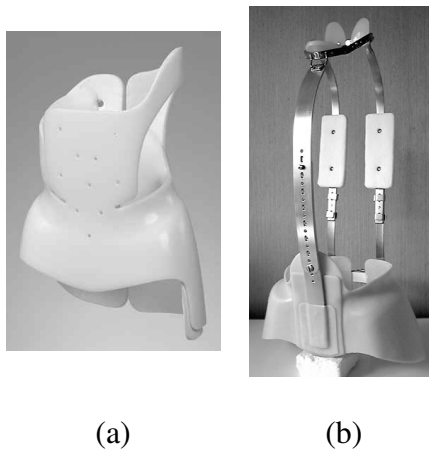


**Figure 1.6 Examples of a Boston brace (a), and a Milwaukee brace (b)**

Source for (a): <http://www.prosthetics-orthotics.net/scoliosis.jpg>

Source for (b): <http://transabled.org/wp-content/uploads/2007/04/milwaukee.jpg>

For this reason, it is imperative to minimize the use of radiographs and introduce a radiation-free methodology for monitoring the progression of scoliosis. Also, even though the Cobb angle method is the standard way of quantifying the curvature of the scoliotic spine, it is difficult to detect small changes in curvature due to errors in the measurements. Intraobserver variability of  $5^\circ$  (i.e. measurements repeatedly made by the same observer) and interobserver variability of  $10^\circ$  (i.e. measurements performed by different observers) at 95% confidence have been reported for Cobb angle measurements by qualified professionals (Goldberg et al., 1988; Morrissy et al., 1990). This is another reason why the Cobb angle method is not ideal for monitoring the progression of scoliosis. In addition, the traditional x-ray method for quantifying the spinal curvature and for monitoring the progression of the disease produces 2D images. It thus ignores the 3D nature of the scoliotic deformity, which includes both lateral and rotational distortions. In fact, the rotational component of scoliosis is a key factor in the progression of the spinal curve (Brown et al., 1976). An example of a non-radiographic 3D scanning technology is the magnetic resonance imaging (MRI). However, it is not suitable for the detection and monitoring of scoliosis, because the imaging is performed with the patient lying down instead of standing up, which neglects the effects of gravity on the spinal curvature. Furthermore, MRI would not be realistic for monitoring the disease progression because it is very expensive and often unavailable (Kotwicki, 2008).

However, the fact that the internal spine curvature and the torso surface deformity are highly correlated, makes quantifying the scoliotic deformity of the torso surface a valid monitoring alternative (Jaremko et al., 2002c). This already established correlation

motivated the current study, which deals with the design and implementation of a low-cost photogrammetric system for the 3D surface reconstruction of scoliotic torsos.

## **1.2 Research objectives**

The ultimate goal of this research project is to have a 3D measurement system, which could be of aid during the monitoring of the progression of scoliosis. In order for the system to be successfully used for routine scoliosis examinations in clinical environments, it must to fulfill the following requirements:

- The system must be non-invasive, radiation-free, and non-contact (i.e. no markers should be needed on the patient's body, other than for system validation);
- The system should provide high-precision 3D measurements (i.e. accurate to the millimetre or even sub-millimetre level);
- The system should be inexpensive – ideally, it should be built from low-cost and off-the-shelf hardware components, which could be easily replaced if broken;
- The system should have the capability to reconstruct homogeneous surfaces (i.e. the surface of a human torso), kinematic objects (i.e. the patients should not have to worry about staying absolutely still during data acquisition), and entire 3D objects (i.e. the full torso surface – the back, the front, and the two sides – should be measured);
- The system should be automated, i.e. the final product should be delivered quickly, without the requirement of a high level of expertise while the data is being processed.

In addition, it would be beneficial if the system could have the flexibility to be extended to dealing with other applications. For example, applications other than biomedical imaging may include structural deformation monitoring and cultural heritage documentation.

### **1.3 Thesis outline**

As a summary, this chapter first defined scoliosis, and listed some basic facts about the disease. Then, the options of treatment and the traditional ways of detecting and monitoring the progression of the disease were explained. After that, the necessity for minimizing radiation exposure by taking advantage of the correlation between the spinal deformity and the torso surface asymmetry were described. The last section concluded with a list of desired specifications for a 3D surface reconstruction system that could be used for routine scoliosis checks in a clinical environment.

The rest of the chapters in this thesis work are organized as follows:

- Chapter Two includes a literature review of commercial systems for 3D surface reconstruction and also custom built photogrammetric systems;
- Chapter Three explains the proposed system design, and describes the necessary prerequisites for the system to be functional as desired;
- Chapter Four describes the processing methodology for the generation of the torso model;
- Chapter Five discusses the current system implementation and lists the experimental results to date; and

- Chapter Six summarizes the thesis by including conclusions and recommendations for future work.

## **Chapter Two: Literature Review**

This chapter addresses the necessity of having an alternative to the traditional way of quantifying spinal deformity, i.e. it is suggested that torso surface measurements should complement or replace the estimation of the Cobb angle from radiographs. After that a brief history of surface measurements for scoliotic torsos is given, and some of the most recent commercially available scanners and custom built photogrammetric systems for 3D reconstruction are reviewed.

### **2.1 Torso surface measurements for estimating the spinal deformity**

The traditional methodology to diagnose, and later on, to monitor the progression of scoliosis involves measuring the so called Cobb angle from a single full-length standing spinal x-ray. If the particular patient has a spinal curvature of  $10^\circ$  or more, he or she is diagnosed with scoliosis, and a series of additional periodic x-ray examinations is undertaken in order to monitor the progression of the disease. The most important problems of the traditional Cobb angle method for monitoring the progression of scoliosis are:

- the estimated spinal curvature is in 2D instead of 3D,
- small changes showing the disease progression cannot be detected confidently due to errors and large variability in the Cobb angle measurements, and
- the total amount of ionizing radiation accumulates over time and increases the potential risk of cancer.

The use of stereo radiographs makes it possible to reconstruct and visualize the spinal deformity in 3D (Hindmarsh et al., 1980; Howell and Dickson, 1989; Kratky, 1975; Suh, 1974). However, taking more than one x-ray at every examination involves exposure to even more ionizing radiation. An alternative to this traditional way of monitoring the progression of scoliosis is to take advantage of the high correlation between the torso surface deformity and the internal spinal curvature (see Figure 2.1). This approach works by creating indices of the torso asymmetry, which relate to the spinal deformity (Jaremko et al., 2002c). The idea is to first complement and eventually, if possible, to completely replace the radiographic Cobb angle method with equivalent surface measurements.

There was a research project at the University of Calgary, where 3D torso surface measurements from optical range sensors were combined in a single digital model with spine and rib cage computer measurements from stereo x-rays (Poncet et al., 2000). One of the goals of that research project was to evaluate whether using 3D surface measurements, which depict the torso surface asymmetry, can be used to predict the spinal deformity (Jaremko et al., 2001). First, cross-sectional indices of the torso surface asymmetry were computed from the combined digital model, and then, these indices were used as input to a mathematical model based on artificial neural networks (ANN), in order to estimate the spinal deformity (Jaremko et al., 2000; Jaremko et al., 2002b). The results from the ANN approach were comparable to the manual measurements of the Cobb angle from a single x-ray. Moreover, they were considered better, because they had reduced measurement variability. So, it was concluded that the torso surface asymmetry can be used to reliably predict the spinal deformity (Jaremko et al., 2002a). Some of the

most recent work of this research was published by Swanson (2008). Naturally, the higher the quality of the 3D torso surface reconstruction, the better the results will be from the ANN method. The inner workings of the ANN algorithm are not within the scope of this thesis work, however, improving the 3D torso surface reconstruction is. The rest of this chapter will attempt to summarize some available systems, which provide radiation-free non-contact 3D measurements that might be suitable for scoliotic torso reconstruction.

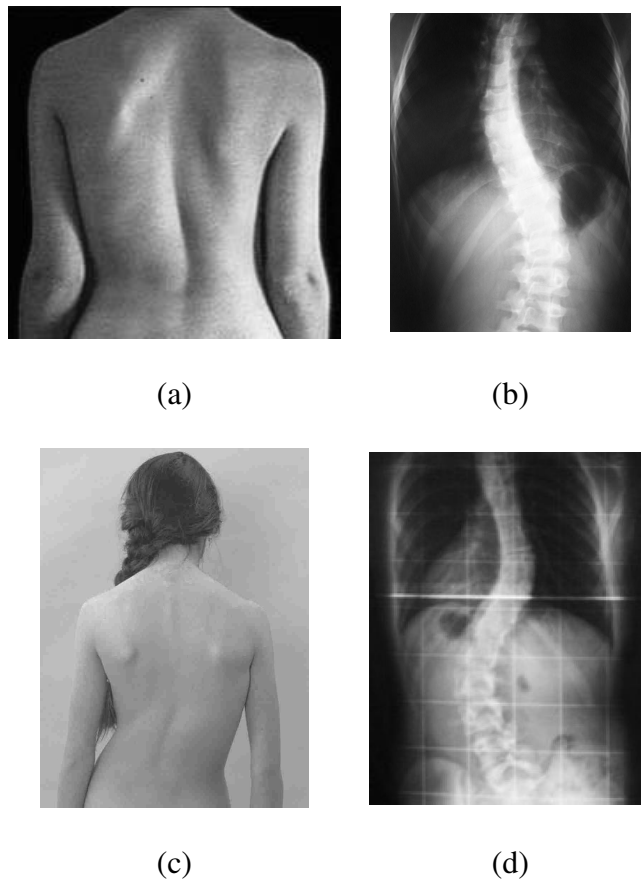


**Figure 2.1 Two examples of the correlation between the torso surface deformity (a, c) and the internal spinal curvature (b, d)**

Source for (a): <http://www.nlm.nih.gov/medlineplus/ency/images/ency/fullsize/1728.jpg>

Source for (b): <http://img.medscape.com/pi/emed/ckb/radiology/10295.jpg>

Source for (c): [http://www.bundesverband-skoliose.de/img/skoliose\\_bild.jpg](http://www.bundesverband-skoliose.de/img/skoliose_bild.jpg)

Source for (d): <http://medicineworld.org/images/blogs/6-2007/scoliosis-2020.jpg>

## **2.2 Brief history of surface measurements for scoliotic torsos**

Methodologies for measuring the surface of scoliotic torsos have been published since the late 19<sup>th</sup> century. From the end of the 19<sup>th</sup> century until the 1920s, mostly inclinometer-type instruments were used (D'Oswaldo et al., 2002). These instruments were simple, hand-held and obviously radiation-free, but they required contact with the patient. After World War I, the use of radiographs became popular, so torso surface measurements were ignored until the late 1950s (D'Oswaldo et al., 2002). In the 1960s, due to the awareness of the potential negative effects of ionizing radiation, simple hand-held instruments were once again designed for widespread screening programs. Since the 1970s and 1980s, with the introduction of computers, and the advancements in projectors and cameras, new radiation-free systems were developed for performing non-contact measurements (D'Oswaldo et al., 2002). Some of the more notable techniques included Moiré topography (Adair et al., 1977; Willner, 1979), rasterstereography (Drerup and Hierholzer, 1994; Frobin and Hierholzer, 1982), and optical triangulation scanning using incoherent light (Dawson et al., 1993; Turner-Smith et al., 1988; Weisz et al., 1988) and coherent light, i.e. laser (Ishida et al., 1982).

Moiré topography is a technique, which allows for a permanent record of body contour lines. This method works by illuminating the subject of interest with a spot light through a specially designed screen. The interference between the screen and its shadow creates a fringe pattern, which appears as contour lines on the back of the patient (see Figure 2.2a). These contour lines are then photographed by a camera (typically a film single-lens reflex was used) in order to be further analyzed for body

asymmetries/deformities (Adair et al., 1977; Willner, 1979). One of the major disadvantages of this technique is that the appearance of the contour lines depends on the position and orientation of the subject with respect to the screen and the spot light.

In rasterstereography, a grid pattern (see Figure 2.2b) is projected onto the back surface of the patient, and a still or video camera is used to capture the resulting projection. The camera must be positioned and oriented at a known displacement and rotation from the projector. Such known geometry is necessary in order to be able to compute the spatial coordinates of points on the surface of the patient's back via a triangulation algorithm. Thus, this method performs a 3D reconstruction in the form of a point cloud (Drerup and Hierholzer, 1994). Traditionally, slide projectors loaded with diapositives, and film or analogue video cameras were used.

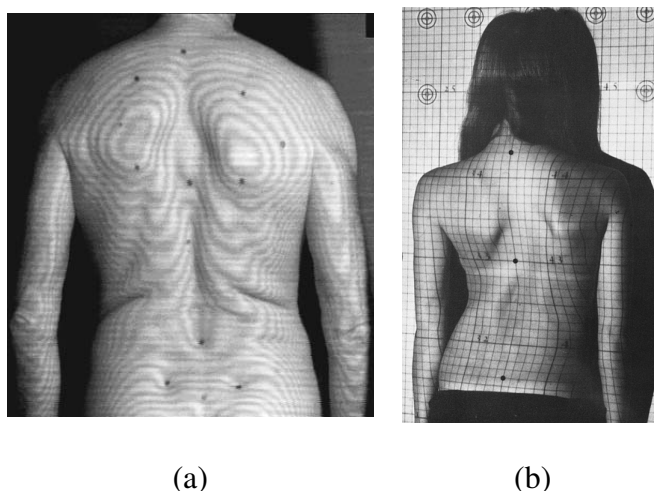


**Figure 2.2 Examples of Moiré topography (a), and rasterstereography (b)**

Source for (a): <http://biomech.ftvs.cuni.cz/pbpbk/kompendium/rhbengn/img/zada.gif>

Source for (b): Frobin and Hierholzer (1982)

Optical triangulation scanning is very similar to rasterstereography. One of the differences is that instead of a grid pattern, usually a single line is projected by an

incoherent light source or a laser emitter. Another difference is that a mechanical apparatus is needed to perform a sweeping motion so that the projected line can scan the full field of view of the camera (Ishida et al., 1982; Turner-Smith, 1988). See section 2.3.1 for an expanded description of triangulation scanners.

For more details on Moiré topography and rasterstereography, and for an evaluation of their performance for torso surface measurements please refer to Robu (2006) and Chang (2008). The next section will emphasize the more up-to-date 3D reconstruction systems that are currently commercially available.

## **2.3 Commercially available systems for 3D reconstruction**

There is a vast number of systems for 3D reconstruction, which are currently available on the market. Since it is not possible to list them all, the basic range measurement principles are explained first, and then examples are given for each type of system right after. The section first covers time-of-flight systems (generally based on coherent light), and then covers triangulation-based system (based either on coherent or incoherent light). At the end of the section, a summary regarding the suitability of these systems for scoliotic torso measurements is given.

### ***2.3.1 Time-of-flight systems***

One category of commercially available 3D reconstruction systems, based on the range measurement principle, is the time-of-flight (TOF) instruments. TOF instruments are primarily laser scanners, and they could be either pulse-based or phase-based. Please note that in some literature, e.g. Fröhlich and Mettenleiter (2004), phase-based instruments are not categorized under TOF systems, but as a separate category. The

pulse-based instruments emit a pulse at time  $t_E$ , and receive its echo reflected from the scanned object at time  $t_R$  (see Figure 2.3a). The range (or slope distance),  $\rho$ , can be computed by using equation (2.1) (Petrie and Toth, 2009). The range accuracy of pulse-based laser scanners is usually on the order of 0.5cm to 1cm (Blais, 2004).

$$\rho = \frac{c \cdot \Delta t}{2} \quad (2.1)$$

where:

$c$  = speed of light ( $\approx 3 \times 10^8$  m/s), and

$\Delta t = t_R - t_E$ , is the time elapsed between emitting and receiving the pulse

An example of a pulse-based laser scanner is the Trimble GX 3D Scanner (see Figure 2.4a). It has a field of view of  $360^\circ$  (horizontal) x  $60^\circ$  (vertical), and range from 2m to 200m with accuracy of 1.4mm to 6.5mm, respectively. It is capable of collecting 5,000 points per second with a density of 3mm at 100m or  $32 \mu\text{rad}$  increments (Trimble, 2009).

The phase-based instruments emit and receive a continuous wave (as opposed to a pulse) (see Figure 2.3b). The required measurements for the instrument include the number of complete wavelengths (or the integer ambiguity),  $n$ , and the phase difference angle,  $\phi$ , between the emitted signal and the signal received after its reflection from the object being scanned (see Figure 2.3c). The range,  $\rho$ , can be computed by using equation (2.2) (Petrie and Toth, 2009). The range accuracy of phase-based laser scanners is usually on the order of 3mm to 5mm or much better depending on whether amplitude or frequency modulation is used (Blais, 2004).

$$\rho = \frac{n \cdot \lambda + \Delta\lambda}{2} \quad (2.2)$$



TOF systems, both pulse-based and phase-based, are mainly preferred for measurements of long ranges, because the range precision remains almost constant for the entire volume of measurements (Blais, 2004). Exceptions to this rule are the newly developed range cameras. For example, the SwissRanger SR4000 (see Figure 2.4c) supports ranges of either 0.8m to 5m or 0.8m to 10m at 54 frames per second, with typical absolute accuracy of 10mm and 15mm, respectively. However, other than the low accuracy, these cameras have a relatively narrow field of view – 43.6° (horizontally) and 34.6° (vertically) – with a sensor matrix of only 176 pixels by 144 pixels. The pixel size is 40 $\mu$ m, and the nominal focal length is 10mm (Lewis and Waizenegger, 2010).

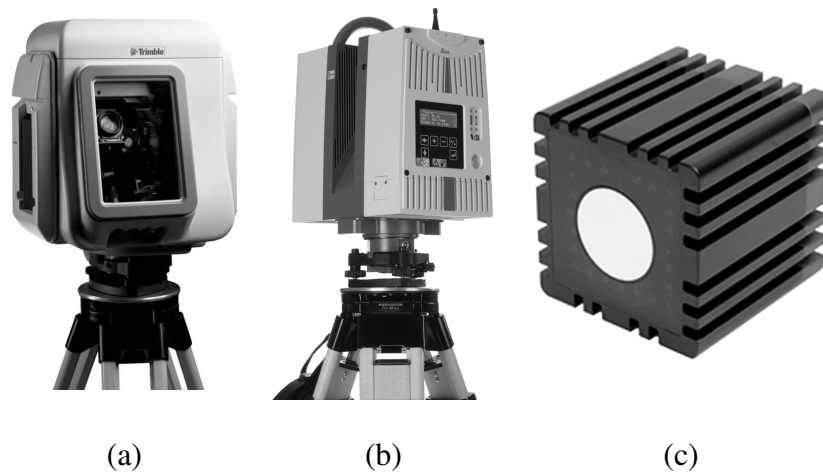


**Figure 2.4 Trimble GX 3D Scanner (a), Leica HDS6100 (b), and SwissRanger SR4000 (c)**

Source for (a): <http://www.pobonline.com/Files/Images/TrimbleGX3DScanner.JPG>

Source for (b): [http://hds.leica-geosystems.com/thumbs/originals/ADEI\\_1949.JPG](http://hds.leica-geosystems.com/thumbs/originals/ADEI_1949.JPG)

Source for (c): <http://www.acroname.com/robotics/parts/R317-SR4000-CW.jpg>

### **2.3.2 Triangulation systems**

Another category of commercially available 3D reconstruction systems, based on the range measurement principle, is the geometric or active optical triangulation instruments (also referred to as digitizers). In optical triangulation, a minimum of two

sensors (see Figure 2.5) with known relative location and orientation, also referred to as exterior orientation parameters (EOPs), are needed. One of the sensors is a source of light (either a laser emitting coherent light, or a projector emitting incoherent light). This light source projects a point, a line or a block pattern, which is displaced onto the surface of interest or the object being scanned. The other sensor is a camera with known interior orientation parameters (IOPs). The camera captures the generated light, and the deformation of this light onto the surface or object of interest is used as a direct function to derive the range and to calculate the 3D object coordinates (Blais, 2004).

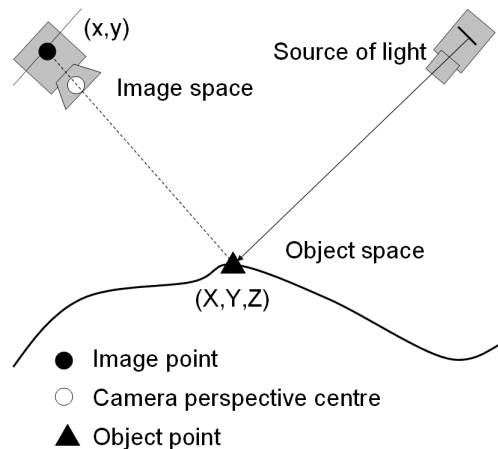


**Figure 2.5 Setup of a triangulation scanning system**

Triangulation systems are most suitable for close range reconstruction, and are generally a lot more accurate than TOF laser scanners. However, one limitation of these systems is that the baseline distance between the source of light and the camera has a fixed length, and the precision of the reconstructed 3D coordinates in the depth direction decreases as the object of interest moves away from the system.

There is an immense variety of such optical triangulation systems, but they can be generally categorized into three types: single point scanners, slit or line scanners and block pattern systems:

- The single point scanners operate with coherent light (i.e. laser). They have high resolution and very good accuracy, because of the large depth of focus. However, they require special scanning mechanisms in order to operate appropriately (Blais, 2004).
- The slit scanners project a line instead of a single point, so complete profiles are detected at a time (see Figure 2.6a). They operate with either coherent or incoherent light. They are mechanically and optically simpler and less costly than the single point scanners, but there is a compromise between the depth resolution and the field of view, and also they have poorer immunity to ambient light (Blais, 2004).
- The block pattern systems project either Moiré fringes or encoded/structured patterns (see Figure 2.6b). Generally, there is no need for a mechanical apparatus and incoherent light is used. However, they are most appropriate for large smooth surfaces with small depth variation, because compared to single point and line scanners, they have smaller depth of focus, and reduced dynamic range in intensity (Blais, 2004).

Examples of 3D reconstruction triangulation systems are the InSpeck 3D Mega Capturor II (see Figure 2.7a) and the Konica Minolta VIVID 9i Non-Contact 3D Digitizer (see Figure 2.7b). The InSpeck system is a block pattern system, and it projects a changing sinusoidal fringe pattern, which is captured by a digital camera in a few frames.

It has a field of view of 1.19m x 0.95m, and depth of field of 1m. At a distance of 1m to 1.5m, points are collected every 1mm. In less than one second the system can collect data that, after post processing, would yield up to 1.3 million points (InSpeck, 2009). The Minolta system is a laser line scanner. It has three lenses: 8mm (wide angle), 14mm (standard), and 25mm (telephoto). The projected laser line sweeps across the object being scanned, while being captured by a 640 pixels x 480 pixels digital camera. Its range is either from 0.6m to 1m or 0.5m to 2.5m. It takes 2.5 seconds to collect a point cloud, which is accurate to 50 $\mu$ m (Minolta, 2007).

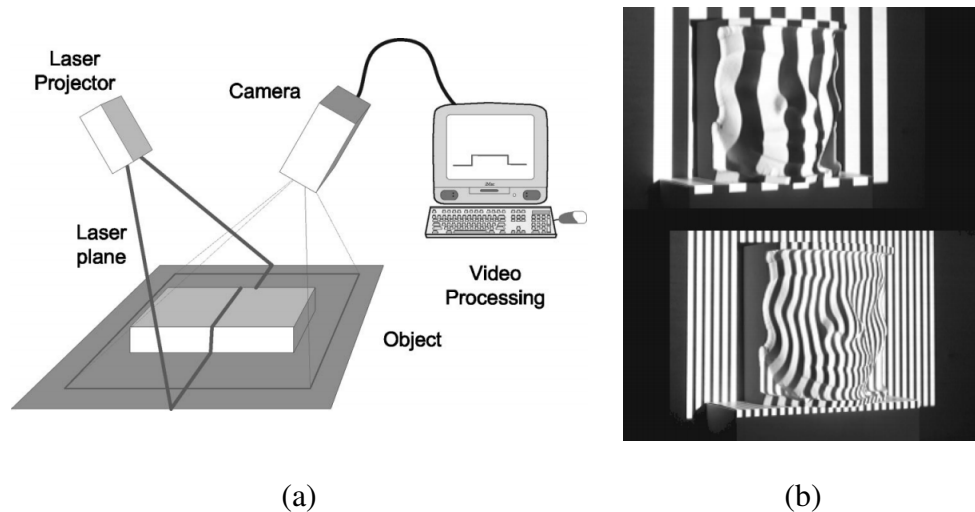


**Figure 2.6 Linear scanner setup (a) and an encoded block pattern with a different resolution (b)**

Source: Blais (2004)

Both the InSpeck and the Minolta systems are quite heavy duty. An example of a lighter weight triangulation unit is the hand-held Polhemus FastSCAN Scorpion (see Figure 2.7c). This is a trigger-operated laser line scanner. It is capable of scanning 50 lines per second. At a distance of 20cm from the object of interest, each line has a swath of up to 75cm, and the resolution and point accuracy are about 0.5mm and 0.75mm, respectively.

The downside of this scanner is that it is very sensitive to any metal objects nearby (Polhemus, 2008).

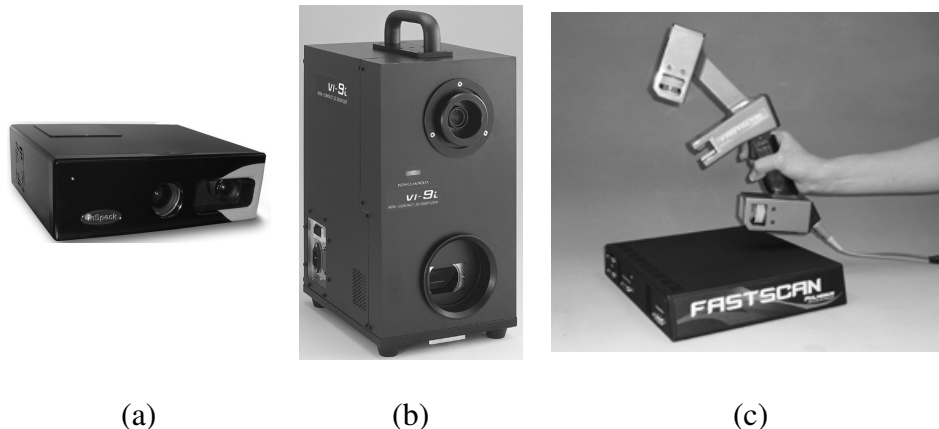


**Figure 2.7 InSpeck 3D Mega Capturor II (a), Konica Minolta VIVID 9i (b), and Polhemus FastSCAN Scorpion (c)**

Source for (a): [http://www.inspeck.com/pages/product\\_pictures/MegaCapturorII.jpg](http://www.inspeck.com/pages/product_pictures/MegaCapturorII.jpg)

Source for (b): <http://www.moreframes.com/storage/KonicaMinoltaVivid9i.jpg>

Source for (c): <http://www.polhemus.com/polhemus/assets/FastSCANScorpion.jpg>

### ***2.3.3 Summary of the commercially available systems for 3D reconstruction***

The previously mentioned commercially available systems for 3D reconstruction differ in performance, so this subsection is an attempt to compare them according to their suitability to be used for scoliotic torso measurements. The main criteria for comparison are accuracy of reconstruction, cost of the system, and ability to perform entire 360° reconstruction of kinematic human subjects. Please note that acquiring the price for a 3D reconstruction system, without the intension of purchasing one, is not a trivial matter, so the given cost ranges are approximate estimates. As it could be seen in Table 2.1 there is a trade-off between the cost of the system and the accuracy or the speed of the reconstruction process. For example, the SwissRanger SR4100 is the most affordable system, however, it has the worst accuracy. On the other hand, the Konica Minolta

VIVID 9i has the best accuracy, but it is fairly expensive. Since a single system could only map one surface at a time, at least four units would be needed to acquire the entire human torso, i.e. one each for the back, the front and the two sides. This would set the cost for a full scoliosis detection and monitoring system even higher. Actually, one of the main drawbacks of commercial 3D reconstruction systems is their extremely high cost (e.g. the Trimble GX 3D Scanner and the Leica HDS6100 could cost up to a couple of hundred thousand dollars).

**Table 2.1 Comparison of commercially available systems regarding the 3D reconstruction of a human torso**

<b>System</b>	<b>Unit Cost Range</b> [\$ x 1000]	<b>Accuracy</b> [mm]	<b>Speed</b> [sec]
<b>GX 3D Scanner</b>	100-200	1.4	~3-4
<b>HDS6100</b>	100-200	5	~1-2
<b>SR4000</b>	10-20	10	<1
<b>3D Mega Capturor II</b>	50-100	1-2	1
<b>VIVID 9i</b>	50-100	0.050	2.5
<b>FastSCAN Scorpion</b>	20-50	0.75	~1-2

Also, the Polhemus FastSCAN Scorpion is on the low end in the price range and at the same time it has sub-millimetre accuracy, but due to the nature of its data acquisition (i.e. being a hand-held instrument), it is not suitable for reconstruction of kinematic human subjects. In fact, the speed of data acquisition and the capability of synchronizing all the necessary units, are two of the most important factors in choosing

the desired scoliosis system. This is because a system, which takes a relatively long time to obtain a dense torso point cloud, might introduce 3D reconstruction errors due to the patient's breathing and movement. In this regard, even though any of the listed systems could be capable of producing a full 360° reconstruction of a static object with four units, only the SwissRanger SR4100 and the InSpeck 3D Mega Capturor II are suitable for the reconstruction of kinematic human torsos.

Another major disadvantage of some of these commercial ranging systems is that they are effectively black boxes due to several reasons. First, the data could usually only be processed with the provided proprietary software – this is especially the case with the InSpeck 3D Mega Capturor II. Second, the final output does not always come with any precision measures, and the accuracy of the reconstructed 3D coordinates might not be as optimistic as listed in the manufacturer's specifications. Lastly, since limited or no specific information is given about the system sensors or the mathematical model behind the reconstruction model, the end user cannot always interpret the outcome or interfere in the reconstruction process. For example, in case of a problem with the final results, the user might not be capable of resolving the issue due to lack of knowledge as to which step of the processing was erroneous. Sometimes, even with knowledge, the user might not be able to interfere in the processing, because the file formats used are proprietary. Due to these reasons, despite their good potential, commercial systems for 3D reconstruction are not recommended for measuring scoliotic torsos.

## 2.4 Custom-built photogrammetric systems for 3D reconstruction

Other than commercial systems for 3D reconstruction, custom-built photogrammetric systems, based on multiple cameras, also have the potential to be used for scoliotic torso measurements. Photogrammetry could be defined as the inverse process of photography. In photography a 3D object is captured in 2D images, and in photogrammetry multiple 2D images taken at different orientations are used to build a 3D model. The classic example of photogrammetric reconstruction is the stereo photography scenario (see Figure 2.8).

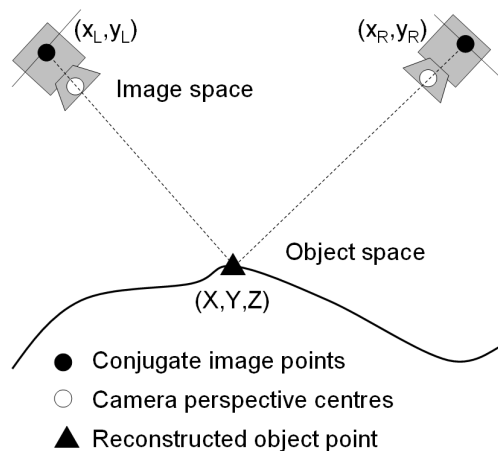


**Figure 2.8 Traditional stereo photography setup**

Here, after the IOPs and the EOPs are established, conjugate points are identified in the left and in the right images, and together with the knowledge of the locations of the left and the right camera perspective centres, and the orientation of the left and the right light rays, the location of the point of interest is intersected in the object space. The difference between the previously described active triangulation technique (implemented by most commercial instruments) and this classic stereo photography setup, is that the light source

is replaced by another camera. Traditional photogrammetric systems, which are frequently used for 3D surface reconstruction, have a few advantages over the previously listed commercial systems. First, they can collect images in fractions of a second, so in essence they do not need the patient to stay absolutely still, i.e. there is no motion problem (Mitchell and Newton, 2002). Second, a major advantage of photogrammetric systems is their high reconstruction accuracy due to the use of rigorous geometric modelling, i.e. implementing the collinearity equations rather than a simplified model such as the direct linear transformation (DLT) (Patias, 2002). Last but not least, low-cost off-the-shelf digital cameras and short-throw digital projectors are now flooding the electronics market and they are replacing the expensive analogue metric cameras and the custom made slide projectors used in traditional close-range photogrammetry. The use of such digital cameras and projectors is becoming a convenient and an inexpensive alternative for 3D reconstruction applications including biomedical imaging. In addition, the need for the movements of any parts in the system to be mechanically controlled during the data collection is negated through the use of multiple cameras (Siebert and Marshall, 2000). Remondino and El-Hakim (2006) also consider photogrammetric image based 3D modelling to be more complete, economical, portable, flexible and widely used compared to 3D commercial scanners. This study is thus motivated to investigate the potential for 3D reconstruction of scoliotic torsos using a photogrammetric system based on multiple digital cameras and projectors. There have recently been a few attempts to perform 3D human torso measurements with photogrammetric cameras. For example, Chong *et al.* (2009) successfully measured certain properties of the human spine with high precision. However, a full torso surface was not provided, rather only several

artificial markings, referred to as anthropometric landmarks, were reconstructed.

Remondino (2004) reconstructed the full body, but the object space standard deviations were on the order of several millimetres. This was due to the fact that uncalibrated cameras had to be used, and it was not possible to solve for the position of the principal point in the self-calibration procedure. D'Apuzzo (2002) claimed high precision for modelling the surface of a human face, and managed to track certain body motions. However, only partial reconstruction of the torso was provided. In particular, only the front side of the subject of interest was imaged.

The goal of this research project is to use the available know-how in the field of photogrammetry, and build a 3D reconstruction system, which could be used in the routine clinical examinations for scoliosis. Since digital cameras and projectors are radiation-free and also inexpensive, the main focus of this study is to have the system perform precise and full 360° reconstruction of kinematic objects with homogenous surface texture.

## **2.5 Summary of the literature review**

In this chapter, it was first recommended that torso surface measurements should be used to complement or replace the traditional way of spinal deformity quantification, i.e. the estimation of the Cobb angle from radiographs. After that a brief chronology of the radiation-free alternatives for scoliosis torso measurements was given. Then, there was a discussion on some of the current commercially available systems for 3D reconstruction. The systems were classified primarily on the range measurement principle, i.e. they were divided as either time-of-flight or triangulation-based systems. It

was decided that none of the example systems were adequate for torso surface measurements, because they were too expensive, not accurate enough, or too slow in order to be able to measure kinematic subjects. The suggested solution is to have a low-cost photogrammetric system, which does not have any motion problems, and uses rigorous sensor modelling so that the optimal accuracy is achieved. The next chapter describes the proposed system design.

## Chapter Three: Proposed System Design

This chapter focuses on the design of a photogrammetric system for the 3D reconstruction of the torso surface of scoliotic patients. The desired system must be able to perform high precision full 360° surface measurements of kinematic objects with homogeneous surfaces. It also has to be inexpensive and it should deliver the final results as quickly as possible. In order for it to meet these criteria, some key issues are carefully considered. First, the proposed system setup is described. Then, prerequisites for the optimal functionality of the system are explained. They include camera calibration and stability analysis, exterior orientation parameter (EOP) estimation, camera synchronization and pattern projection. Finally, the balance between intersection accuracy and matching reliability is addressed.

### 3.1 Proposed system setup

The proposed system for performing scoliotic torso surface measurements is based on photogrammetric principles. Thus, it uses images to carry out the computation of 3D coordinates. In order to do that, multiple cameras are first used to photograph different areas of the torso surface. So, in the proposed system, several low-cost off-the-shelf cameras together with an accompanying projector, used for projecting a pattern, are mounted on a metal support. This constitutes one sensor arm (see Figure 3.1a). Four of these sensor arms are located around the patient, so that the entire torso surface may be observed at the same time (see Figure 3.1b). Note that the metal piece holding the cameras for each sensor arm can rotate vertically through a swivel mechanism. This

function of the sensor arms is not needed for the image collection, i.e. there is no scanning involved. However, it allows the patients to easily get into position for data acquisition. They are able to do that by rotating one or two of the sensor arms (see Figure 3.2).

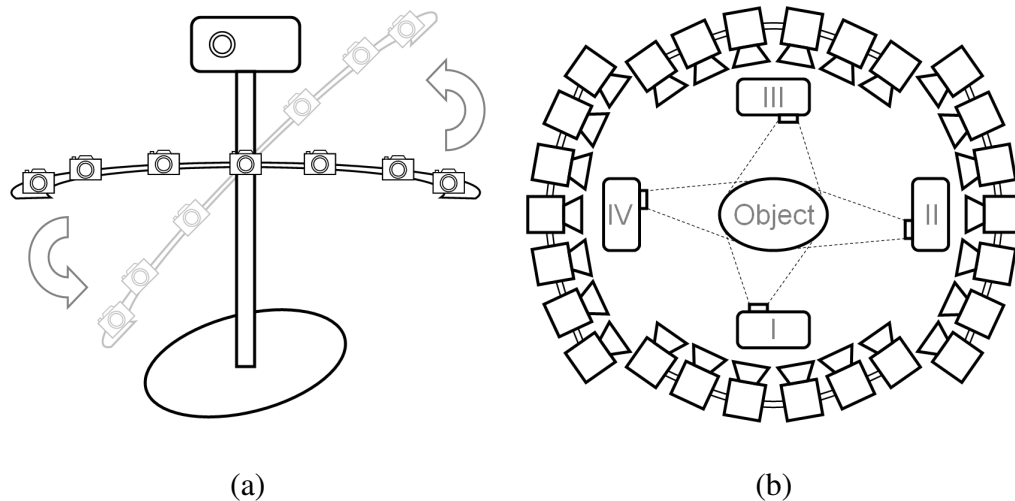


**Figure 3.1** Sensor arm prototype comprised of a projector and multiple cameras rotating vertically through a swivel mechanism (a); design of system setup comprised of four sensor arms (b)

The four sets of cameras are synchronized to operate simultaneously thus producing four surface models, i.e. one partial model of the torso from each sensor arm. The entire 3D torso model is then built through combining the four pieces by taking advantage of the overlap between them. In order for 3D reconstruction by a photogrammetric system to take place, there are a number of prerequisites that must be met. They are the following:

- The internal and external characteristics of the cameras must be estimated,
- Landmarks or conjugate points must be identified in the overlapping images, and

- The two steps above must be implemented in such a way that the best possible reconstruction quality would be achieved.

The following three sections, which deal with the necessity for system calibration, the use of a projected pattern, and the justification for having multiple cameras in each sensor arm, address in detail these prerequisites for the design of the proposed system.

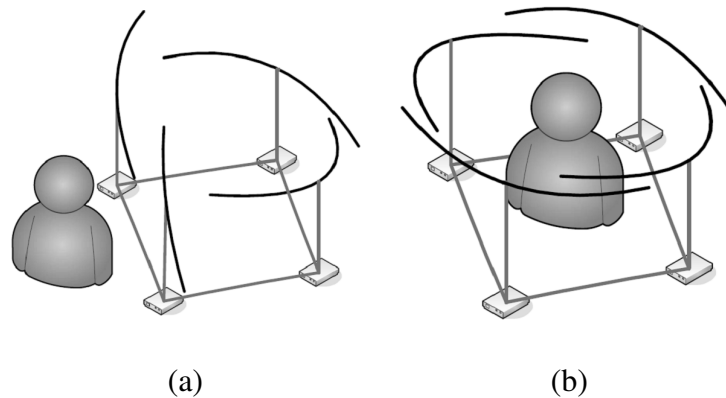


**Figure 3.2 Patient entering the system (a), and patient being ready for data acquisition (b)**

Source: Chang *et al.* (2009)

### 3.2 System calibration

The term system calibration refers to the estimation of both the internal and the external characteristics of the cameras employed. System calibration must be done before the cameras are used for the torso surface reconstruction. This is an important condition in order to achieve the highest reconstruction accuracy possible.

#### 3.2.1 Camera calibration and stability analysis

The objective of estimating the internal characteristics of the cameras, a process also known as camera calibration, is to obtain the camera's interior orientation parameters (IOPs). They include the principal point coordinates  $(x_{pp}, y_{pp})$ , the principal

distance,  $c$ , and the lens distortion parameters. The principal point (pp) is the projection of the camera's perspective centre (PC) onto the image plane. The principal distance is the distance between the principal point and the perspective centre. Note (in Figure 3.3a) that the principal point does not necessarily coincide with the centre of the image, or with the fiducial centre (fc) in the case of analogue metric cameras. The lens distortion parameters describe any deviations from the collinearity condition, i.e. the assumption that the perspective centre, any image space point and its corresponding object space point lie on a straight line. The IOPs are necessary in order to compute the distortion-free coordinates of any image points, which together with the location of the perspective centre, are used to define the bundles of light rays at the moment of exposure.

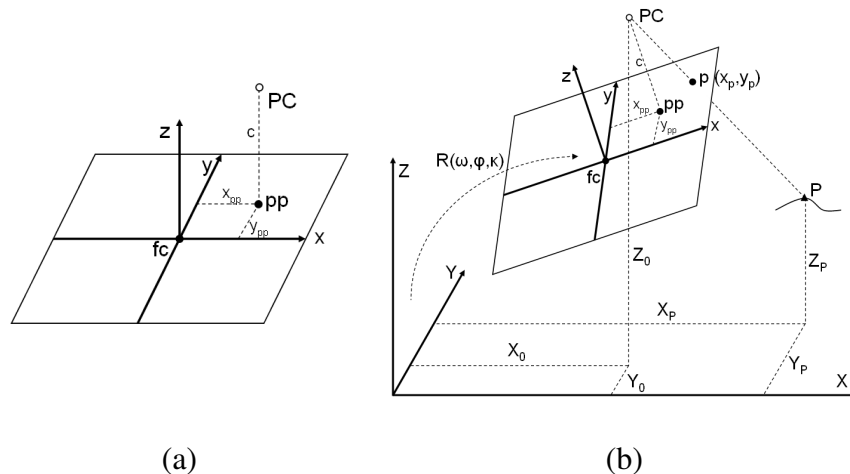


**Figure 3.3 Illustration of the principal point offset (a); example of the collinearity condition and the relation between the object and the image space coordinate systems (b)**

Bundle adjustment with self-calibration is commonly used for camera calibration. Other than estimating for the desired IOPs, the EOPs of the images involved, and the object space coordinates on any tie points involved, are also solved for in the bundle

adjustment with self-calibration procedure. The EOPs include the location (or the position) of the camera perspective centre and the orientation of the image coordinate system with respect to the object space coordinate system. In this way, the EOPs simulate the position and orientation of the camera at the moment of exposure. In order for the EOPs to be estimated a calibration field having targets with known object space coordinates is necessary. The observations involved are the image coordinates of the measured calibration targets. The mathematical model for the photogrammetric bundle adjustment is the collinearity equations (Kraus, 1993):

$$\begin{aligned} x_p &= x_{pp} - c \cdot \frac{r_{11} \cdot (X_p - X_0) + r_{21} \cdot (Y_p - Y_0) + r_{31} \cdot (Z_p - Z_0)}{r_{13} \cdot (X_p - X_0) + r_{23} \cdot (Y_p - Y_0) + r_{33} \cdot (Z_p - Z_0)} + \Delta x_p \\ y_p &= y_{pp} - c \cdot \frac{r_{12} \cdot (X_p - X_0) + r_{22} \cdot (Y_p - Y_0) + r_{32} \cdot (Z_p - Z_0)}{r_{13} \cdot (X_p - X_0) + r_{23} \cdot (Y_p - Y_0) + r_{33} \cdot (Z_p - Z_0)} + \Delta y_p \end{aligned} \quad (3.1)$$

where:

$(x_p, y_p)$  are the observed image coordinates for point p,

$(X_p, Y_p, Z_p)$  are the corresponding object space coordinates for point P,

$r_{11}$  to  $r_{33}$  are the elements of the 3D rotation matrix, R, which relates the object to the image coordinate systems, and is based on the angles  $\omega$ ,  $\phi$ , and  $\kappa$ ,

$(X_0, Y_0, Z_0)$  are the object space coordinates of camera perspective centre PC, and

$(\Delta x_p, \Delta y_p)$  are the distortions in image space for point p.

The above terminology involved in the collinearity condition is visually described in Figure 3.3b. In addition, the distortions in image space may be divided into radial lens distortion, decenteric lens distortion, affine deformation, and others. Radial lens distortion may follow either a pincushion (see Figure 3.4a) or a barrel (see Figure 3.4b) pattern.

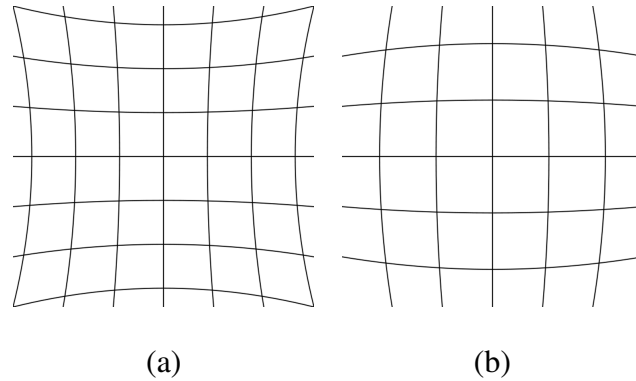


**Figure 3.4 Examples of pincushion (a), and barrel (b) lens distortion**

Source for (a): [http://commons.wikimedia.org/wiki/File:Pincushion\\_distortion.svg](http://commons.wikimedia.org/wiki/File:Pincushion_distortion.svg)

Source for (b): [http://commons.wikimedia.org/wiki/File:Barrel\\_distortion.svg](http://commons.wikimedia.org/wiki/File:Barrel_distortion.svg)

There are many existing mathematical models, which attempt to describe these deviations from the collinearity condition. Some examples are the Brown-Conrady model (Brown, 1971), the USGS simultaneous multiframe analysis calibration (SMAC) (Light, 1992), and the Chebyshev normalized orthogonal polynomials model (Smith et al., 1992). The model used in this research project falls under the Brown-Conrady category, and is defined as follows (Kraus, 1997):

$$\begin{aligned}\Delta x_p &= k_1 \cdot (r^2 - r_0^2) \cdot x' + k_2 \cdot (r^4 - r_0^4) \cdot x' + p_1 \cdot (r^2 + 2 \cdot (x')^2) + 2 \cdot p_2 \cdot x' \cdot y' - a_1 \cdot x' + a_2 \cdot y' \\ \Delta y_p &= k_1 \cdot (r^2 - r_0^2) \cdot y' + k_2 \cdot (r^4 - r_0^4) \cdot y' + p_2 \cdot (r^2 + 2 \cdot (y')^2) + 2 \cdot p_1 \cdot x' \cdot y' + a_1 \cdot x' - a_2 \cdot y'\end{aligned}\tag{3.2}$$

where:

$k_1$  and  $k_2$  are the radial lens distortion parameters,

$p_1$  and  $p_2$  are the decentering lens distortion parameters,

$a_1$  and  $a_2$  are the affine deformation parameters,

$r$  is the radial distance,  $r^2 = (x')^2 + (y')^2$ , and  $x' = x_p - x_{pp}$ , and  $y' = y_p - y_{pp}$ , and

$r_0$  is the radial distance with zero radial lens distortion (other than the principal point).

Generally, the precision of the estimated IOPs during the camera calibration procedure depends on the camera station geometry (such that any potentially correlated parameters may be decoupled as much as possible), the precision of the image coordinate measurements, and the method of datum definition (Clarke and Fryer, 1998; Fraser, 1997). The camera station geometry during the image acquisition defines how strong the bundle adjustment solution would be, so it is important to take it under serious consideration. It is preferred that the bundles of light rays from the cameras to the calibration targets intersect at an angle as close to  $90^\circ$  as possible in both the horizontal (i.e. between left and right camera stations) and the vertical (i.e. between the low and high camera stations) planes. Ideally, all targets should be present in all images, and the entire image format should be filled with targets as much as possible. Also, photographs in both landscape and portrait orientation must be taken in order to decouple the IOPs and the EOPs (Remondino and Fraser, 2006). The image measurement precision depends on whether natural or signalized targets are used, and whether the targets are measured manually or automatically. Some examples of signalized targets are crosses, circles or checker-board squares (see Figure 3.5). The two most common ways of datum definition are by either using pre-surveyed control points, or by fixing the object coordinates of certain points and using distance constraints. Other methods include minimally controlling the datum, e.g. performing inner constraints or a free-network adjustment. In the case of the former methods, the control points or distance measurements must be well distributed and encompass the entire image space as much as possible (see Figure 3.6 for

visual examples). In all cases, tie points are necessary to increase the redundancy and strengthen the bundle adjustment solution.

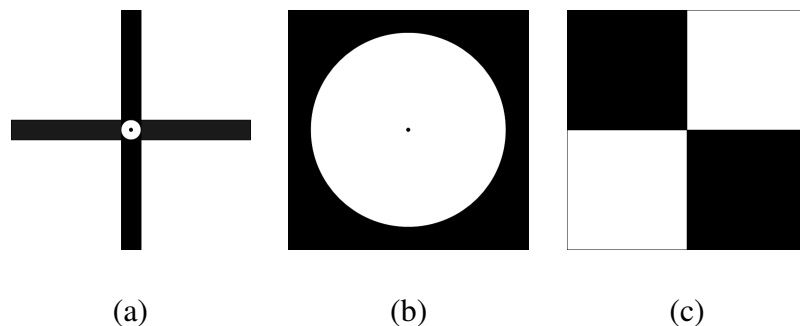


**Figure 3.5** Examples of cross (a), circle (b), and checker-board (c) signaled targets

Source: Detchev *et al.* (2010)

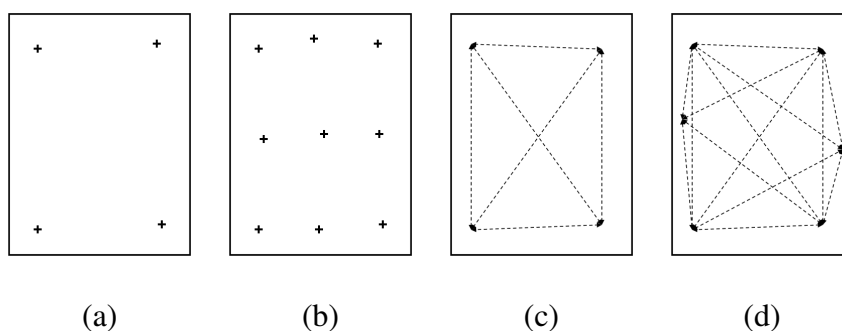


**Figure 3.6** Examples of control point (a-b), and distance measurement (c-d) distribution in the image format

Source: Detchev *et al.* (2010)

Indoor test fields for calibrating close-range photogrammetric cameras could be either 2D or 3D (see Figure 3.7). Examples for a 2D field are a single wall in a room or a portable flat board. Examples for a 3D test field are an inside corner of a room, a cube or a cage. Depending on whether a 2D or a 3D test field is chosen, different data acquisition procedures are required. The ideal option for such an indoor test field is a 3D cage. In this case, the observed points fill up a 3D volume, so a relatively simple image configuration

is needed during the data acquisition procedure. However, it is very difficult and/or expensive to secure space that is large enough for such a calibration cage, so a 2D test field is often more convenient to have. The downside of this option is that the observed points lie on a relatively flat surface, so a more stringent image configuration is needed.

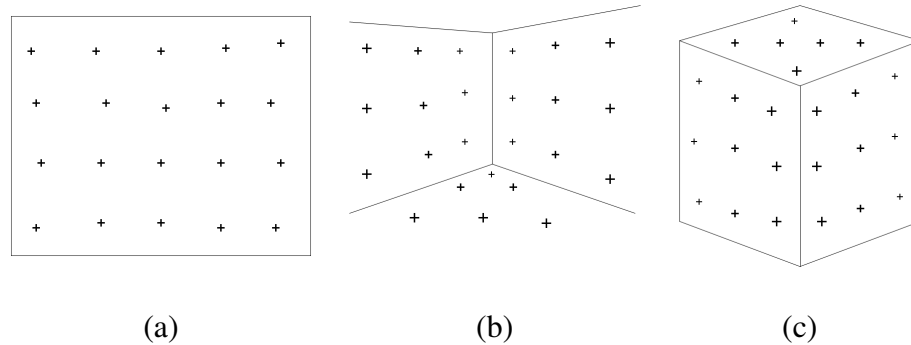


**Figure 3.7 Examples of 2D (a), and 3D (b-c) calibration test fields**

Source: Datchev *et al.* (2010)

Also, the target points within the test field need to be surveyed. Conventionally, this is done with specialized surveying instruments (e.g. a total station). Again, this could be quite an expensive procedure, because a competent survey crew and high grade equipment must be available, so a less complex alternative to this is to measure distances between certain points in the test field with a measuring tape.

Since consumer grade (i.e. inexpensive) cameras are being used for this research project, their calibration should be as simple and as practical as possible, so that the cost of the calibration is proportional to the cost of the cameras. So bearing this in mind, i.e. to avoid high cost, an easy-to-establish test field for the purpose of semi-automated indoor calibration is being used in this research project. The test field is comprised of a portable flat board (1.5m x 1.2m) with attached point targets and linear features (see Figure 3.8). The choice of target design fell on the checkerboard one, because it is suitable for

automatically detecting the target centres, and at the same time, it is practical when pointing and focusing on the targets with a total station (in cases whenever a total station needs to be used). The board was built with common construction materials and tools. It is sturdy enough so that it does not warp, but at the same time, it is light enough so that it could be moved from one location to another. Thus, its major advantages are its portability and compactness (Detchev *et al.*, 2010).

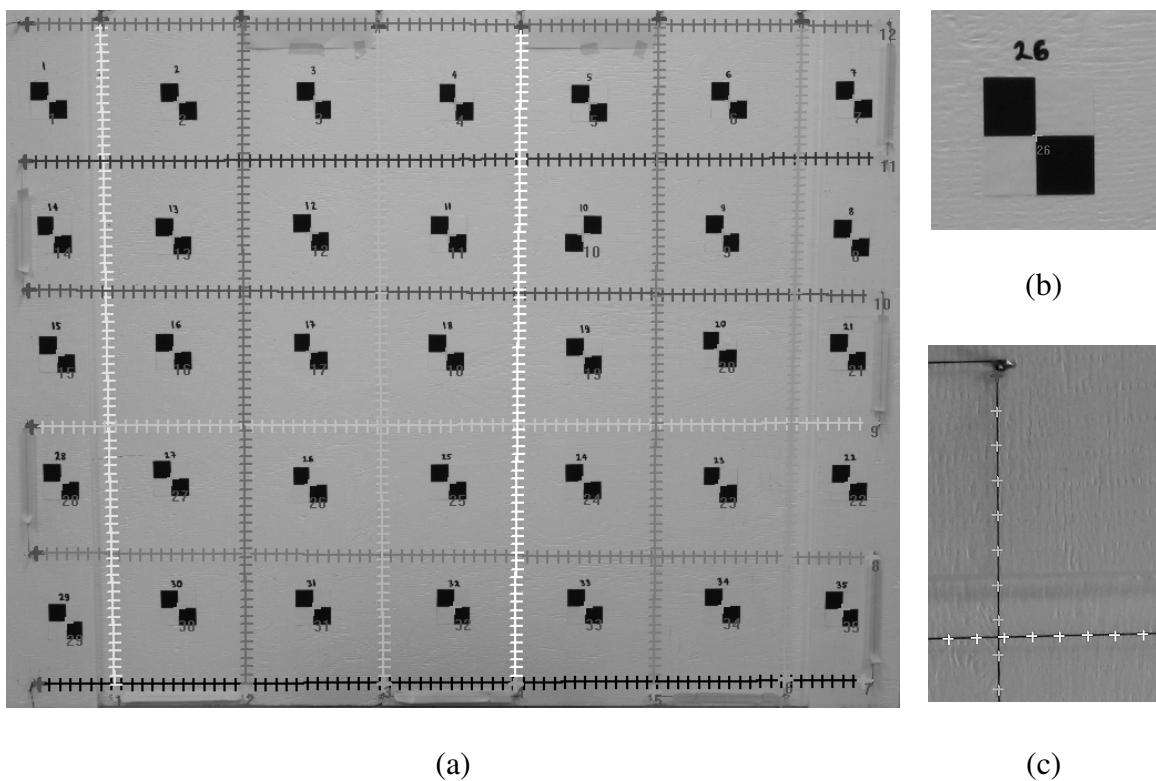


**Figure 3.8** Example of a portable calibration board (a), with collected points (b) and linear features (c)

Source: Detchev *et al.* (2010)

In addition, it needs a moderate number of target points, because the linear features are used in the estimation of the lens distortion parameters. In absence of any distortion, straight features, should also appear straight in the image space. Any deviation from straightness in the image space is attributed to the lens distortion parameters (Habib

and Morgan, 2003). The linear features in image space are represented by two end points and a number of intermediate points along the line of interest. The end points need to be identified in only one image, i.e. they do not need to be visible in the rest of the images, and their image coordinate measurements are included in the collinearity equations. The mathematical constraint used in order to incorporate the intermediate points as observations in the bundle adjustment follows the idea that the vector from the perspective centre to any intermediate image point is contained within the plane defined by the perspective centre of that image and the two points that define the straight line in object space (see Figure 3.9). This constraint incorporates the image coordinates of any intermediate points, the EOPs, the IOPs (including the distortion parameters), and the object space coordinates of the points that define the object space line. Thus, the constraint does not introduce any new parameters, and it could be written for the intermediate points along each line in the imagery. The equation used is the following (Habib et al., 2002):

$$(\vec{V}_A \times \vec{V}_B) \cdot \vec{V}_p = 0 \quad (3.3)$$

where:

$\vec{V}_A$  is the vector which connects the perspective centre of one of the images to the first end point, A, along the object space line,

$\vec{V}_B$  is another vector which connects the same perspective centre to the second end point, B, along the object space line, and

$\vec{V}_p$  is the vector which connects the perspective centre to the intermediate point, p, along the corresponding image line.

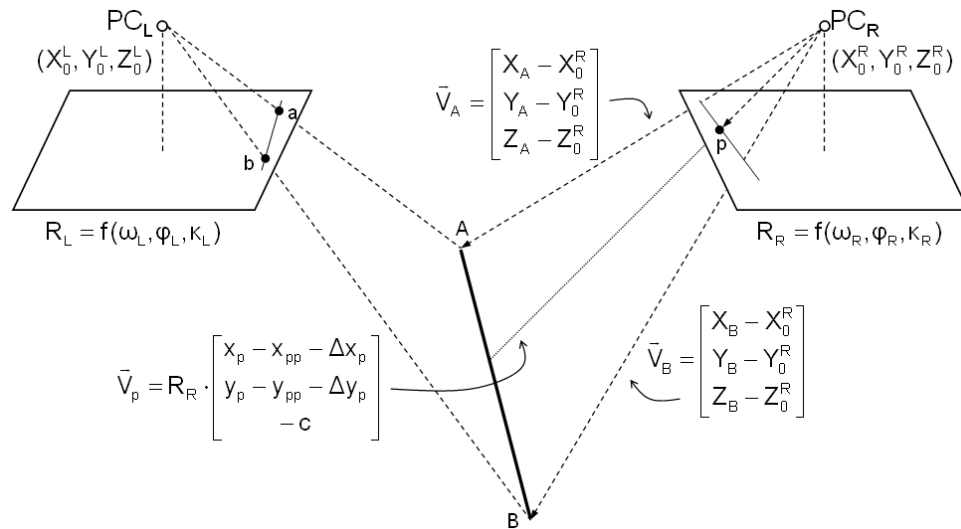


**Figure 3.9 Perspective transformation between image and object space straight lines**

Sources: Habib *et al.* (2002), and Habib and Morgan (2003)

An extension of the camera calibration is the stability analysis procedure. The cameras should go through such a procedure in order to verify that the estimated IOPs do not change significantly over time. The IOPs define the bundle of light rays for the camera, so it is important that the IOPs from different calibrations define bundles of light rays that are similar. This is necessary, because the cameras used are amateur ones (i.e. they were simply bought off-the-shelf), and they are not designed specifically for metric applications (Habib and Morgan, 2005). Checking the stability between two IOP sets for the same camera cannot be done by simply comparing the numerical values for the parameters, because the IOPs are correlated. Thus, the comparison must be done by estimating the similarity between the bundles of light rays defined by the two IOP sets. The bundle similarity method used in this research project is referred to as ROT, which stands for “rotation”. In the ROT method, two bundles of light rays share the same perspective centre, but they have different orientations in space, i.e. the two bundles are

rotated to reduce the angular offset between the conjugate light rays (see Figure 3.10). In order to evaluate the degree of similarity between the two bundles, a root mean square (RMS) value is computed for a simulated grid of points. The RMS value represents the average spatial offset along the image plane between the conjugate light rays of the two bundles. The bundles are deemed similar if the computed RMS value is within the expected image measurement accuracy (e.g. half a pixel to one pixel) (Habib et al., 2008; Habib et al., 2005).

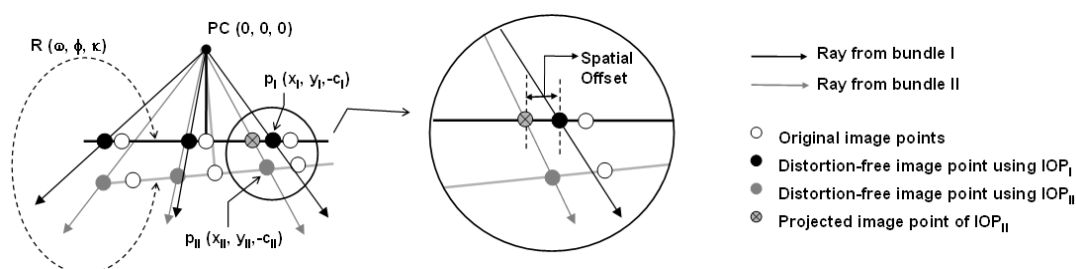


**Figure 3.10 Visual representation of the ROT bundle similarity method**

Sources: Habib *et al.* (2006)

### 3.2.2 Exterior orientation parameter estimation

The camera calibration procedure is not performed while the cameras are mounted to their respective sensor arms. Due to the stringent requirements for the camera station geometry, imposed by having a 2D calibration test field, every camera is calibrated individually before being mounted on its corresponding sensor arm. So once each camera is first calibrated and mounted to the metal frames, then the relative EOPs of the cameras used for each sensor arm must be estimated with respect to a separate local coordinate system. This is achieved through another bundle adjustment procedure using a test field with target points, where the distances between some of the points have been previously measured. One of the cameras (e.g. the central one) for each of the sensor

arms is chosen to define its corresponding local reference frame. Since the cameras are rigidly mounted on the metal arms, the relative orientation parameters for the cameras on each of the sensor arms should stay the same. Thus, the bundle adjustment for each sensor arm is required to be done only once.

### 3.3 Camera synchronization and pattern projection

Once the system has been calibrated, the cameras are in place and are ready to be used. The shutter release on each camera could be controlled remotely, so that there is no contact with any of the cameras. In order for all the cameras to operate at the same time, only one remote trigger should be used. To achieve synchronization, the wire for the remote trigger must be split for all the cameras (see Figure 3.11).

Another prerequisite for the proposed system is the use of projectors. The purpose of having them is to project a pattern (see Figure 3.12) onto the torso in order to provide artificial markers on its surface. This is necessary, because the torso surface is relatively homogeneous. With no artificial markers, it would be impossible to identify conjugate points in the captured imagery (see Figure 3.13).

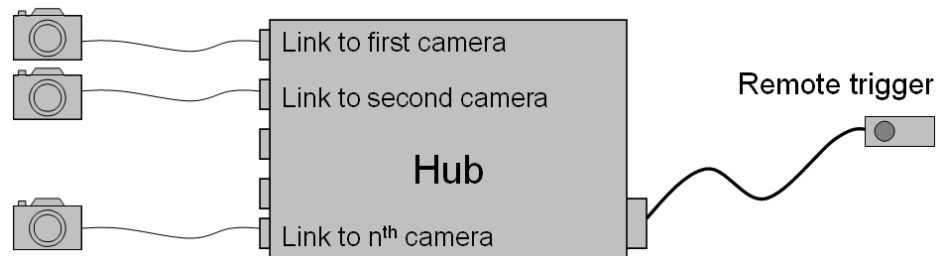


**Figure 3.11 Example of a cable splitter for the camera remote trigger**

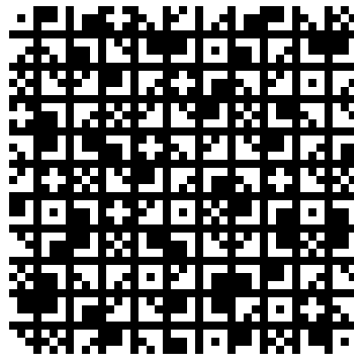
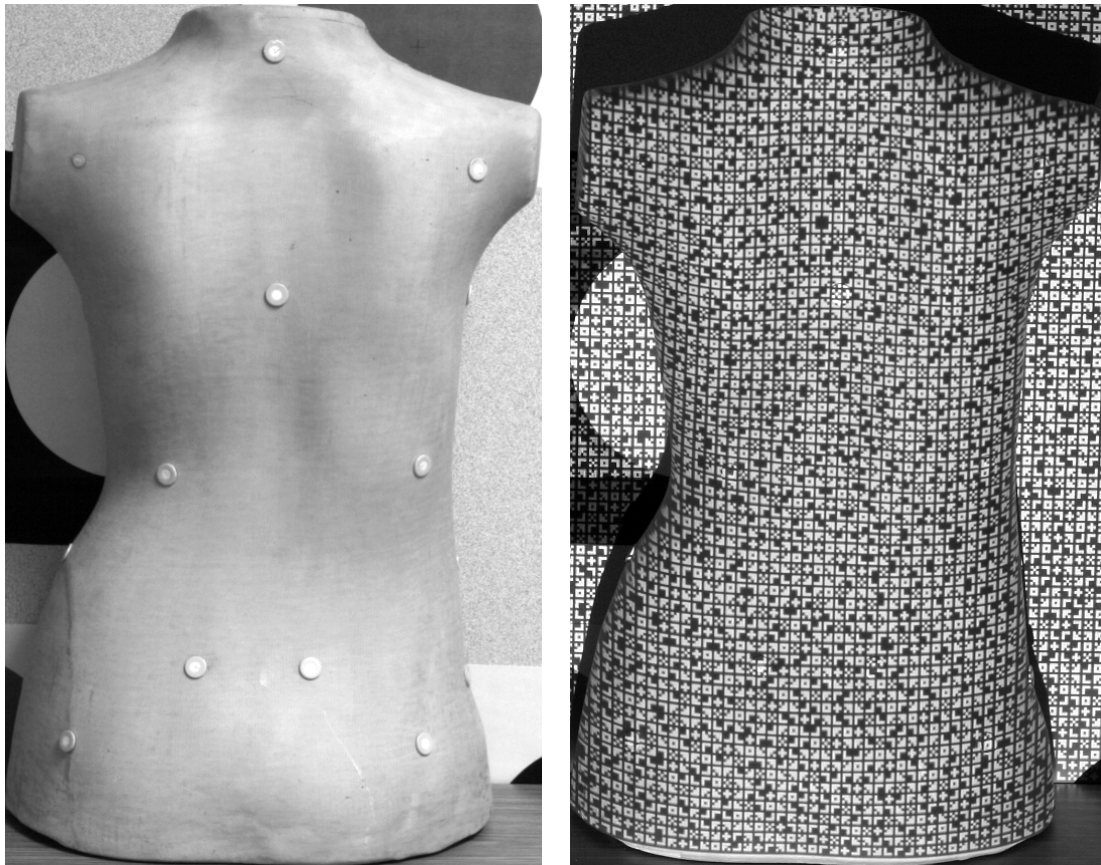


**Figure 3.12** Excerpt from the designed pattern for projection



(a)

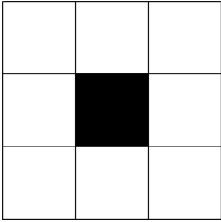
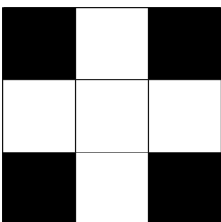
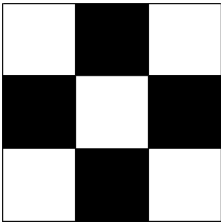
(b)

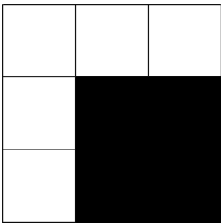
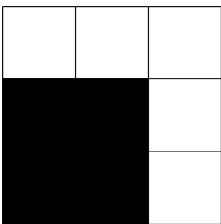
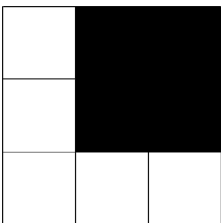
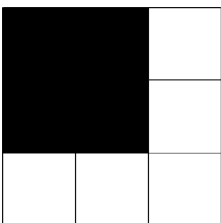
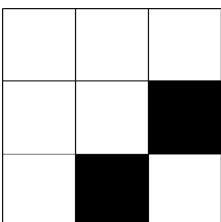
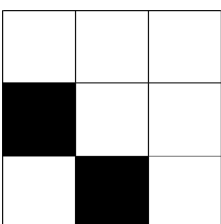
**Figure 3.13** Example of an artificial torso mannequin imaged without (a) and with (b) a projected pattern

Source: Chang *et al.* (2009)

Also, by regulating the resolution of the projected pattern, the density of the final generated point cloud could be controlled. The projected pattern is generated by randomly arranging eleven unique 3 x 3 pixel blocks (see Table 3.1). However, to minimize any matching ambiguity, no pixel block is repeated within a radius of six pixels within the pattern. During the projection of the pattern, the lighting must be managed so that optimal contrast of the artificial features is achieved on the surface of the subject of interest. Please note that the pattern is currently only used for projection, and not for calibrating the actual projector.

**Table 3.1 Binary encoding and corresponding images for the 3 x 3 pixel block patterns used**

<b>Pattern ID</b>	<b>Binary Encoding</b>	<b>Corresponding Image</b>
<b>1</b>	1    1    1 1    0    1 1    1    1	
<b>2</b>	0    1    0 1    1    1 0    1    0	
<b>3</b>	1    0    1 0    1    0 1    0    1	

<b>4</b>	<table border="1"> <tbody> <tr> <td>1</td> <td>1</td> <td>1</td> </tr> <tr> <td>1</td> <td>0</td> <td>0</td> </tr> <tr> <td>1</td> <td>0</td> <td>0</td> </tr> </tbody> </table>	1	1	1	1	0	0	1	0	0	
1	1	1									
1	0	0									
1	0	0									
<b>5</b>	<table border="1"> <tbody> <tr> <td>1</td> <td>1</td> <td>1</td> </tr> <tr> <td>0</td> <td>0</td> <td>1</td> </tr> <tr> <td>0</td> <td>0</td> <td>1</td> </tr> </tbody> </table>	1	1	1	0	0	1	0	0	1	
1	1	1									
0	0	1									
0	0	1									
<b>6</b>	<table border="1"> <tbody> <tr> <td>1</td> <td>0</td> <td>0</td> </tr> <tr> <td>1</td> <td>0</td> <td>0</td> </tr> <tr> <td>1</td> <td>1</td> <td>1</td> </tr> </tbody> </table>	1	0	0	1	0	0	1	1	1	
1	0	0									
1	0	0									
1	1	1									
<b>7</b>	<table border="1"> <tbody> <tr> <td>0</td> <td>0</td> <td>1</td> </tr> <tr> <td>0</td> <td>0</td> <td>1</td> </tr> <tr> <td>1</td> <td>1</td> <td>1</td> </tr> </tbody> </table>	0	0	1	0	0	1	1	1	1	
0	0	1									
0	0	1									
1	1	1									
<b>8</b>	<table border="1"> <tbody> <tr> <td>1</td> <td>1</td> <td>1</td> </tr> <tr> <td>1</td> <td>1</td> <td>0</td> </tr> <tr> <td>1</td> <td>0</td> <td>1</td> </tr> </tbody> </table>	1	1	1	1	1	0	1	0	1	
1	1	1									
1	1	0									
1	0	1									
<b>9</b>	<table border="1"> <tbody> <tr> <td>1</td> <td>1</td> <td>1</td> </tr> <tr> <td>0</td> <td>1</td> <td>1</td> </tr> <tr> <td>1</td> <td>0</td> <td>1</td> </tr> </tbody> </table>	1	1	1	0	1	1	1	0	1	
1	1	1									
0	1	1									
1	0	1									

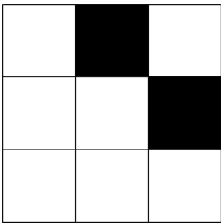
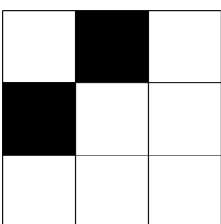
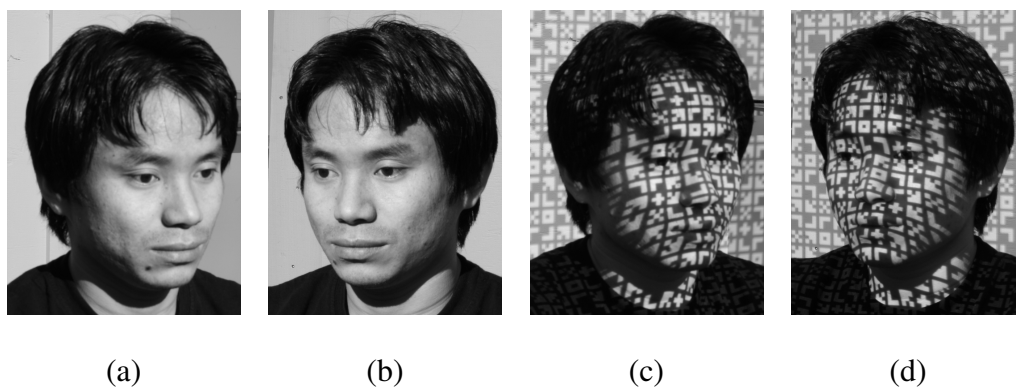
<b>10</b>	<table border="1"> <tbody> <tr><td>1</td><td>0</td><td>1</td></tr> <tr><td>1</td><td>1</td><td>0</td></tr> <tr><td>1</td><td>1</td><td>1</td></tr> </tbody> </table>	1	0	1	1	1	0	1	1	1	
1	0	1									
1	1	0									
1	1	1									
<b>11</b>	<table border="1"> <tbody> <tr><td>1</td><td>0</td><td>1</td></tr> <tr><td>0</td><td>1</td><td>1</td></tr> <tr><td>1</td><td>1</td><td>1</td></tr> </tbody> </table>	1	0	1	0	1	1	1	1	1	
1	0	1									
0	1	1									
1	1	1									

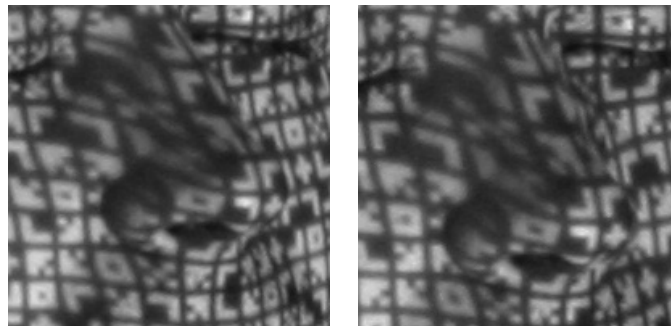
Figure 3.14 shows another example of a human face imaged without and with a projected pattern. In the stereo pairs without the projected pattern, it would be difficult to identify conjugate points, because the face has homogeneous surface texture. However, by projecting the pattern on the surface, there would be thousands of conjugate points that could be identified reliably.



**Figure 3.14** Example stereo pairs of a human face taken without (a-b), and with (c-d) a projected pattern

### 3.4 Balance between intersection accuracy and matching reliability

The previous two sections discussed the necessary system prerequisites prior to and during the data collection. This section addresses the prerequisite for optimal processing. In particular, the geometric setup of the cameras must be taken into consideration so that the system can achieve an accurate and reliable reconstruction solution. In order to solve for the 3D object space coordinates of points on the torso surface, these points must be first identified in image space. The identification of conjugate points in overlapping images is preferably done through an automated matching procedure in order to speed up the processing time and also to minimize the level of expertise required. In automatic image matching, conjugate points are identified through a measure that quantifies the degree of similarity between regions in the overlapping areas of the images. Therefore, the closer two camera stations are positioned, the more similar the two images would appear (see Figure 3.15a and Figure 3.15b), and the more reliable the automated matching procedure would become. This is why a short baseline between two cameras is ideal when it comes to automated image matching.



(a)

(b)

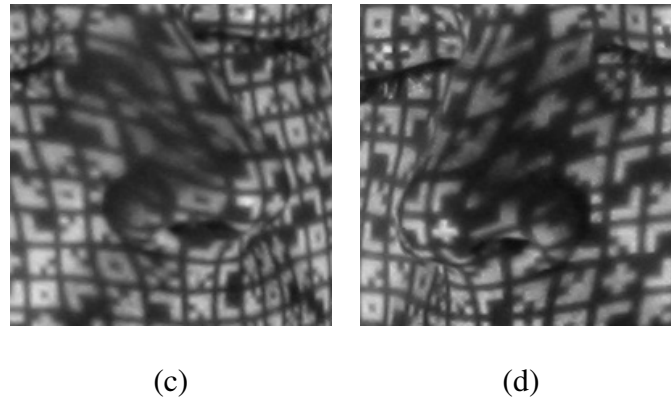


**Figure 3.15 Small differences in relief displacement between images with a short baseline (a-b); significant differences in relief displacement between images with a large baseline (c-d);**

Source: Chang (2008)

On the other hand, the baseline between two camera stations in stereo photogrammetry must be sufficiently large so that the intersection angle of two conjugate light rays is as close to  $90^\circ$  as possible. According to equation (3.4), at a constant depth (i.e. the distance between the cameras and the object to be reconstructed),  $Z$ , the depth precision,  $\sigma_z$ , improves with the increase of the baseline distance,  $B$ , until the light rays coming from the perspective centres of the two cameras form a right angle triangle (see also Figure 3.16a and Figure 3.16b) (Förstner et al., 2004).

$$\sigma_z = \sqrt{2} \cdot \frac{s}{B/Z} \cdot \sigma_{xy} \quad (3.4)$$

where:

$s = \frac{Z}{c}$ , is the image scale, and

$\sigma_{xy}$  is the image point measurement precision

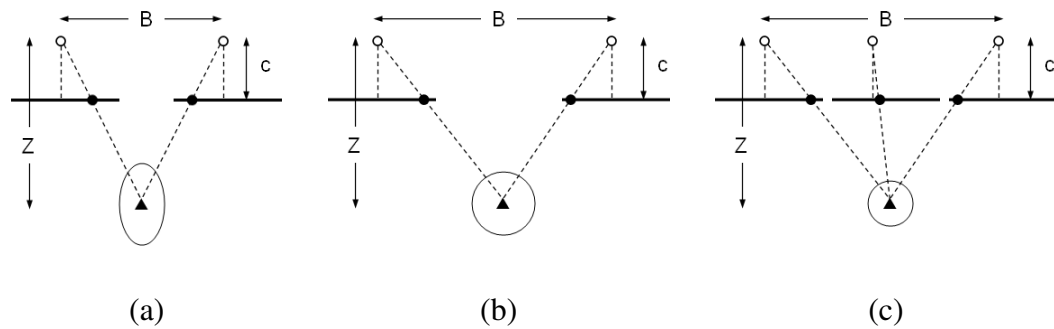


**Figure 3.16 Intersection of conjugate light rays with a short baseline between the two camera perspective centres (a); intersection of two conjugate light rays at an angle close to  $90^\circ$  (b); multiple light ray intersection (c)**

Thus, this large baseline camera station geometry optimizes the intersection accuracy.

For example, in Figure 3.17, notice how the surface reconstruction in the case of a large baseline has less noise and clearer features compared to the one in the case of a short baseline. However, in the large baseline scenario, significant relief displacement is usually present, and this causes occlusion problems in the images. For example, see how the right side of the nose is not visible in the left image in Figure 3.15c and vice versa in Figure 3.15d. Thus, the automated image matching could become quite problematic (Okutomi and Kanade, 1993). In such cases, undesired manual operator intervention is required to double-check the reliability of the results. This is why, in the proposed system, the torso is simultaneously photographed using multiple cameras from different viewpoints, which are close together, and automatic image matching is performed between the adjacent exposure stations with short baselines. After that, conjugate points are tracked through all images, and every point is reconstructed through a conjugate light ray intersection from multiple images (see Figure 3.16c). In this manner, the procedure generates a surface model by taking advantage of the reliable matching in the images

with a short baseline and the accurate multiple light ray intersection from the images with a large baseline. In addition, multiple light ray intersection increases the redundancy and it improves the ability to detect blunders in the 3D coordinate computations.

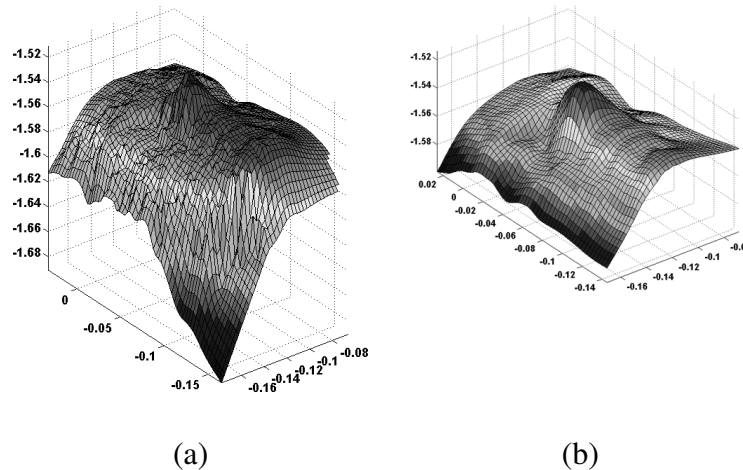


**Figure 3.17** Surface reconstructed using a stereo pair with an intersection angle smaller than  $45^\circ$  ( $B = 0.3\text{m}$ , and  $Z = 1.6\text{m}$ ) (a); surface reconstructed using a stereo pair with a larger baseline ( $B = 1.3\text{m}$ , and  $Z = 1.4\text{m}$ ) (b)

Source: Chang (2008)

### 3.5 Summary of the proposed system design

This chapter explained the design of the proposed photogrammetric system for 3D reconstruction of the torso surface of a scoliotic patient. First, the system setup was described. Then, the prerequisites for optimal functionality, such as system calibration, camera synchronization and pattern projection, were explained. The section on the system calibration included an explanation of camera calibration, camera stability analysis, and exterior orientation parameter determination. The chapter ended with a discussion on the balance between intersection accuracy and matching reliability. It was concluded that multiple light ray intersection is necessary in order to have high accuracy

and reliable automatic image matching at the same time. The next chapter discusses the proposed processing methodology in more detail.

## Chapter Four: Processing Methodology

This chapter addresses the necessary components of the processing methodology, i.e. how the image data is processed once it is collected by the system, in order to generate the desired 3D surface model of the entire torso. The first major processing task is to perform the partial reconstruction of the torso surface model for each of the four sensor arms. This is achieved by:

- carrying out corner detection on every image,
- doing image matching for every stereopair in order to identify conjugate corner points,
- tracking the same matched corners through the neighbouring stereopairs, and
- finally, intersecting the multiple light rays coming from the tracked corners.

Each piece of the partial torso surface model is defined in the reference frame of its corresponding sensor arm. Therefore, the four reconstructed surface models are in four different reference frames. Also, the relationship between these reference frames cannot be assumed to be rigid. This is, because one or two of the sensor arms would be moving up and down whenever a patient enters the system for data collection. This is why the second major processing task is to register these four surface models in the same reference frame. The surface registration is achieved in two phases. First, the neighbouring surfaces are initially registered to each other through a pairwise surface registration process, which establishes the initial transformation parameters between the involved surfaces and also the correspondence between conjugate surface elements in the overlapping areas. Then, global fine tuning of the alignment between all the surfaces is

performed through a multiple surface registration process. The proposed procedure for the 3D torso model generation is summarized in Figure 4.1 and is explained further in the following sections.

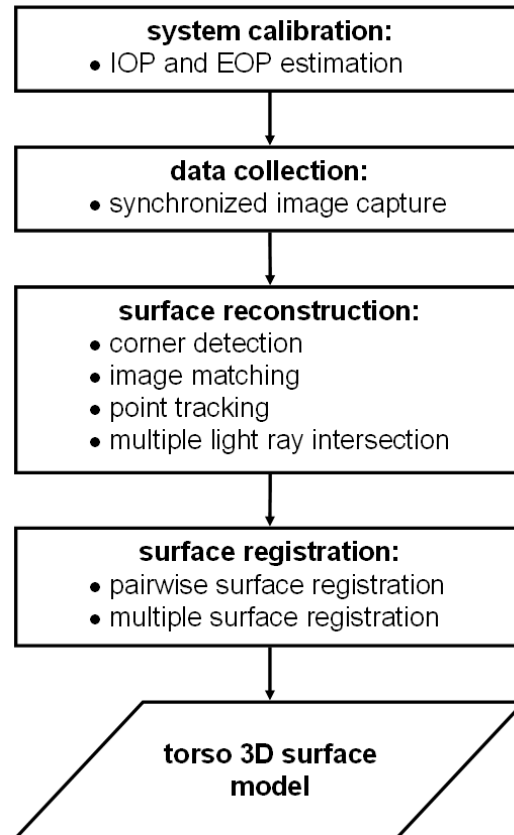


**Figure 4.1** The proposed procedure for 3D surface reconstruction

#### 4.1 Surface reconstruction

In order to optimize the total processing time, the corner detection and the image matching are restricted to a region of interest (ROI), i.e. the region occupied by the torso, and the image space outside of this region is ignored. The region of interest is manually defined by the user through a digitization process, and the output is a binary mask (see Figure 4.2). The rest of the surface reconstruction processing is automated.

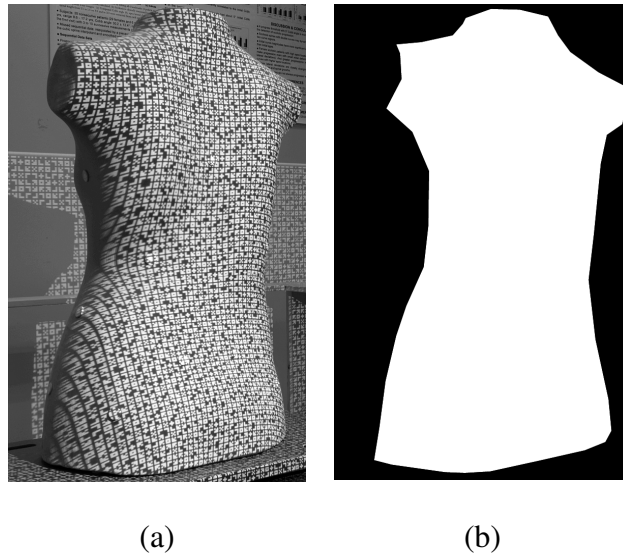


**Figure 4.2** Example of an original image of an artificial torso mannequin (a), and a region of interest mask (b)

#### ***4.1.1 Corner detection and image matching***

The first step in the surface reconstruction processing is identifying features of interest in every image. In the case of the proposed system, the features of interest are the corners in the projected pattern, and they are extracted using the Harris operator (Harris and Stephens, 1988). The parameters involved in the Harris operator include a corner strength threshold, a sigma value for generating a Gaussian smoothing filter, and a radius value for non-maximal suppression. Further on, the image matching algorithm of choice for the proposed system is based on normalized cross correlation (NCC), which is an efficient technique for performing area-based matching. The idea is that a template in one image is compared to a matching window in another image (see Figure 4.3). The matching window moves within a search window, and the location with highest normalized cross correlation coefficient is considered the correct match (Schenk, 1999).

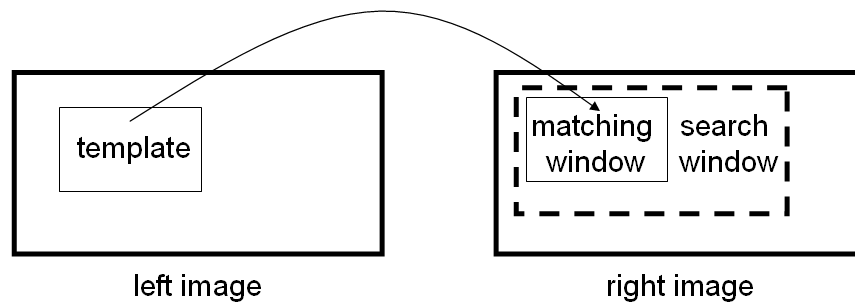
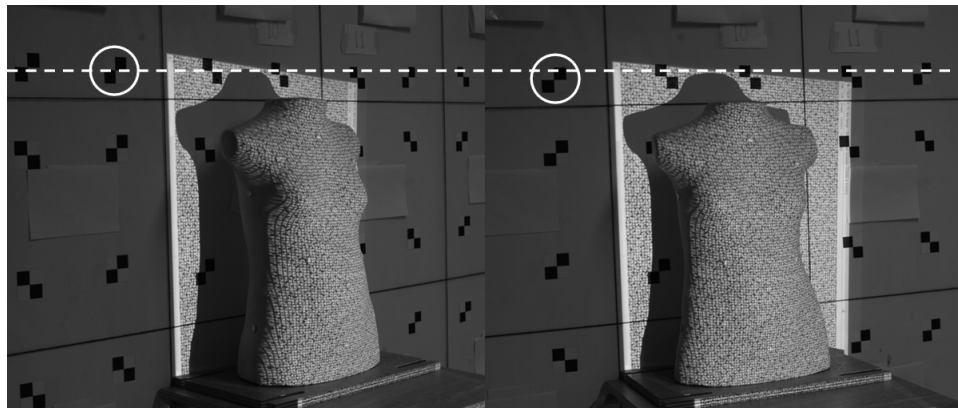


**Figure 4.3 Illustration of area-based image matching**

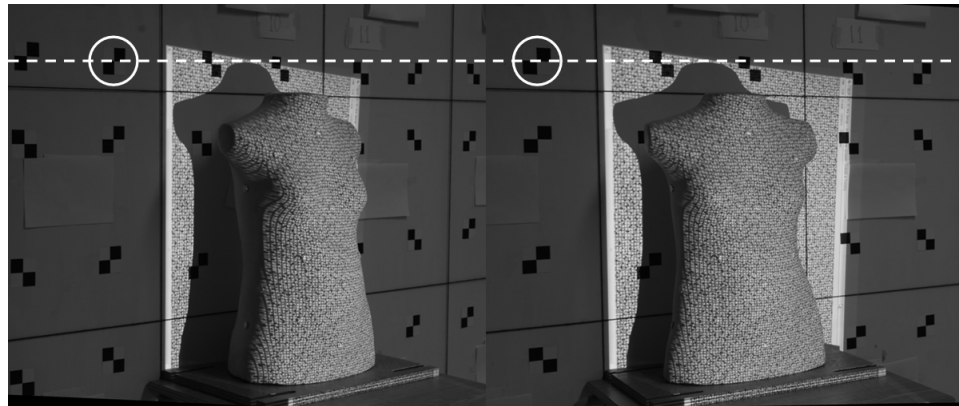
In the proposed system, the template is centred at a detected corner in the left image, and the moving matching window jumps through the detected corners within the search window in the right image. Without any a-priori information, the location and the size of the search window are only constrained to the previously selected ROI. In cases when high megapixel cameras are used, this ROI could end up being fairly large. This would prolong the time necessary for processing, and at the same time create potential risk of matching ambiguities. Therefore, in order to decrease computational time and to avoid any matching ambiguities, it is necessary to reduce the search window as much as possible. This is accomplished by applying two preprocessing steps: first, the y-parallax is eliminated to constrain the search window in the row direction, and second, the x-parallax is predicted in order to constrain the search window in the column direction. The former is accomplished by performing epipolar resampling, and the latter by employing a hierarchical matching strategy. These two concepts are explained in the following two subsections.

#### 4.1.1.1 Epipolar resampling

Raw stereo image pairs contain y-parallax. This means that the y-pixel values of points in the left image would not equal the y-pixel values of the same points in the right image. Figure 4.4a visually describes this problem. The objective of the epipolar resampling is to generate normalized image pairs where corresponding points appear on the same row of the two images (see Figure 4.4b), i.e. the y-parallax is removed (Cho *et al.*, 1992; Morgan *et al.*, 2006). The required pieces of information for the epipolar resampling include the EOPs of the exposure stations and the IOPs of the involved cameras and are estimated from the system calibration. In order for the proposed system to be able to handle the impact of potential errors in the IOPs and EOPs, the size of the search window in the row direction is chosen to be slightly larger than the size of the template.



(a)



(b)

**Figure 4.4 Conjugate points appear on different rows in the original stereopair (a), and on the same row after normalization according to epipolar geometry (b)**

#### 4.1.1.2 Hierarchical matching strategy

After the epipolar transformation, the normalized image pairs would not have y-parallax any longer. However, they would still contain x-parallax. This means that the x-pixel values for points in the left image would not equal the x-pixel values of their corresponding points in the right image. For example, if a normalized image pair is examined manually, it could be noticed that there is a wide range of x-parallax values for conjugate points. Figure 4.5 shows that on the left side of the imaged object the x-parallax value of a conjugate point pair is more than 100 pixels, at the centre of the imaged object the x-parallax value is close to zero pixels, and on the right side – it is over 200 pixels. The idea behind a hierarchical matching strategy is to perform the matching process iteratively. More specifically, at each iteration, the x-parallax of any matched conjugate points is calculated, and its value is used as a prediction to aid the matching process in the subsequent iteration. The hierarchical matching strategy proposed in this research work is similar to the use of image pyramids for the matching of aerial

photographs, which is a common way of speeding up the generation of digital surface models (Ackermann and Hahn, 1991). However, instead of resampling the images from coarse to fine resolution, the density of the corner detection at every matching iteration is controlled.

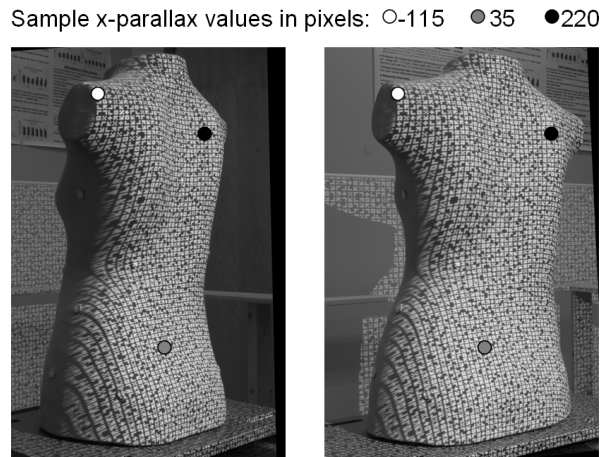
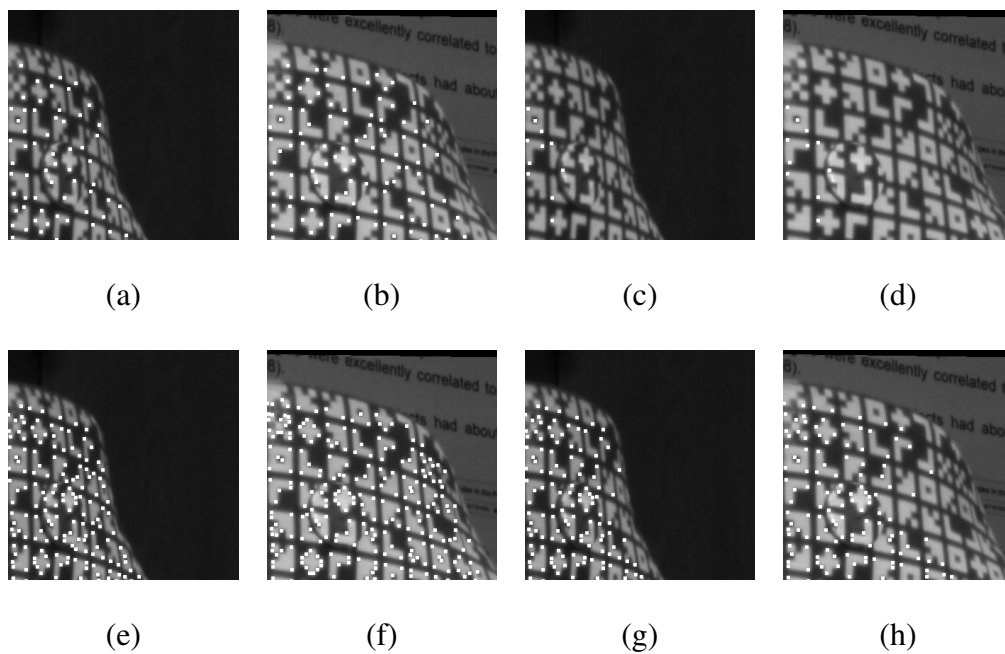


**Figure 4.5 Example of a normalized stereo pair, where sample corresponding points in the left and right images have significantly different x-parallax values**

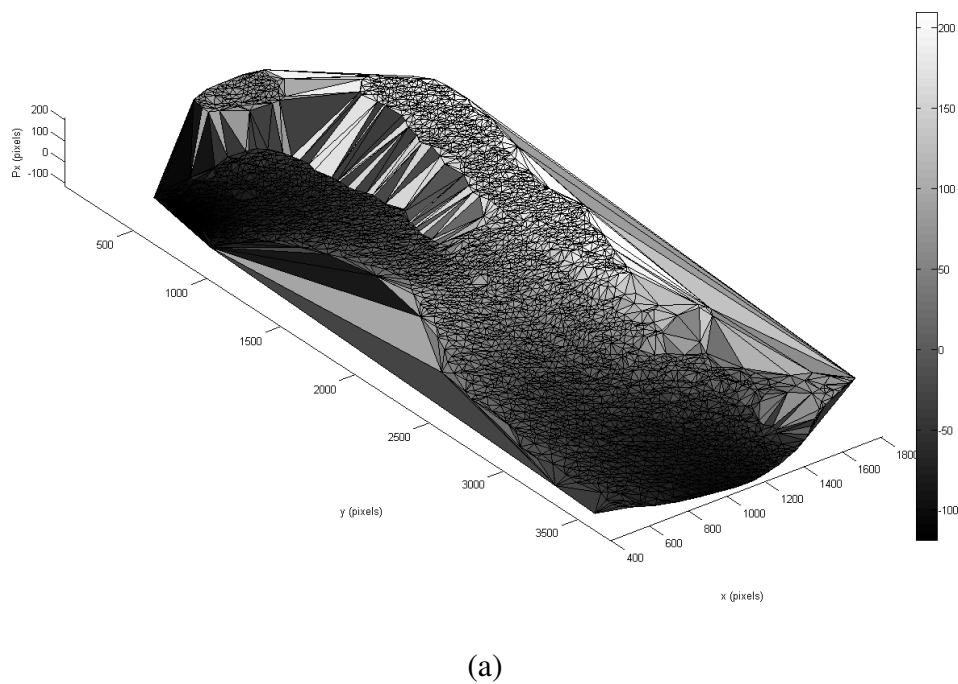
In the first iteration, without any knowledge of the x-parallax, a value of zero is assumed. This means that the search window in the right image is centred at the same location as the template in the left image. However, the two images are not taken from the same position, i.e. the x-parallax is not zero. This is why a large search window must be used to compensate for its incorrect location, and also a large template window must be used to avoid any potential matching ambiguities. Having large search and template windows increases the time necessary to perform computations, so this is why fewer points or lower corner density must be used initially. After the matching process in the first iteration is finished, the x-parallax between any matched corners could be used to better approximate the location of the search window for corners to be matched in the

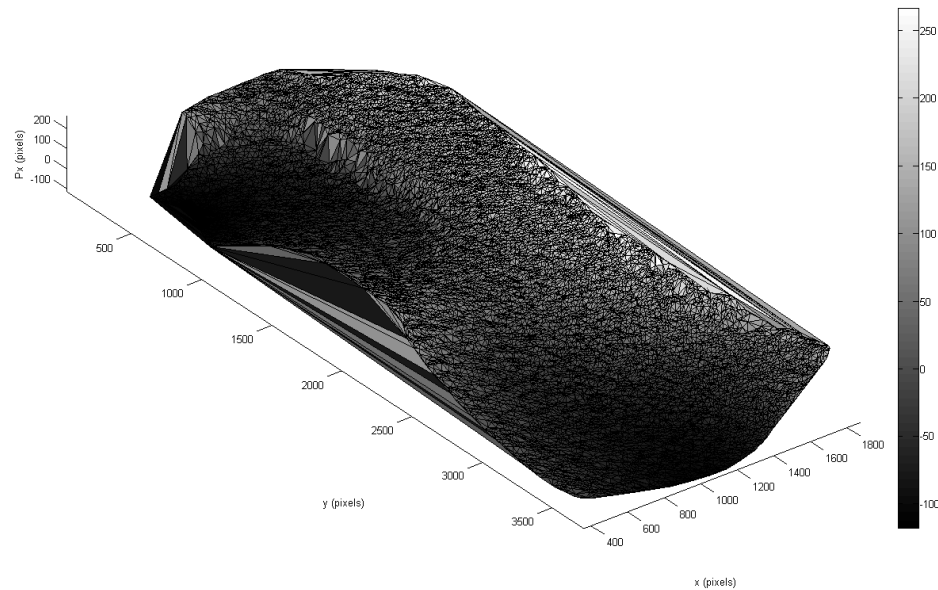
next iteration. More points or higher corner density is used for the subsequent iteration, but since the approximate location of the search window is now better known, its size and the size of the template window, are reduced to optimize the processing time. The sequence of operations in the algorithm is the following:

1. Detect a few very reliable corners by increasing the corner strength threshold, the radius for non-maximal suppression and the Gaussian smoothing parameters (see Figure 4.6a and Figure 4.6b);
2. Match detected corners assuming zero x-parallax and using large search and template windows (see Figure 4.6c and Figure 4.6d);
3. Estimate the x-parallax of the matched corners, and record the values in a look-up table (see Figure 4.7a for a visual example of x-parallax values);
4. Detect more corners by relaxing the Harris operator parameters (see Figure 4.6e and Figure 4.6f);
5. Assign approximate x-parallax values to the detected corners based on the established look-up table in step three;
6. Match again by using the approximate x-parallax values and smaller search and template windows (see Figure 4.6g and Figure 4.6h).
7. Repeat steps three to six until enough point density to represent the torso is reached (see Figure 4.7b for an example of the increased density of x-parallax values).



**Figure 4.6 Hierarchical image matching examples for a given stereopair: first iteration – detected corners in the left (a) and right (b) images, and matched corners in the left (c) and right (d) images; second iteration – detected corners in the left (e) and right (f) images, and matched corners in the left (g) and right (h) images**





(b)

**Figure 4.7 Sample look-up tables of x-parallax values: after first iteration (a), and after second iteration (b)**

#### ***4.1.2 Tracking and intersection***

After the image matching is performed for a given sensor arm, corner tracking is done to identify the same corners in all the images they appear in. Effectively, the tracking procedure yields the image coordinates of conjugate corners in the overlapping imagery, which are needed for the multiple light ray intersection. Using the IOPs of the involved cameras and the EOPs of the involved images, these image coordinates are included in a least squares adjustment to determine the object coordinates of the corresponding points on the torso surface. There are two filters that are currently incorporated in the algorithm. The first one removes any blunders or outliers (i.e. average image coordinate residuals larger than two pixels), and the second one removes points with low intersection precision (i.e. the number of images for a tracked point should be at

least three). Figure 4.8 shows an example for the reconstruction results from one of the sensor arms in the proposed system. This same process is then repeated for the other three sensor arms.

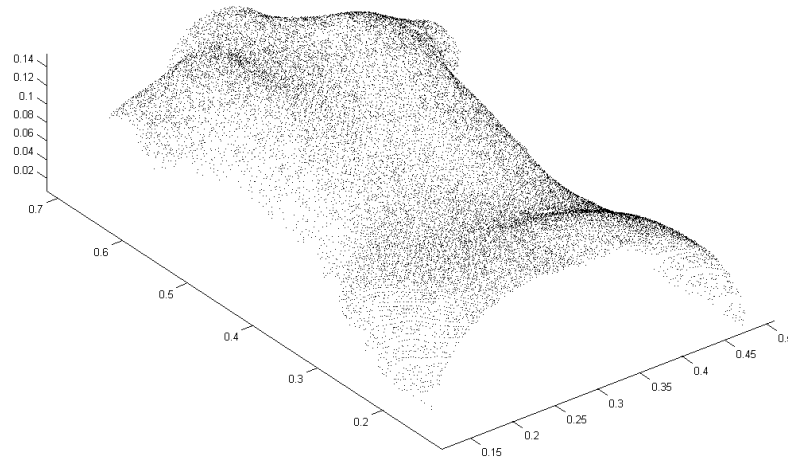


**Figure 4.8 Example of a reconstructed surface, i.e. the back side of an artificial torso mannequin, from one of the sensor arms**

Source: Habib *et al.* (2010a)

## 4.2 Surface registration

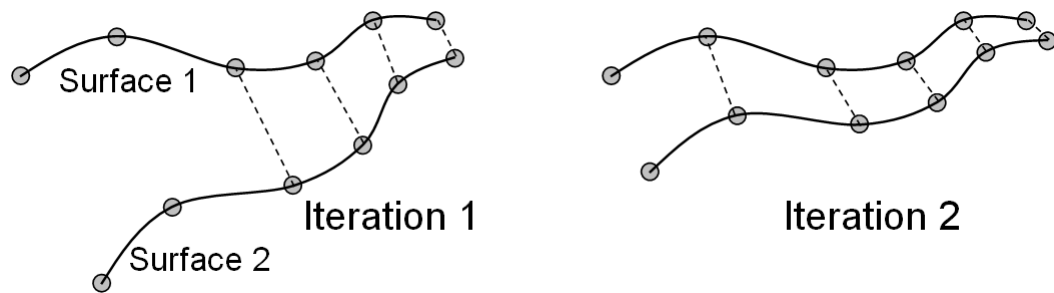
As stated in the proposed system design, each of the four sensor arms yields a surface model in its corresponding reference frame. Also, at least one of the sensor arms is rotated up and down in order for the patient to be able to enter the system for data acquisition. This is why a rigid relationship between the sensor arms cannot be assumed. In order to reconstruct the entire torso, the four surface models have to be registered in a common reference frame. Thus, the integration of the multiple surface models, is a registration procedure. In general, the elements of the registration paradigm could be classified in four categories (Fonseca and Manjunath, 1996):

- geometric primitives,

- transformation function,
- similarity measure, and
- matching strategy.

The primitives are the domain in which information is extracted from the input data, e.g. points, lines, planes, triangular patches, etc. The transformation function is what mathematically describes the mapping process between the reference frames of the datasets being registered, e.g. a 3D similarity transformation. The similarity measure is the necessary constraint for ensuring the correspondence of conjugate primitives. Finally, the matching strategy is the controlling framework that uses the primitives, the transformation function, and the similarity measure to solve the registration problem (Brown, 1992).

A well-known algorithm for registering point clouds is the iterative closest point, also known as ICP (Besl and McKay, 1992). In the light of registration paradigm definitions, the ICP method uses points as the geometric primitives, it applies a 3D similarity transformation as the transformation function, and in terms of the similarity measure, it minimizes Euclidean distances between conjugate points in two overlapping surface models (see Figure 4.9a).



(a)

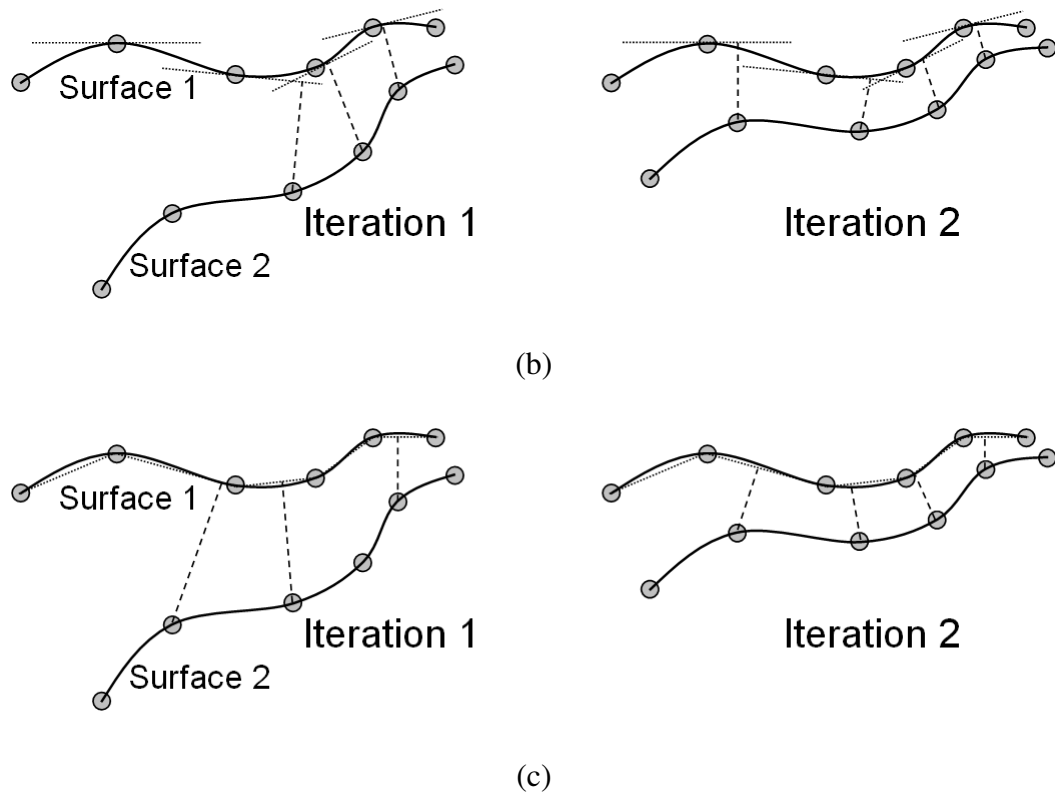


**Figure 4.9 Examples of point cloud registration algorithms in 2D: minimizing distances between points and points (i.e. ICPoint) (a), points and planes (i.e. ICPlane) (b), and points and triangular patches (i.e. ICPatch) (c)**

The matching strategy is implemented in an iterative manner. More specifically, starting from an approximate estimate of the parameters of the transformation function relating two point clouds, hypothesized conjugate points are made by identifying the closest point in one of the datasets to a transformed point from the second one. Hypothesized matches are generated for all the points in the overlap area. These matches are then used to estimate a refined estimate of the transformation function parameters, which are then used to derive a new set of hypothesized matches. The process of hypothesized-match generation and parameters estimation are repeated until the transformation parameters converge. However, when dealing with irregular point clouds exact point-to-point

correspondences between surface models cannot be guaranteed. Some variations of the ICP algorithm, which employ more appropriate geometric primitives, exist. For example, Chen and Medioni (1992) minimized the normal distance between points in one surface model and planes in another surface model (see Figure 4.9b). Such point-to-plane correspondence may be assumed to exist, however, the algorithm requires local plane fitting.

This research work uses another algorithm for performing surface registration of irregular point clouds. It uses point-to-patch correspondence, where points in one surface model and triangular irregular network (TIN) patches in another surface model serve as the geometric primitives (see Figure 4.9c). This choice of geometric primitives does not assume existing point-to-point correspondence, and at the same time, it does not require any local fitting. The only preprocessing that is necessary is the generation of the TIN patches, which is a common function in most geographical information systems (GIS). This algorithm could be implemented in two ways. Both approaches use the same geometric primitives, transformation function and matching strategy. The only difference is the similarity measure used in the implementation of the least-squares algorithm when solving for the registration transformation parameters. These two methods are referred to as the coplanarity constraint and the modified weight matrix, and the rest of this section describes them in detail. In addition, the section also explains how the two methods are extended to handle not only pairwise registration between two overlapping surface models, but also multiple surface registration in a network mode. Such multiple surface registration is necessary in order to minimize any error propagating from the pairwise surface registration.

#### 4.2.1 Pairwise surface registration

Due to the irregular nature of point clouds describing surface models generated from close range photogrammetry, exact point-to-point correspondence cannot be assumed. In this research work, the geometric primitives chosen for the registration of point clouds are points and triangular patches. Thus, for any two overlapping surface models, one of the point clouds is kept as is, and the other one is converted to a TIN, i.e. one of the surface models is represented by the original points, and the other surface model is represented by the triangular patches from the TIN. It is important to note that the TIN patches are an acceptable primitive only in the cases when the TIN model represents the true physical surface of the reconstructed object of interest (Habib et al., 2010b). This means that the surface models have to have point density high enough that no triangles are built across what would be a breakline. If this is true, then it can be assumed that point-to-patch correspondence between the overlapping surface models does exist (see Figure 4.10). In order to deal with cases where the TIN does not represent the physical surface (e.g. sparse areas in the point clouds), a threshold is implemented in the matching strategy (explained later on in this subsection). So, if it is safe to assume that point P in surface one ( $S_1$ ) corresponds to the triangular patch with vertices  $V_1$ ,  $V_2$ , and  $V_3$  in surface two ( $S_2$ ), then this point should coincide with the patch after applying the transformation parameters in equation (4.1).

$$\begin{bmatrix} X_{P'} \\ Y_{P'} \\ Z_{P'} \end{bmatrix} = \begin{bmatrix} X_T \\ Y_T \\ Z_T \end{bmatrix} + s \cdot \mathbf{R}_{3 \times 3}(\omega, \phi, \kappa) \cdot \begin{bmatrix} X_P \\ Y_P \\ Z_P \end{bmatrix} \quad (4.1)$$

where:

$X_P, Y_P, Z_P$  are the coordinates of point  $P$

$X_T, Y_T, Z_T$  are the translation parameters

$R$  is the rotation matrix defined by angles  $\omega, \varphi, \kappa$

$s$  is the scale factor

$X_{P'}, Y_{P'}, Z_{P'}$  are the coordinates of the transformed point  $P'$

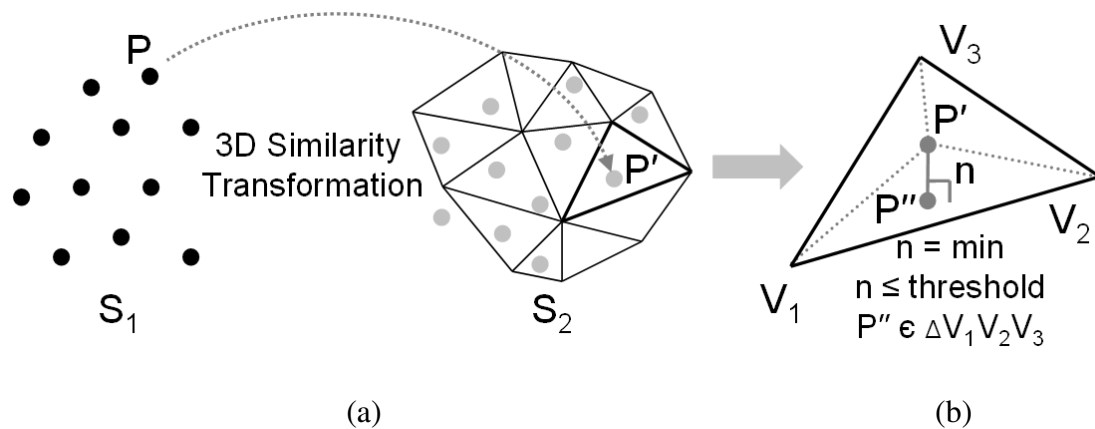


**Figure 4.10** Surface model representation (a), and criteria for accepting correspondence between conjugate primitives (b)

Source: Habib *et al.* (2010a)

The correct correspondence between points in surface  $S_1$  and triangular patches in surface  $S_2$  is established through an iterative procedure. A point-patch pair is considered a valid conjugate match under three conditions (see Figure 4.10b). First, the particular triangular patch,  $\Delta V_1 V_2 V_3$ , must be the closest to the transformed point of interest,  $P'$ . Second, the normal distance,  $n$ , from the transformed point,  $P'$ , to the patch must be within a certain threshold. This is the threshold mentioned earlier, which is incorporated in order to be able to deal with cases where the TIN patches does not represent the physical surface. Lastly, the projection of the transformed point onto the patch,  $P''$ , must be inside the patch. The iterative procedure progresses as follows: first, initial point-patch

pairs are determined after applying approximate transformation parameters, which bring  $S_1$  in the reference frame of  $S_2$  (see Figure 4.10a); then, these initial point-patch pairs are used to calculate a better estimate of the transformation parameters between  $S_1$  and  $S_2$ ; and the updated transformation parameters are used to determine a new set of point-patch pairs. The procedure is repeated until the transformation parameters converge, and there is no change in the point-patch correspondence. At the end of this registration procedure the goodness of fit between the two surfaces is evaluated by calculating the average normal distance for all the matched point-patch pairs (Habib et al., 2009). So far, the choice of geometric primitives, the transformation function, and the matching strategy for the pairwise surface registration has been described. The rest of this section explains the similarity measures used in the calculation of the registration transformation parameters for the coplanarity constraint and the modified weight matrix methods in the pairwise surface registration.

#### 4.2.1.1 Coplanarity constraint method for the pairwise surface registration

In the coplanarity constraint method,  $P'$ ,  $V_1$ ,  $V_2$ , and  $V_3$  are assumed to be coplanar. This means that the volume of the pyramid, whose vertices are  $P'$ ,  $V_1$ ,  $V_2$ , and  $V_3$  in Figure 4.10b, should be zero. This can be mathematically expressed as the determinant in equation (4.2).

$$\det \begin{bmatrix} X_{P'} & Y_{P'} & Z_{P'} & 1 \\ X_{V_1} & Y_{V_1} & Z_{V_1} & 1 \\ X_{V_2} & Y_{V_2} & Z_{V_2} & 1 \\ X_{V_3} & Y_{V_3} & Z_{V_3} & 1 \end{bmatrix} = 0 \quad (4.2)$$

Equation (4.2) is a function of the vector of unknown parameters,  $x$  (i.e. the transformation parameters), and the vector of observations,  $\ell$  (i.e. the coordinates of  $P^i$ ,  $V_1$ ,  $V_2$ , and  $V_3$ ), with an assumed known variance-covariance matrix for the observations,  $C_\ell$ , and an unknown variance-covariance matrix for the unknowns,  $C_x = 0$ :

$$f(x^0 + \hat{\delta}, \ell + \hat{r}) = 0, C_\ell \quad (4.3)$$

where the variance-covariance matrix of the observations is the product of the a-priori variance factor and the inverse of the weight matrix for the observations, i.e.

$$C_\ell = \sigma_0^2 \cdot P_\ell^{-1}$$

The least squares problem is to minimize the sum of the squared observation residuals:

$$\min(\hat{r}^T \cdot P_\ell \cdot \hat{r}) \quad (4.4)$$

subject to:

$$A \cdot \hat{\delta} + B \cdot \hat{r} + w = 0, \quad (4.5)$$

where:

$A$  is the design matrix of partial derivatives with respect to the unknown parameters, i.e.  $A = \frac{\partial f}{\partial x}$ ,

$\hat{\delta}$  is the vector of corrections for the approximate values of the unknown parameters,  $x^0$ , i.e.  $\hat{x} = x^0 + \hat{\delta}$ ,

$B$  is the design matrix of partial derivatives with respect to the observations, i.e.

$$B = \frac{\partial f}{\partial \ell}, \text{ and}$$

$w$  is the misclosure vector evaluated with the approximate values of the unknown parameters and the observations, i.e.  $w = f(x^0, \ell)$ .

The corrections for the approximate values of the unknown parameters are solved by using the following expression:

$$\hat{\delta}_{\text{mx1}} = - N_{\text{mxm}}^{-1} \cdot u_{\text{mx1}}, \quad (4.6)$$

where:

$m$  is the number of unknowns, which in this case equals seven (i.e.  $m = 7$ )

$N$  is the normal matrix, and

$u$  is the normal vector.

The normal matrix,  $N$ , and the normal vector,  $u$ , are populated through a process known as the summation of normals:

$$N_{\text{mxm}} = \sum_{i=1}^n \left( A_i^T \cdot \left( B_i \cdot C_\ell \cdot B_i^T \right)^{-1} \cdot A_i \right) \quad (4.7)$$

$$u_{\text{mx1}} = \sum_{i=1}^n \left( A_i^T \cdot \left( B_i \cdot C_\ell \cdot B_i^T \right)^{-1} \cdot w_i \right), \quad (4.8)$$

where:

$n$  is the number of observation equations, i.e. the number of conjugate point-patch pairs, and  $i$  is the particular point-patch pair used for populating  $A_i$ ,  $B_i$  and  $w_i$ .

The solution iterates until there is no significant change in the value for the a-posteriori variance factor between consecutive iterations. The a-posteriori variance factor is calculated as follows:

$$\hat{\sigma}_0^2 = \frac{\hat{\mathbf{r}}^T \cdot \mathbf{P}_\ell \cdot \hat{\mathbf{r}}}{n - m}, \quad (4.9)$$

By using numerous point-patch pairs, which satisfy this coplanarity constraint, the transformation parameters relating the two surface models can be estimated through the above described least squares adjustment. In order to obtain reliable estimates of these transformation parameters, variations in the topography of the surfaces are needed so that there are constraints in as many directions as possible.

#### 4.2.1.2 Modified weight matrix method for the pairwise surface registration

In the modified weight matrix method, the transformation function in equation (4.1) is used together with the similarity measure (or the functional model) shown in equation (4.10) as the basis for the complete stochastic model used in the adjustment.

$$\begin{bmatrix} X_{V_i} \\ Y_{V_i} \\ Z_{V_i} \end{bmatrix} = \begin{bmatrix} X_{P_i} \\ Y_{P_i} \\ Z_{P_i} \end{bmatrix} \quad (4.10)$$

So if equation (4.1) is substituted in equation (4.10), the complete stochastic model is given in equation (4.11).

$$\begin{bmatrix} X_{V_i} \\ Y_{V_i} \\ Z_{V_i} \end{bmatrix} = \begin{bmatrix} X_T \\ Y_T \\ Z_T \end{bmatrix} + s \cdot \mathbf{R}_{3 \times 3}(\omega, \varphi, \kappa) \cdot \begin{bmatrix} X_P \\ Y_P \\ Z_P \end{bmatrix} + \mathbf{r}_{3 \times 1}, \text{ where } \mathbf{r}_{3 \times 1} \sim (0, \sigma_0^2 \cdot \mathbf{P}_{XYZ}^{-1}) \quad (4.11)$$

where:

$\mathbf{r}$  is the combined vector of observation residuals,  $\mathbf{r}_{3 \times 1} = \mathbf{r}_{V_i} - s \cdot \mathbf{R}_{3 \times 3}(\omega, \varphi, \kappa) \cdot \mathbf{r}_P$ , and

$$\sigma_0^2 \cdot \mathbf{P}_{XYZ}^{-1} = \mathbf{B} \cdot \mathbf{C}_\ell \cdot \mathbf{B}^T.$$

The least squares adjustment for this case follows the concepts explained in equations (4.3) to (4.6), and the normal matrix,  $N$ , and the normal vector,  $u$ , are populated in the following manner:

$$N_{mxm} = \sum_{i=1}^n \left( A_i^T \cdot \begin{pmatrix} B_i \cdot C_\ell \cdot B_i^T \\ 3 \times 6 \quad 6 \times 6 \quad 6 \times 3 \end{pmatrix}^{-1} \cdot A_i \right) \quad (4.12)$$

$$u_{mx1} = \sum_{i=1}^n \left( A_i^T \cdot \begin{pmatrix} B_i \cdot C_\ell \cdot B_i^T \\ 3 \times 6 \quad 6 \times 6 \quad 6 \times 3 \end{pmatrix}^{-1} \cdot w_i \right), \quad (4.13)$$

As seen from equation (4.10), the similarity measure for this surface registration method is a point-based approach, where it is assumed that one of the triangular patch vertices is conjugate to the transformed point  $P'$ . However, such correspondence is not necessarily true. To compensate for the fact that we are using a point-based procedure while using non-conjugate points in a point-patch pair, the weights associated with the similarity measure in equation (4.10) are modified. More specifically, the weight matrix is modified to ensure the minimization of the combined residual vector in a direction normal to the TIN patch in question. In other words, due to the lack of point-to-point correspondence, there would be a spatial offset between point  $P'$  in  $S_1$  and vertex  $V_1$  in  $S_2$  in all three directions. However, the weights in the least-squares adjustment are modified in such a way that the transformation parameters are estimated to minimize the spatial offset normal to the triangular patch. This is accomplished by the following sequence of operations (Aldelgawy et al., 2008):

1. Compute the rotation matrix,  $M$ , which transforms the coordinates of the point from the original coordinate system  $(X,Y,Z)$  to the local coordinate system of the

triangular patch (U,V,W), where the U and V axes are within the patch plane and the W axis is normal to the patch plane (see Figure 4.11)

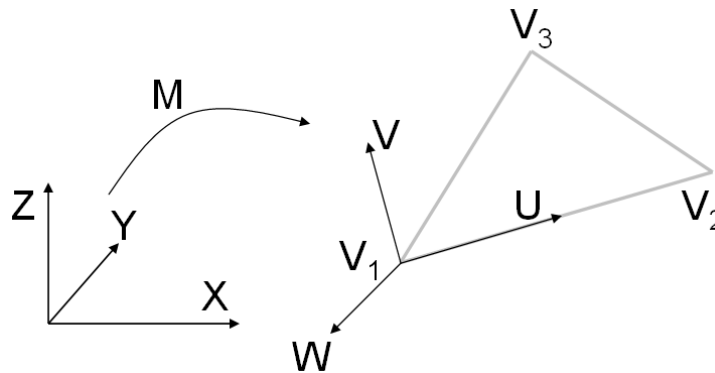


**Figure 4.11 Illustration of the transformation between the (X,Y,Z) and the (U,V,W) coordinate systems**

2. Compute the weight matrix in the (U,V,W) coordinate system according to the law of error propagation:

$$P_{UVW} = M \cdot P_{XYZ} \cdot M^T \quad (4.14)$$

where:

$P_{XYZ}$  is the weight matrix in the (X,Y,Z) coordinate system, and

$P_{UVW}$  is the weight matrix in the (U,V,W) coordinate system

3. Modify the weight matrix in the (U,V,W) coordinate system by assigning zeros for the weights along the triangular patch:

$$P'_{UVW} = \begin{bmatrix} 0 & 0 & 0 \\ 0 & 0 & 0 \\ 0 & 0 & p_w \end{bmatrix} \quad (4.15)$$

4. Compute the modified weight matrix in the (X,Y,Z) coordinate system:

$$P'_{XYZ} = M^T \cdot P'_{UVW} \cdot M \quad (4.16)$$

5. Apply a point-based solution using least squares with the modified weight matrix,  $P'_{XYZ}$ .

Essentially, in the modified weight matrix method, the sum of the squared random residuals along the triangular patch normal, are minimized. Here follows the proof:

- First, assume that the combined residual vector  $r_{XYZ}$  has a random and systematic component:

$$r_{XYZ} = r_{XYZ}^{\text{rand}} + r_{XYZ}^{\text{syst}} \quad (4.17)$$

- Then, apply the target function of the least squares adjustment using the modified weight matrix:

$$(r_{XYZ})^T \cdot P'_{XYZ} \cdot r_{XYZ}, \quad (4.18)$$

- and substitute equations (4.16) and (4.17) in (4.18):

$$(r_{XYZ}^{\text{rand}} + r_{XYZ}^{\text{syst}})^T \cdot M^T \cdot P'_{UVW} \cdot M \cdot (r_{XYZ}^{\text{rand}} + r_{XYZ}^{\text{syst}}). \quad (4.19)$$

- After that, expand (4.19):

$$\begin{aligned} & (r_{XYZ}^{\text{rand}})^T \cdot M^T \cdot P'_{UVW} \cdot M \cdot r_{XYZ}^{\text{rand}} \\ & + 2 \cdot (r_{XYZ}^{\text{rand}})^T \cdot M^T \cdot P'_{UVW} \cdot M \cdot r_{XYZ}^{\text{syst}} \\ & + (r_{XYZ}^{\text{syst}})^T \cdot M^T \cdot P'_{UVW} \cdot M \cdot r_{XYZ}^{\text{syst}}, \end{aligned} \quad (4.20)$$

- and note that

$$M \cdot r_{XYZ}^{\text{syst}} = r_{UVW}^{\text{syst}} = \begin{bmatrix} r_U^{\text{syst}} \\ r_V^{\text{syst}} \\ 0 \end{bmatrix}, \quad (4.21)$$

which means that

$$\mathbf{P}'_{UVW} \cdot \mathbf{M} \cdot \mathbf{r}_{XYZ}^{syst} = \begin{bmatrix} 0 & 0 & 0 \\ 0 & 0 & 0 \\ 0 & 0 & p_w \end{bmatrix} \cdot \begin{bmatrix} \mathbf{r}_U^{syst} \\ \mathbf{r}_V^{syst} \\ 0 \end{bmatrix} = 0, \quad (4.22)$$

and the only term left in (4.20) is one that contains only the random component of the residuals:

$$\begin{aligned} & (\mathbf{r}_{XYZ}^{rand})^T \cdot \mathbf{M}^T \cdot \mathbf{P}'_{UVW} \cdot \mathbf{M} \cdot \mathbf{r}_{XYZ}^{rand} \\ & + 2 \cdot (\mathbf{r}_{XYZ}^{rand})^T \cdot \mathbf{M}^T \cdot \mathbf{P}'_{UVW} \cdot \mathbf{M} \cdot \mathbf{r}_{XYZ}^{syst} \rightarrow 0 \\ & + (\mathbf{r}_{XYZ}^{syst})^T \cdot \mathbf{M}^T \cdot \mathbf{P}'_{UVW} \cdot \mathbf{M} \cdot \mathbf{r}_{XYZ}^{syst} \rightarrow 0. \end{aligned} \quad (4.23)$$

- Finally, simplify (4.23) to:

$$(\mathbf{r}_{XYZ}^{rand})^T \cdot \mathbf{M}^T \cdot \mathbf{P}'_{UVW} \cdot \mathbf{M} \cdot \mathbf{r}_{XYZ}^{rand} = (\mathbf{r}_{UVW}^{rand})^T \cdot \begin{bmatrix} 0 & 0 & 0 \\ 0 & 0 & 0 \\ 0 & 0 & p_w \end{bmatrix} \cdot \mathbf{r}_{UVW}^{rand} = p_w \cdot (\mathbf{r}_W^{rand})^2 \quad (4.24)$$

It is important to note that even though it seems as if there are three observations equations for every point-patch pair, the net contribution of the constraint towards the redundancy estimation is one, because the rank of the modified weight matrix is one. Therefore, the redundancy for this method equals the redundancy of the coplanarity constraint one. Again, as with the coplanarity constraint, in order to obtain reliable estimates of the transformation parameters, variations in the topography of the surfaces are needed so that there are constraints in as many directions as possible. Figure 4.12 illustrates an example of the alignment outcome from the pairwise registration between the reconstructed surface models from two of the sensor arms.

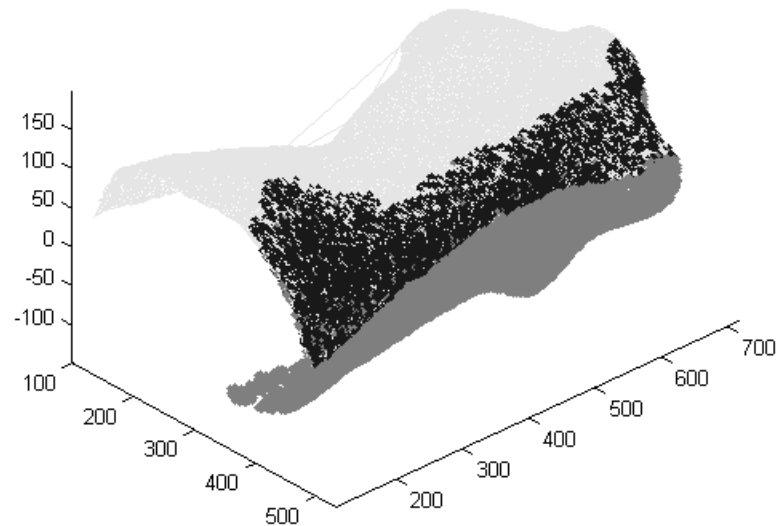


**Figure 4.12** Example of a pairwise registration of two overlapping surfaces (light gray: non-matched area in the TIN surface; black: matched area in the overlap between the point cloud and the TIN surface; dark gray: non-matched area in the point cloud)

#### ***4.2.2 Multiple surface registration***

The previous subsection explained two approaches for registering two overlapping surface models, a procedure referred to as pairwise registration. However, in the case of a full 360° reconstruction of an object, there are multiple surface models covering the volume of interest. Each surface model is in a different reference frame, so it is necessary to register the multiple surfaces in a common reference frame. One way of achieving this is to choose the reference frame of one of the surface models as the common one, and then to sequentially register the rest of the surface models in the pairwise manner described before. However, the first and the last surface models might exhibit incompatibility due to errors propagated through the sequential registration process (see Figure 4.13b). This is similar to a closed loop traverse in surveying, where the constraint that the first and last point coincide, has not been used. To avoid such an

incompatibility and to have a seamless final product, the multiple surface registration has to be performed simultaneously, i.e. in a network mode (see Figure 4.13c).

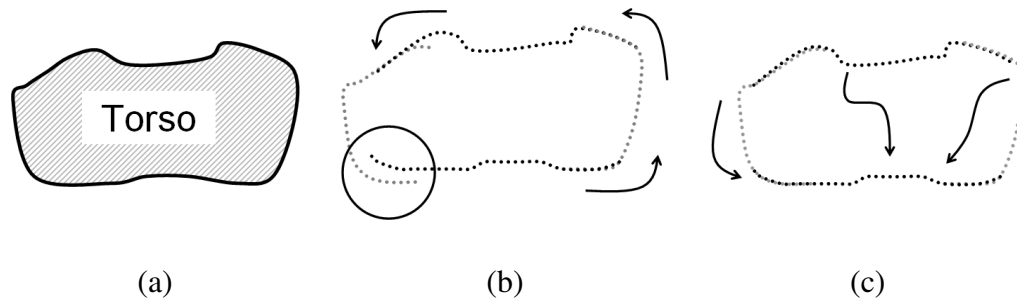


**Figure 4.13 Illustrations of the torso surface (a), sequential pair-wise surface registration (b), and simultaneous multiple surface registration (c) in 2D**

This procedure can be viewed as an extension to the pairwise registration. In particular, the pairwise registration procedure is used to establish a list of the corresponding point-patch pairs and estimate the transformation parameters between any two overlapping surface models. The multiple surface registration, on the other hand, uses these corresponding point-patch pairs, and applies the transformation parameters from the pairwise surface registration as initial approximations, to simultaneously solve for all the final surface transformation parameters. This is done in a least-squares adjustment, where each surface is iteratively transformed to a common reference frame until the sum of the squared normal distances between the conjugate point-patch pairs is minimized. This procedure is highly non-linear, so that is why the initial approximates from the pairwise surface registration are necessary. It is also important to note that the transformation parameters for one of the surface models are kept fixed in order to define the datum for the final surface model. The transformation function for the multiple surface registration is similar to the one in the pairwise surface registration, except both point P, and

triangular patch vertices  $V_1$ ,  $V_2$ , and  $V_3$  for a given conjugate point-patch pair are transformed to the reference frame of choice as shown in equations (4.25) and (4.26).

$$\begin{bmatrix} X_{P'} \\ Y_{P'} \\ Z_{P'} \end{bmatrix} = \begin{bmatrix} X_{T_i} \\ Y_{T_i} \\ Z_{T_i} \end{bmatrix} + s_i \cdot \mathbf{R}_{3 \times 3}(\omega_i, \phi_i, \kappa_i) \cdot \begin{bmatrix} X_P \\ Y_P \\ Z_P \end{bmatrix} \quad (4.25)$$

$$\begin{bmatrix} X_{V_{1,2,3}} \\ Y_{V_{1,2,3}} \\ Z_{V_{1,2,3}} \end{bmatrix} = \begin{bmatrix} X_{T_j} \\ Y_{T_j} \\ Z_{T_j} \end{bmatrix} + s_j \cdot \mathbf{R}_{3 \times 3}(\omega_j, \phi_j, \kappa_j) \cdot \begin{bmatrix} X_{V_{1,2,3}} \\ Y_{V_{1,2,3}} \\ Z_{V_{1,2,3}} \end{bmatrix} \quad (4.26)$$

where:

‘i’ denotes the transformation parameters between the surface represented by points and the common reference frame, and

‘j’ denotes the transformation parameters between the surface represented by triangular patches and common reference frame

The rest of this section explains how the coplanarity constraint and the modified weight matrix methods are applied to solve for the final surface transformation parameters in the multiple surface registration.

#### 4.2.2.1 Coplanarity constraint method for the multiple surface registration

The mathematical model describing the coplanarity constraint for the multiple surface registration is similar to equation (4.2), except that both point P and vertices  $V_1$ ,  $V_2$ , and  $V_3$  are transformed to the common reference frame. So, in this case, the volume of the pyramid with vertices  $P'$ ,  $V_1'$ ,  $V_2'$ , and  $V_3'$  should be zero. Mathematically, this is expressed as the determinant in equation (4.27).

$$\det \begin{bmatrix} X_{p'} & Y_{p'} & Z_{p'} & 1 \\ X_{v_1'} & Y_{v_1'} & Z_{v_1'} & 1 \\ X_{v_2'} & Y_{v_2'} & Z_{v_2'} & 1 \\ X_{v_3'} & Y_{v_3'} & Z_{v_3'} & 1 \end{bmatrix} = 0 \quad (4.27)$$

The least squares adjustment for the solution of this problem follows the concepts explained in equations (4.3) to (4.8), except this time the number of unknowns,  $m$ , is different (e.g. in the case of four sensor arms  $m = 4 \times 7 = 28$  assuming all seven transformation parameters are solved for).

#### 4.2.2.2 Modified weight matrix method for the multiple surface registration

In the modified weight matrix method for the multiple surface registration, the transformation functions in equations (4.25) and (4.26) are used together with the similarity measure (or the functional model) shown in equation (4.28) as the basis for the complete stochastic model used in the adjustment.

$$\begin{bmatrix} X_{v_i'} \\ Y_{v_i'} \\ Z_{v_i'} \end{bmatrix} = \begin{bmatrix} X_{p'} \\ Y_{p'} \\ Z_{p'} \end{bmatrix} \quad (4.28)$$

So if equations (4.25) and (4.26) are substituted in equation (4.28), the complete stochastic model is given in equation (4.29).

$$\begin{bmatrix} X_{v_i} \\ Y_{v_i} \\ Z_{v_i} \end{bmatrix} = \frac{1}{s_j} \cdot \mathbf{R}_{3 \times 3}^T(\omega_j, \phi_j, \kappa_j) \cdot \begin{bmatrix} X_{T_i} \\ Y_{T_i} \\ Z_{T_i} \end{bmatrix} + s_i \cdot \mathbf{R}_{3 \times 3}(\omega_i, \phi_i, \kappa_i) \cdot \begin{bmatrix} X_p \\ Y_p \\ Z_p \end{bmatrix} - \begin{bmatrix} X_{T_j} \\ Y_{T_j} \\ Z_{T_j} \end{bmatrix} + \mathbf{r}_{3 \times 1}, \quad (4.29)$$

where  $\mathbf{r}_{3 \times 1} \sim (0, \sigma_0^2 \cdot \mathbf{P}_{XYZ}^{-1})$ ,

where:

$\mathbf{r}$  is the combined vector of observation residuals,

$$\mathbf{r}_{3 \times 1} = \mathbf{r}_{V_1} - \frac{1}{S_j} \cdot \mathbf{R}_{3 \times 3}^T(\omega_j, \phi_j, \kappa_j) \cdot \mathbf{s}_1 \cdot \mathbf{R}_{3 \times 3}(\omega_1, \phi_1, \kappa_1) \cdot \mathbf{r}_p.$$

The least squares adjustment for this case follows the concepts explained in equations (4.3) to (4.6), and (4.12) and (4.13), except the number of unknowns,  $m$ , again equals 28 in the case of four sensor arms.

Again, due to the lack of point-to-point correspondence, there would be a spatial offset between point  $P$  in  $S_1$  and vertex  $V_1$  in  $S_2$  in all three directions. However, the weights in the least-squares adjustment are modified in such a way that the transformation parameters are estimated through minimizing the component of the spatial offset between non-conjugate points within a point-patch pair along the normal to the triangular patch. This is accomplished by implementing the procedure defined in the previous subsection.

### 4.3 Summary of the processing methodology

This chapter covered the necessary components of the processing methodology in order for the proposed system to generate the desired 3D surface model of the entire torso. The two major processing tasks, i.e. the surface reconstruction and the surface registration, were described in detail. The main emphasis in the surface reconstruction section was the use of a hierarchical matching strategy in the corner detection and image matching workflow, in order to reduce computational time and increase matching reliability. The highlight of the surface registration section was the explanation of the mathematical models behind the coplanarity constraint and especially behind the

modified weight matrix methods for the pairwise and the multiple surface registration. The multiple surface registration procedure completes the data processing steps for the proposed system, and the final result is the entire 3D torso surface model. The next chapter shows the current system implementation, and discusses the experimental results conducted to date.

## **Chapter Five: System Implementation and Experimental Results**

This chapter first shows results from the system calibration, which includes the camera calibration, stability analysis, and the EOP determination. Tests on the type of distortion model, the choice of image space observations, and the options for datum definition are shown as part of the camera calibration. Then, the experimental results comprise the surface reconstruction (by using the currently implemented single sensor arm) of a flat metal plate, two human faces, and most importantly – an artificial torso mannequin. The objectives of the experiments are to test the feasibility of the proposed system for different applications, and to estimate the relative and absolute accuracy of the reconstruction quality. A test on the pattern size, a comparison between using a single and a dual projector setup, and an evaluation between the coplanarity constraint and the modified weight matrix methods for pairwise and multiple surface registration, are incorporated as part of the reconstruction experiments.

### **5.1 Camera calibration**

There were two data collection sessions for the camera calibration experiments. The purpose of the first session was to survey the targets on a portable calibration board. After that, the second session involved photographing the board with all the cameras that would be used for the project. After all the necessary data was collected, there were three calibration experiments conducted for one of the cameras. They dealt with the choices for a distortion model, image space observations and datum definition. Generally, a lens distortion model can be categorized as inadequate, adequate or over-parameterized. An

adequate model has the minimum number of distortion parameters needed to sufficiently describe the inherent distortions for the implemented camera. Insufficient and over-parameterized models should be avoided, because they might have an adverse effect on the reconstructed object space. Thus, the first experiment was to test the necessity of solving for all the lens distortions as opposed to solving for only the first coefficient of radial lens distortion. The second experiment was to test the use of points only against the use of points and linear features as image space observations. Lastly, the third experiment was to test using control points against fixing the coordinates for a few points (in order to define the datum position and orientation) and using distance constraints (in order to define the datum scale). Once the three tests were run, the most efficient technique to calibrate the rest of the cameras was chosen. The rest of this section describes the data collection procedures and the tests that were run in more detail.

#### ***5.1.1 Surveying the portable calibration board***

The surveying of the targets on the calibration board was first done using a high precision total station (see Figure 5.1), and two reflector prisms. According to the manufacturer specifications, the measurement capabilities of the total station were 0.5'' for the horizontal and vertical circle readings, and  $1\text{mm} \pm 1\text{ppm}$  for the electronic distance measurement (EDM) device. Note that the two reflector prisms have had their zero errors previously estimated. The observation points at which the total station was set up were two stable pillars. The portable target board was placed in such a way that the intersection angle between the directions from the two pillars was as close to  $90^\circ$  as possible. Horizontal directions, zenith angles, and slope distances from each pillar to the 35 target points on the board (and to the other pillar) were observed in two rounds. Note

that temperature, atmospheric pressure and humidity were not measured, because the slope distances measured were too short for any atmospheric corrections to have a significant contribution to the measurements. Each round involved both face left (direct), and face right (reverse) observations. The face left and face right observations were reduced for each round, and the two rounds were averaged after verifying that the observations were within the allowable discrepancies. After that, the averaged observations were fed into a surveying network adjustment in order to solve for the 3D coordinates of the target points. The standard deviations for the 3D coordinates were  $\pm 0.1\text{mm}$  for X, Y and Z. This method for surveying the target points was very cumbersome, and the combined time for data collection and processing took over two days. Another approach to survey the calibration board was to simply measure distances between selected points. Thus, ten distances between nine of the target points were measured using a construction quality tape measure, which had smallest graduation of 1mm. This was done twice by two different operators in order to avoid any reading blunders. However, note that neither the zero, nor the scale errors of the tape were estimated in order to keep this part of the experiment as simple as possible. The total time did not exceed 10-15 minutes, and the average of the differences in the distances measured with the tape measure and the ones calculated from the total station coordinates was 0.6mm with a standard deviation of  $\pm 0.3\text{mm}$ .

### ***5.1.2 Image collection for the camera calibration***

During the second data collection session the portable calibration board was photographed by the seven cameras currently available for the system. The cameras used were entry level digital single-lens reflex (DSLR) ones. The make and the model of the

cameras was Canon Rebel XS (also known as EOS 1000D). Each camera had a 22.2mm x 14.8mm complimentary metal oxide semiconductor (CMOS) solid state sensor. The output images had 3888 rows and 2592 columns or 10.1 effective megapixels, where the pixel size was 5.7 $\mu$ m. The camera lenses had a nominal focal length of 35mm. The image stabilization, the automatic focus, and the sensor cleaning functions of the cameras were turned off to ensure the validity of the established parameters for subsequent datasets. In addition, the zoom and focus rings were taped so that the focal length stayed fixed. Images were taken from three locations – left, centre, and right of the board. At each location, there was a low camera station (i.e. a tripod set at a height of 50cm), and a high camera station (i.e. a tripod set at a height of 180cm). At each camera station, landscape and portrait orientation photos were taken (see Figure 5.2). The origin of the coordinate system was chosen as the bottom left corner of the target board. Also, the sets of three orthogonal lines at each exposure station represent the orientation of the image coordinate system as defined by the  $\omega$ ,  $\phi$ , and  $\kappa$  angles, i.e. the camera x, y, and z axes.

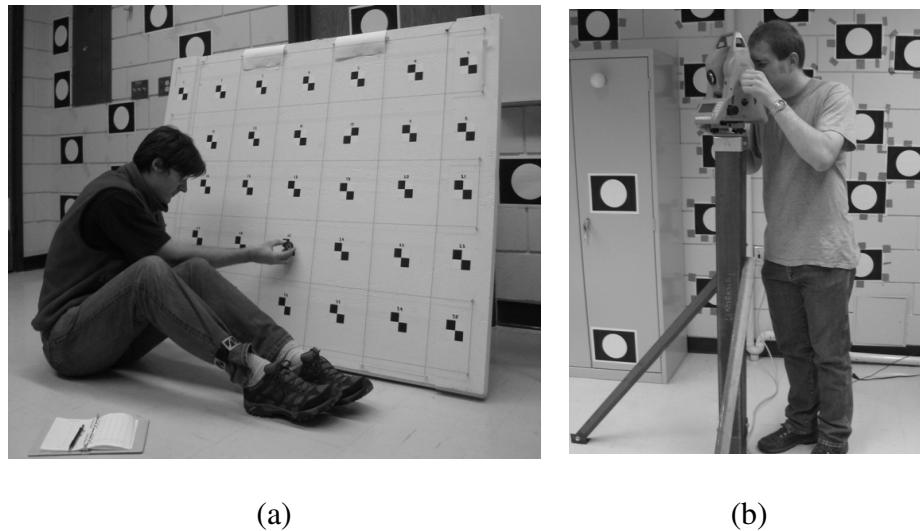


**Figure 5.1 Observing of the targets on the portable calibration board (a) with a high precision total station (b)**

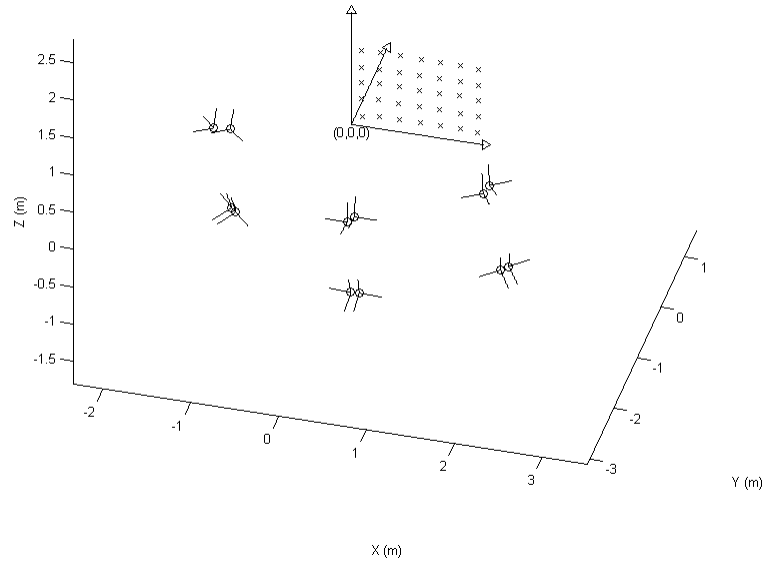


**Figure 5.2 Camera calibration setup: camera stations (circles) and board targets (crosses)**

Source: Datchev *et al.* (2010)

### 5.1.3 Test on the choice for a distortion model

The first test that was performed was to verify whether it is necessary to solve for all the lens distortion parameters, or to just use the first radial lens distortion coefficient (i.e.  $k_1$ ) in the bundle adjustment with self-calibration as shown in equation (5.1).

$$\begin{aligned} \Delta x_p &= k_1 \cdot (r^2 - r_0^2) \cdot x' + k_2 \cdot (r^4 - r_0^4) \cdot x' + p_1 \cdot (r^2 + 2 \cdot (x')^2) + 2 \cdot p_2 \cdot x' \cdot y' - a_1 \cdot x' + a_2 \cdot y' \\ \Delta y_p &= k_1 \cdot (r^2 - r_0^2) \cdot y' + k_2 \cdot (r^4 - r_0^4) \cdot y' + p_2 \cdot (r^2 + 2 \cdot (y')^2) + 2 \cdot p_1 \cdot x' \cdot y' + a_1 \cdot x' - a_2 \cdot y' \end{aligned} \quad (5.1)$$

where as explained in Chapter Three:

$k_1$  and  $k_2$  are the radial lens distortion parameters,

$p_1$  and  $p_2$  are the decentering lens distortion parameters,

$a_1$  and  $a_2$  are the affine deformation parameters,

$r$  is the radial distance,  $r^2 = (x')^2 + (y')^2$ , and  $x' = x_p - x_{pp}$ , and  $y' = y_p - y_{pp}$ , and

$r_0$  is the radial distance with zero radial lens distortion (other than the principal point).

The adjustments were run by fixing six coordinates (e.g. the X, Y, Z for one, the Y, Z for another, and the Y for a third point), and using the distances measured with the tape as control. The standard deviation used for all the distances was  $\pm 1$  mm. The adequacy of lens distortion models used in bundle adjustment with self-calibration procedures for this test was evaluated in three ways:

- by checking the a-posteriori variance factors for the bundle adjustments (i.e. the overall precision values) (see Table 5.1),
- by estimating the similarity between the bundles of light rays defined by the different IOP sets (see Table 5.1), and
- by checking the reconstruction accuracy in object space (i.e. performing a check point analysis) (see Table 5.2).

**Table 5.1 A-posteriori variance factors and RMSE of the bundle similarity in the calibration results for using all six distortion parameters against using only  $k_1$**

<b>Datum definition (and distortion model)</b>	$\hat{\sigma}_0^2$ ( $\mu\text{m}$ )	<b>ROT RMSE (<math>\mu\text{m}</math>)</b>
<b>Distance constraints (all six parameters)</b>	$(0.7)^2$	<b>1.0</b>
<b>Distance constraints (only <math>k_1</math>)</b>	$(0.9)^2$	

**Table 5.2 RMSE between photogrammetric reconstruction and surveying measurements for calibration results when using all six distortion parameters against using only  $k_1$ ; all units are mm**

<b>Datum definition (and distortion model)</b>	<b>Mean <math>\Delta X</math> <math>\pm \sigma \Delta X</math></b>	<b>Mean <math>\Delta Y</math> <math>\pm \sigma \Delta Y</math></b>	<b>Mean <math>\Delta Z</math> <math>\pm \sigma \Delta Z</math></b>	<b>RMS X</b>	<b>RMS Y</b>	<b>RMS Z</b>	<b>Total RMSE</b>
<b>Distance constraints (all six parameters)</b>	0.00 $\pm 0.09$	0.00 $\pm 0.10$	0.00 $\pm 0.05$	0.09	0.10	0.05	<b>0.14</b>
<b>Distance constraints (only <math>k_1</math>)</b>	0.00 $\pm 0.11$	0.00 $\pm 0.12$	0.00 $\pm 0.06$	0.11	0.11	0.06	<b>0.17</b>

Note that the bundle similarity method used here was the rotation one (i.e. ROT). The ROT method was also used to investigate the equivalency of IOP sets resulting from different camera calibration configurations in the rest of the experiments. The ROT bundle similarity technique was necessary, because the comparison between any two sets of IOPs was not undertaken directly. That is, as explained in Chapter Three, the comparison was not accomplished by simply contrasting the estimated values for the individual calibration parameters, because the parameters were correlated. Rather – a grid simulation was used to compare a bundle of light rays defined by the first set of calibration parameters with a bundle of light rays defined by the second set (Habib *et al.*, 2005).

So if the square root of the a-posteriori variance factor for the bundle adjustment using all six distortion parameters was compared against the bundle adjustment using

only the  $k_1$  parameter, it could be noticed that the difference was in the vicinity of  $0.2\mu\text{m}$  (see the first two data columns in Table 5.1). This value was much less than the expected image coordinate measurement accuracy of half a pixel size (i.e.  $\frac{1}{2}$  of  $5.7\mu\text{m}$ ), so the difference could be considered insignificant. Also, the calibration results for the two types of distortion models were regarded as equivalent, because the RMS value between the bundle of light rays defined with all six distortion parameters and the one defined with only  $k_1$  was also under half a pixel size (see the last column in Table 5.1). In addition, the object space reconstructions for the two distortion models only demonstrated differences at a level of less than  $0.1\text{mm}$ , i.e. less than what could be trustfully measured with the total station (i.e.  $1\text{mm} \pm 1\text{ppm}$ ) (see Table 5.2). Since solving for all six distortion parameters did not seem to be crucial, the rest of the experiments involved only solving for  $k_1$ .

#### ***5.1.4 Test on the choice for image space observations***

The second test was to perform a bundle adjustment with self-calibration using only points, and points and linear features as observations in image space. Previous research had shown that including linear features as observations improved the standard deviations for the estimated IOPs (Habib and Morgan, 2005). The differences in the IOP results between the two adjustments for this experiment were summarized in Table 5.3. It could be noticed that the results were quite similar. In fact, the ROT RMSE between the bundles of light rays for both calibration results was  $1.6\mu\text{m}$  (i.e. less than half a pixel size), which deemed them equivalent. However, the IOPs for the solution with linear features do have better standard deviations. Also, so do the EOPs for the same solution. Most likely, the reason for this was that, because more observations were used in the least

squares adjustment, the redundancy was much higher. This test supported the finding previously published.

**Table 5.3 IOP differences for using tie points only against using tie points and linear features**

Image space observations	$x_P \pm \sigma_{x_P}$ ( $\mu\text{m}$ )	$y_P \pm \sigma_{y_P}$ ( $\mu\text{m}$ )	$c$ (mm) $\pm \sigma_c$ ( $\mu\text{m}$ )	$k_1 \pm \sigma_{k_1}$ ( $\text{mm}^{-2}$ )	ROT RMSE ( $\mu\text{m}$ )
Distance constraints	-20.7 $\pm 4.4$	-191.5 $\pm 4.6$	34.920 $\pm 4.8$	-1.65e-5 $\pm 1.18\text{e-}6$	<b>1.6</b>
Distance constraints (with linear features)	-21.6 $\pm 1.6$	-188.0 $\pm 1.8$	34.910 $\pm 2.1$	-1.68e-5 $\pm 1.78\text{e-}7$	

In addition, Table 5.4 lists the RMS values between the two photogrammetric reconstructions (using distance constraints without or with linear features) and the total station survey. It is worth mentioning that the quality of the 3D reconstruction for the board targets was equivalent.

**Table 5.4 RMSE between photogrammetric reconstruction and surveying measurements for calibration results when using points only against using points and linear features as observations; all units are mm**

Image space observations	Mean $\Delta X \pm \sigma$ $\Delta X$	Mean $\Delta Y \pm \sigma$ $\Delta Y$	Mean $\Delta Z \pm \sigma$ $\Delta Z$	RMS X	RMS Y	RMS Z	Total RMSE
Distance constraints (w/out linear features)	0.00 $\pm 0.12$	0.00 $\pm 0.12$	0.00 $\pm 0.06$	0.12	0.12	0.06	<b>0.17</b>
Distance constraints (w/ linear features)	0.00 $\pm 0.11$	0.00 $\pm 0.12$	0.00 $\pm 0.06$	0.11	0.11	0.06	<b>0.17</b>

### 5.1.5 Test on the choice for datum definition

The third test was to perform a bundle adjustment with self-calibration using control points and using distance constraints in order to define the object coordinate datum. In the cases when the adjustment was run with the surveyed points as the chosen control, the standard deviation used for each X, Y, Z coordinate was  $\pm 0.1\text{mm}$ , which came from the output of the network adjustment. The resulted IOP parameters for this experiment are summarized in Table 5.5.

**Table 5.5 IOP differences for using control points against using distance constraints**

Datum definition (and observations)	$x_p \pm \sigma_{x_p}$ ( $\mu\text{m}$ )	$y_p \pm \sigma_{y_p}$ ( $\mu\text{m}$ )	$c$ (mm) $\pm \sigma_c$ ( $\mu\text{m}$ )	$k_1 \pm \sigma_{k_1}$ ( $\text{mm}^{-2}$ )	ROT RMSE ( $\mu\text{m}$ )
<b>Control points only</b>	-22.0 $\pm 4.0$	-177.6 $\pm 4.4$	34.902 $\pm 4.8$	-1.70e-5 $\pm 6.45\text{e-}7$	<b>2.8</b>
<b>Distance constraints</b>	-20.7 $\pm 4.4$	-191.5 $\pm 4.6$	34.920 $\pm 4.8$	-1.65e-5 $\pm 1.18\text{e-}6$	
<b>Control points (with linear features)</b>	-21.4 $\pm 1.6$	-186.5 $\pm 1.7$	34.908 $\pm 2.1$	-1.68e-5 $\pm 1.75\text{e-}7$	<b>0.3</b>
<b>Distance constraints (with linear features)</b>	-21.6 $\pm 1.6$	-188.0 $\pm 1.8$	34.910 $\pm 2.1$	-1.68e-5 $\pm 1.78\text{e-}7$	

From the first two rows of the table, it is noticeable that there were some differences in the results, especially for the estimates of  $y_p$  and the principal distance,  $c$ . However, the ROT RMSE between the bundles of light rays for these two sets of IOPs was  $2.8\mu\text{m}$ , which was only half a pixel. Moreover, if linear features were added as observations in the image space (see last two rows of the table), the results from the two adjustments became almost identical, with a ROT RMSE of  $0.3\mu\text{m}$ . That is, if only points were used

as image space observations, the solution seemed to be sensitive to the way the datum was defined, while if points and linear features were used as image space observations, the solution was more robust against the datum definition procedure.

### ***5.1.6 Camera calibration findings***

In summary, there were three findings for the camera calibration experiments. The first finding was that it was not necessary to solve for all the six lens distortion parameters for the implemented camera, i.e. estimating only  $k_1$  yielded an adequate set of IOPs – the bundle adjustment had sub-pixel level precision in image space, and sub-millimetre accuracy in object space. The second finding (or rather – confirmation) was that adding linear features to the calibration procedure did not increase the accuracy in object space, but seemed to improve the precision of the estimated IOPs (due to increased redundancy). The last finding was that whether control points or distance constraints were used to define the datum, the output IOP sets were equivalent. This was especially true if linear features were used as observations, i.e. they seemed to improve the robustness of the solution against the datum definition procedure. Thus, the most practical way to do the calibration for the rest of the cameras as far as choices for a distortion model, image space observations and datum definition, was to solve only for  $k_1$  as opposed to all the lens distortion parameters, use linear features in addition to points, and use distance constraints as opposed to control points, respectively.

## **5.2 Camera stability analysis**

In order to assess whether the cameras were stable or not, every camera had to be calibrated again (see Table 5.6). Before the second calibration dataset was collected for

each camera, the lenses were removed and then reattached in order to simulate the typical use of DSLRs. The results from the two calibration sets were then compared by using the previously described ROT bundle similarity method, in order to verify that the IOPs for the cameras did not change significantly. The cameras were deemed stable, because the overall RMS error between the reconstructed light ray bundles varied from 1 to  $4.5\mu\text{m}$ , which was below the size of one pixel (see Table 5.7).

**Table 5.6 Example of two sets of camera calibration results for the same camera**

Dataset	$x_P \pm \sigma_{x_P}$ ( $\mu\text{m}$ )	$y_P \pm \sigma_{y_P}$ ( $\mu\text{m}$ )	$c$ (mm) $\pm \sigma_c$ ( $\mu\text{m}$ )	$k_1 \pm \sigma_{k_1}$ ( $\text{mm}^{-2}$ )
Set 1 April 17, 2009	29.9 $\pm 1.6$	32.5 $\pm 1.9$	34.589 $\pm 2.2$	$-2.09\text{e-}5$ $\pm 1.77\text{e-}7$
Set 2 April 22, 2009	34.3 $\pm 1.5$	42.0 $\pm 1.7$	34.603 $\pm 2.0$	$-2.18\text{e-}5$ $\pm 1.76\text{e-}7$

**Table 5.7 Stability results for the two calibration sets for all the cameras**

Camera ID	1	2	3	4	5	6	7
ROT RMSE ( $\mu\text{m}$ )	3.11	3.35	1.65	2.36	0.96	2.11	4.51

### 5.3 Sensor arm setup and exterior orientation parameters determination

Once the camera calibration and the stability analysis were completed, the cameras were ready to be positioned for image acquisition. The seven DSLRs were rigidly mounted to a wooden frame (see Figure 5.3). The camera positions were evenly spaced, and the baseline distance between neighbouring exposure stations was approximately 0.4m. In addition, the cameras were accompanied by a short throw projector. The projector of choice was the single-chip digital light processing (DLP)

BenQ MP522 ST, which had an extended graphics array (XGA) with a resolution of 1024 pixels x 768 pixels. The cameras together with the projector represented one sensor arm.

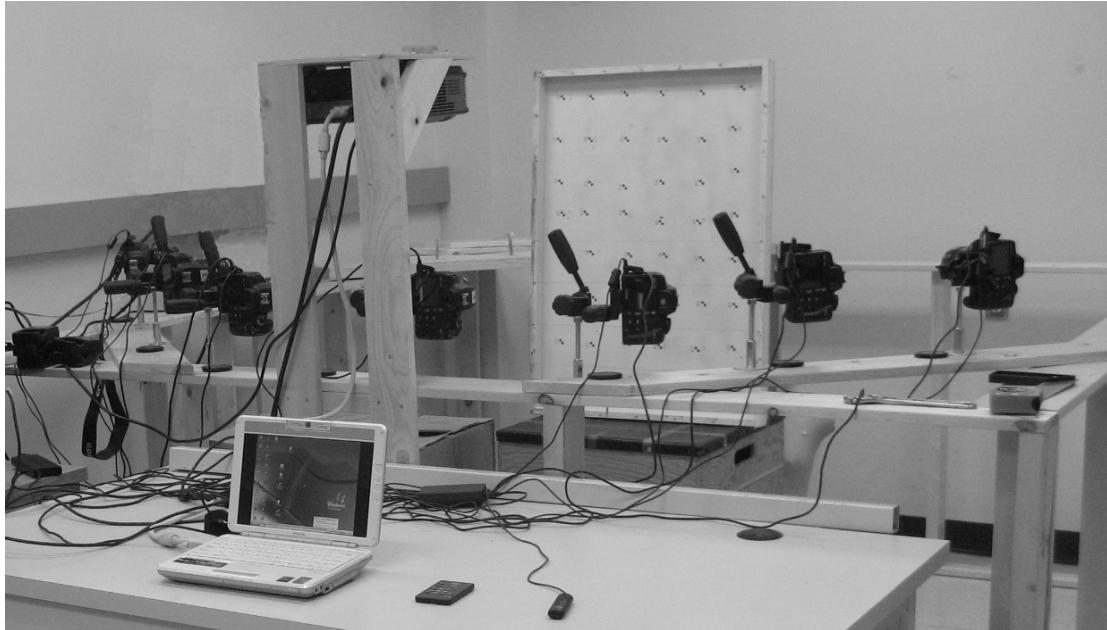


**Figure 5.3** Sensor arm setup showing all the cameras pointed towards a target board

The next step in the system calibration was to determine the EOPs for the camera stations. This was achieved through a bundle adjustment procedure using a target board (similar to the one used for the camera calibration), where the distances between some of the points had been previously measured. The target board had 48 targets, and after it was placed approximately 1.2m away from the cameras (see Figure 5.3), one photograph was collected from each camera. The bundle adjustment had 664 observations and 249 unknowns, and the solution converged in six iterations. The a-posteriori standard deviation was  $2.2\mu\text{m}$ , which was quite acceptable, because it was under half pixel size. The image coordinate residuals ranged from  $-6.9\mu\text{m}$  to  $+6.7\mu\text{m}$  with a mean of zero and a standard deviation (i.e.  $1\cdot\sigma$ ) of  $\pm 1.8\mu\text{m}$  for x, and  $\pm 1.9\mu\text{m}$  for y (see Figure 5.4).

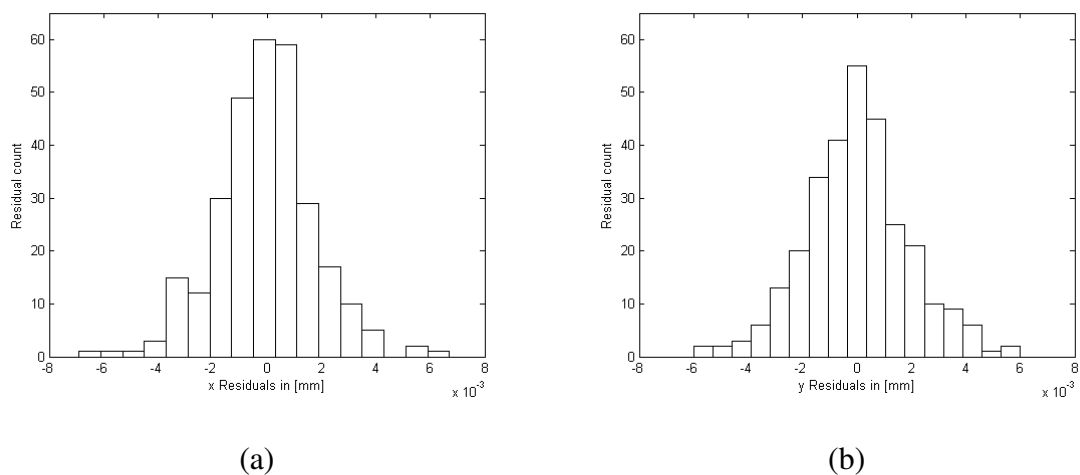


**Figure 5.4 Histogram plots showing image coordinate residuals in x (a), and y (b) for the bundle adjustment to establish the EOPs of the camera exposure stations**

The results for the EOP determination for the seven exposure stations are visually displayed in Figure 5.5. The origin of the coordinate system was chosen as the bottom left corner of the target board. Also, the sets of three orthogonal lines at each exposure station represent the orientation of the image coordinate system as defined by the  $\omega$ ,  $\phi$ , and  $\kappa$  angles, i.e. the x, y, and z axes for each camera.

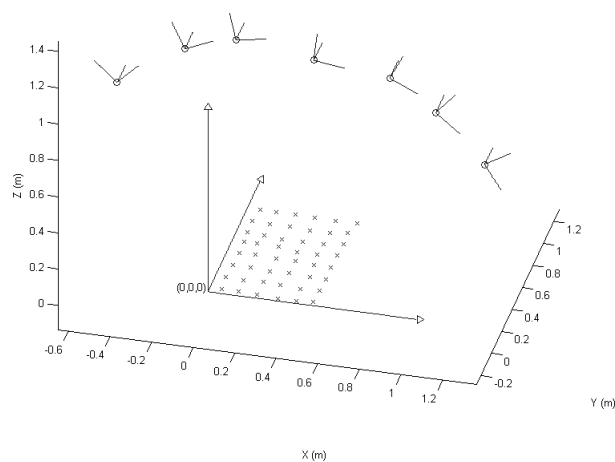


**Figure 5.5 EOP determination: the camera positions shown with circles and the targets on the board with crosses**

#### 5.4 Flat metal plate reconstruction

The first surface reconstruction experiment was performed on a white flat metal plate with dimensions 50cm x 50cm as seen in Figure 5.6a and Figure 5.6b. The purpose of this experiment was to verify that the system was fit to perform high precision reconstructions. Other than biomedical imaging, this could be useful for industrial quality control and infrastructure monitoring (e.g. beams under different loading conditions). The test was done in two independent sessions one month apart. The plate was placed 1.1m away from the exposure stations of the constructed sensor arm. The cameras were synchronized with a remote control, and the images for each of the seven cameras were taken simultaneously. The total number of reconstructed points was 29,590 for the first session, and 28,340 for the second session (see Figure 5.6c). This amounted to an average point density on the order of 12 points/cm<sup>2</sup>. A mathematical model for a plane was fitted to both datasets. The normal distances to the plane ranged from -1.60mm to +1.58mm for the first dataset, and from -1.53 to +1.53mm for the second dataset (see Figure 5.7). The average normal distances were zero millimetres in both cases, and the respective standard deviations (i.e.  $1 \cdot \sigma$ ) were  $\pm 0.48$ mm and  $\pm 0.46$ mm. It is important to note that these standard deviations do not represent the system noise, but the deviation between the reconstructed and the fitted plane. It could be noticed that the histogram shown in Figure 5.7a is skewed, i.e. the normal distances were not normally distributed. This was due to the fact that the metal plate was not perfectly flat as seen in Figure 5.7b. This means that if a more suitable model (e.g. 3D surface as opposed to a 2D plane) was fitted to the current data or a flatter surface was reconstructed, the standard deviations of the normal

distances would be even less than the current values. Based on the range of the noise in Figure 5.7b, the surface reconstruction accuracy can be estimated to be less than 1mm.

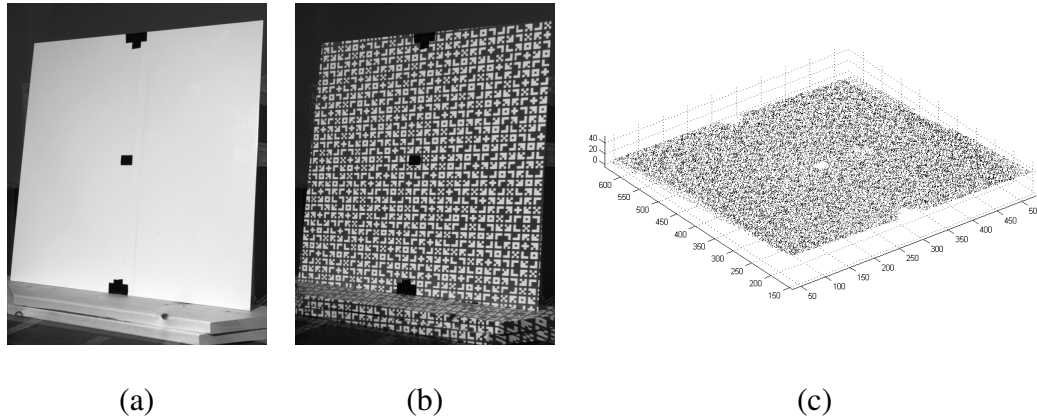
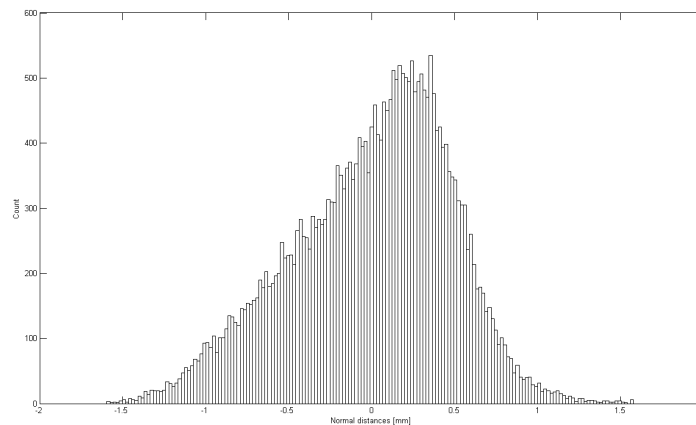
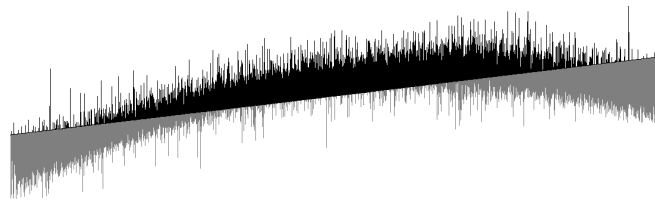


**Figure 5.6** Example photo of the flat metal plate used in the experiment (a); the same plate imaged with a pattern projection (b); final 3D reconstruction of the flat metal plate (c)

The execution for the reconstruction of the plate surface model took over three hours in both experiments. The bulk of the processing time, i.e. 30 minutes per stereo pair on average, was spent on the hierarchical image matching. Speeding up this process would be the focus of future work.



(a)



(b)

**Figure 5.7 Histogram of the normal distances for the plane fitting of the flat metal plate reconstruction (a); Z-X plot of the normal distances above (black) and below (gray) the fitted plane (b)**

### 5.5 Human face reconstruction

The next experiment was done on human subjects. Its purpose was to verify that the system could be used for facial reconstruction and related applications (e.g. cosmetic surgery and facial asymmetry measurements). The experiment was similar to the one that had been done by (Cheng and Habib, 2007), except they had used only two cameras and a simple grid pattern, and the conjugate point identification and collection had been done manually. The faces of two subjects (see Figure 5.8a and Figure 5.8b) were reconstructed twice while varying the size of the projected patterns (as varying the size of the projected pattern was one of the experiment objectives). Just as with the metal plate experiment, the subjects were asked to sit approximately 1.1m away from the sensor arm cameras, and the shutter release of the cameras was controlled with a remote trigger. The face reconstruction of the first subject had 2710 points after using a large (coarse) pattern, and 5770 after using a small (fine) pattern (see Figure 5.8c). Similarly, the face reconstruction of the second subject constituted of 2360 and 4950 points after using a large (coarse), and a small (fine) pattern (see Figure 5.8d), respectfully.

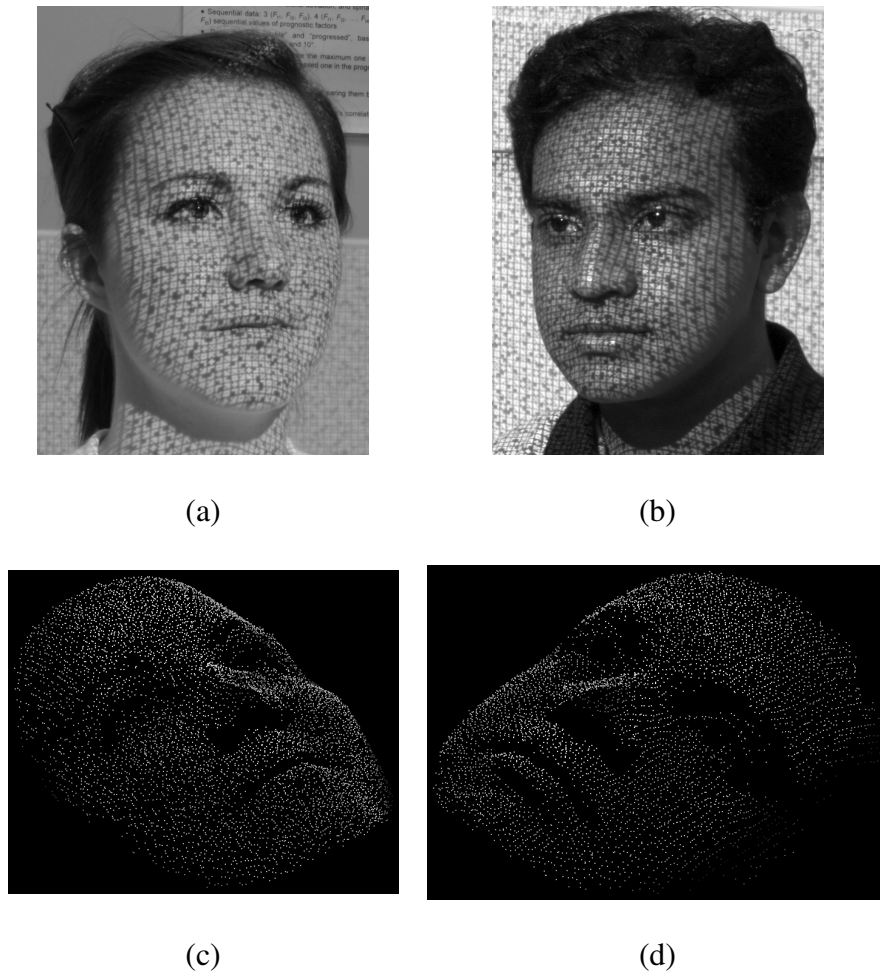
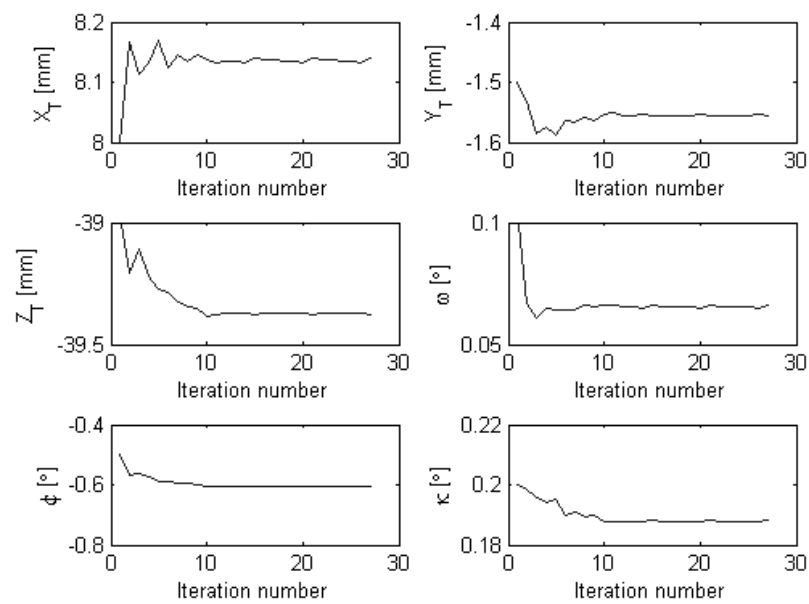


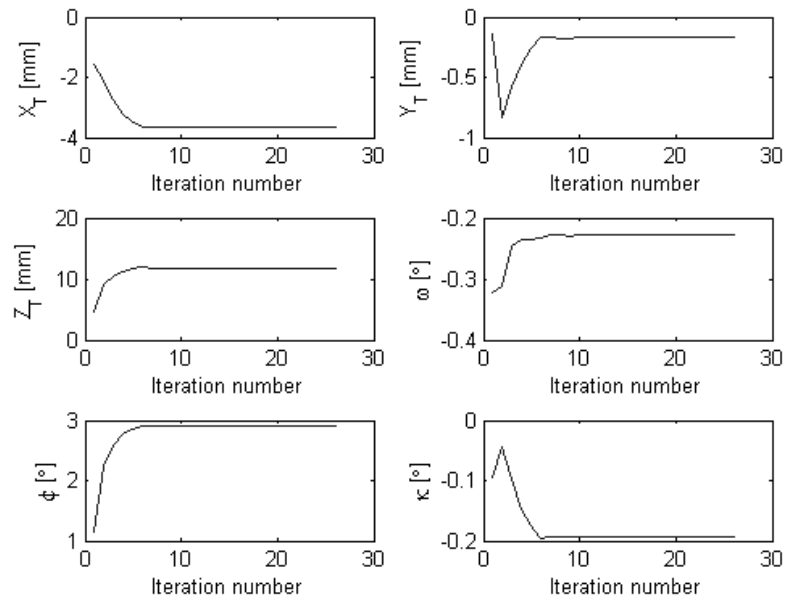
**Figure 5.8** The first (a) and second (b) subjects, and the irregular point clouds of their respectful face reconstructions (c), and (d) using the small (fine) pattern

It can be noted that there were approximately 15% more points in the face reconstruction of the first subject. This is most likely because the face of the first subject had smoother features and a fair complexion, while the second subject had more pronounced facial characteristics, and at the same time – a darker skin tone. Using the surface registration technique explained in Chapter Four, the two reconstructions for each subject were registered by keeping the large (coarse) pattern irregular point cloud as points, and converting the smaller (finer) pattern irregular point cloud to triangular irregular

networks (TINs). The datasets for the face of the first subject registered with an average normal distance of 0.38mm, where 93.5% of the points found matching TIN patches, and the datasets for the face of the second subject registered with an average normal distance of 0.34mm, where 93.3% of the points found matching TIN patches (see plots of the convergence of the transformation parameters in Figure 5.9). Note that the convergence of the transformation parameters for the second subject (Figure 5.9b) was better than the one for the first subject (Figure 5.9a). This could be credited to the more pronounced facial features of the second subject.



(a)



(b)

**Figure 5.9 Iterative solution for the transformation parameters for the facial reconstruction of the first (a) and the second (b) subject**

Thus, it could be concluded that other than the fewer number of points for the second subject, the reconstructed 3D models for the two subjects were equally reliable. The execution for the face reconstruction using the small (fine) pattern took over one hour per subject. The bulk of the processing time, i.e. 10 minutes per stereo pair on average, was again spent on the hierarchical image matching. The reason why the execution time for this experiment was less than the one for the metal plate was due to the much smaller area of interest, i.e. the faces of the human subjects did not fill the full format of the collected images.

## **5.6 Artificial torso mannequin reconstruction**

The third and most important application that the system was tested on was a 360° scoliotic torso reconstruction. There were three types of experiments carried out. The first experiment involved a single projector as part of the system setup. The second experiment involved a dual projector setup, and the effect of the pattern overlap from the two projectors on the surface reconstruction was assessed. In the first two experiments only the coplanarity constraint method was used for the surface registration, so that the results could be compared to the ones from previous work. Thus, the third experiment was to specifically compare the coplanarity constraint and the modified weight matrix methods for the surface registration. The following subsections show detailed results for these experiments.

### ***5.6.1 Single projector torso reconstruction***

The two previously described experiments only required a single sensor arm, because they did not deal with 360° reconstruction. Note that since only seven cameras were available at the time of the experiments, just one out of the four sensor arms for the designed system was implemented. In order to simulate the four necessary sensor arms for reconstructing a human torso as per the design setup in Chapter Three, an artificial scoliotic torso mannequin was used. This way, even though only one sensor arm was available (see Figure 5.10), motion problems were avoided. The approximate dimensions of the mannequin were a height of 60cm, a width of 40cm, and a depth of 25cm. During the data collection, the torso mannequin had to be rotated three times, producing four sets of images – one each for the front, the right side, the back, and the left side (see Figure 5.11). The four sets of images, that were acquired, were used to reconstruct four partial

pieces of the full torso (see Figure 5.12). Since these four partial pieces were theoretically in four different reference frames (due to the fact that the torso was rotated), they had to be registered to a common reference frame as explained in Chapter Four. After all the processing was finished, the final torso model was evaluated both qualitatively and quantitatively. The qualitative evaluation was done by examining the completeness of the reconstruction, and the quantitative one – by first checking the goodness of fit for the surface registration of the four surfaces and second by matching targets on the reconstructed torso model to “ground truth” acquired from the coordinate measuring machine (CMM) FaroArm (FARO Technologies Inc., Lake Mary, Florida – see Figure 5.13). In addition, the results for this experiment (i.e. June 2009) were compared to the results of two previous reconstruction datasets of the same torso mannequin. These previous datasets were acquired and processed in May and September 2008, and their results were published in Chang (2008) and Chang *et al.* (2009). The May and September 2008 experiments were conducted similarly to the ones described in this research work except for a few notable differences. In terms of the data collection, only one camera and a tripod were available at the time, so each sensor arm had to be simulated by manually moving the camera to each of the desired exposure stations. Also, the distance between the exposure stations and the object of interest were much longer, so the object of interest did not fill out the image format. In terms of the surface reconstruction, the hierarchical image matching was not yet implemented.

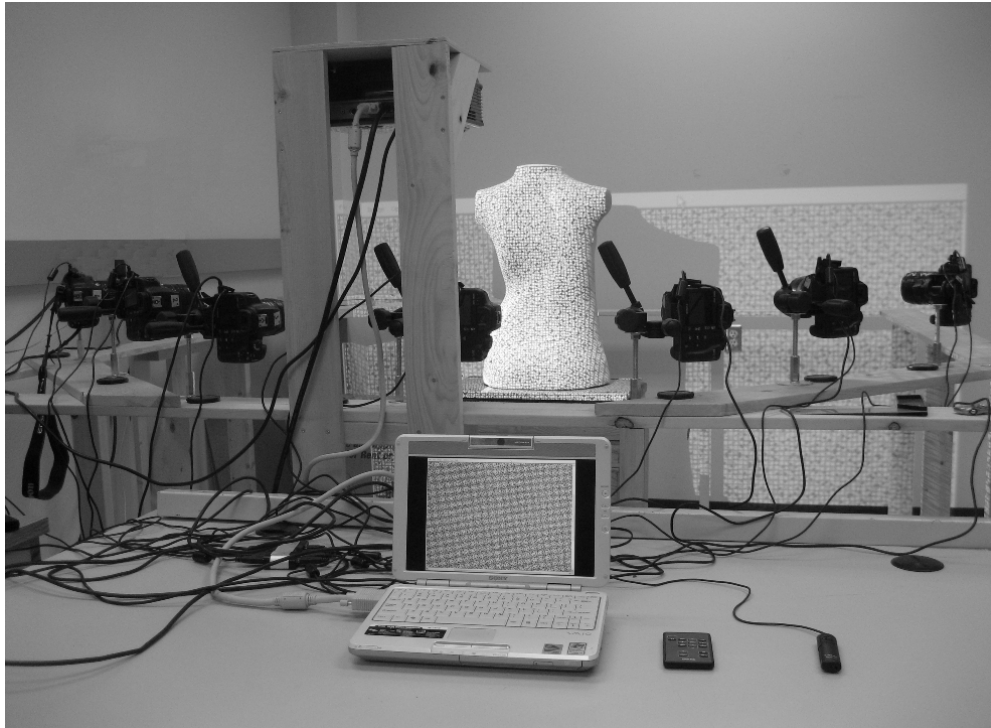


**Figure 5.10** Sensor arm setup showing all the cameras pointed towards the torso mannequin

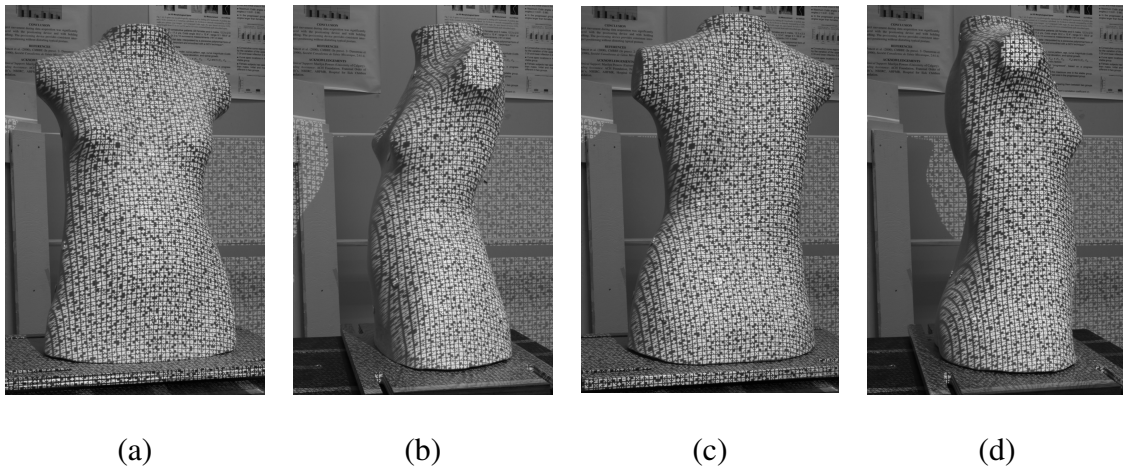


**Figure 5.11** The central images from the sensor arm for the four torso mannequin surfaces – the front/ $S_1$  (a), the right side/ $S_2$  (b), the back/ $S_3$  (c), and the left side/ $S_4$  (d)

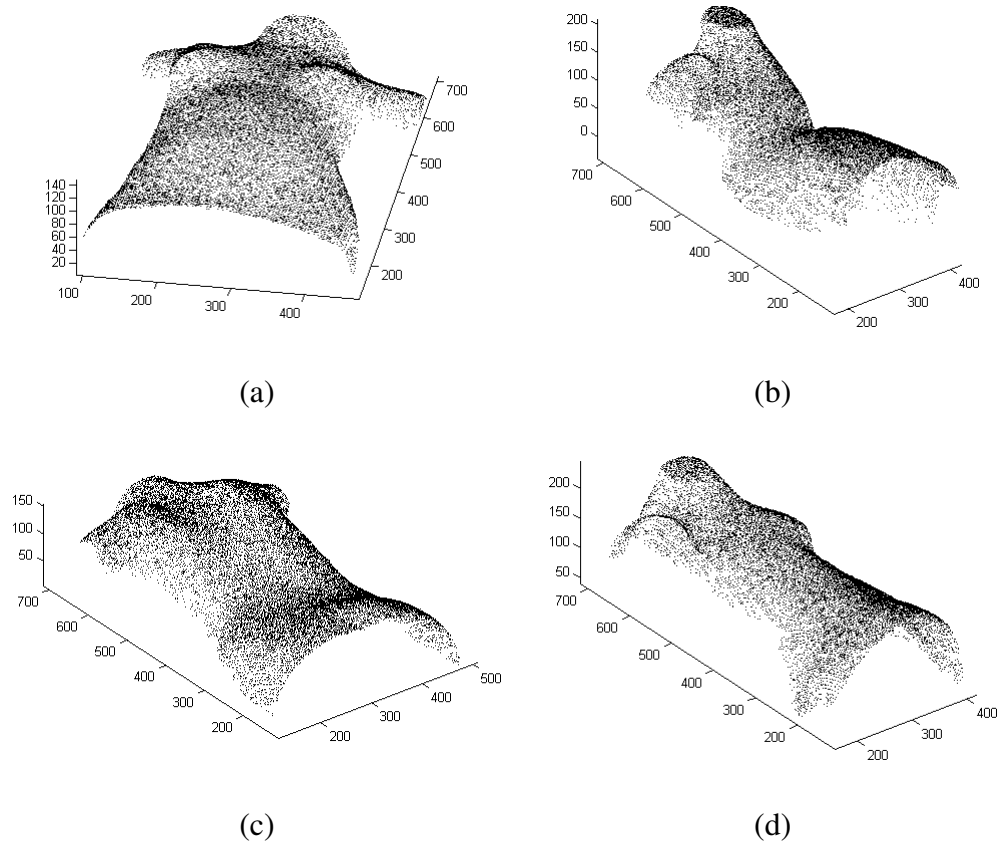


**Figure 5.12** The reconstructed torso front/ $S_1$  (a), right side/ $S_2$  (b), back/ $S_3$  (c), and left side/ $S_4$  (d) surfaces



**Figure 5.13** FaroArm

Source: <http://pss-corp.com/FaroArm.jpg>

In this experiment, the cross section of the reconstructed torso (see Figure 5.14) visually shows that the four partial surfaces were combined well – there were no major gaps or inconsistencies. Also, the cross section point density was high enough to visualize the torso asymmetry, which could be used when reconstructing the scoliotic spine.

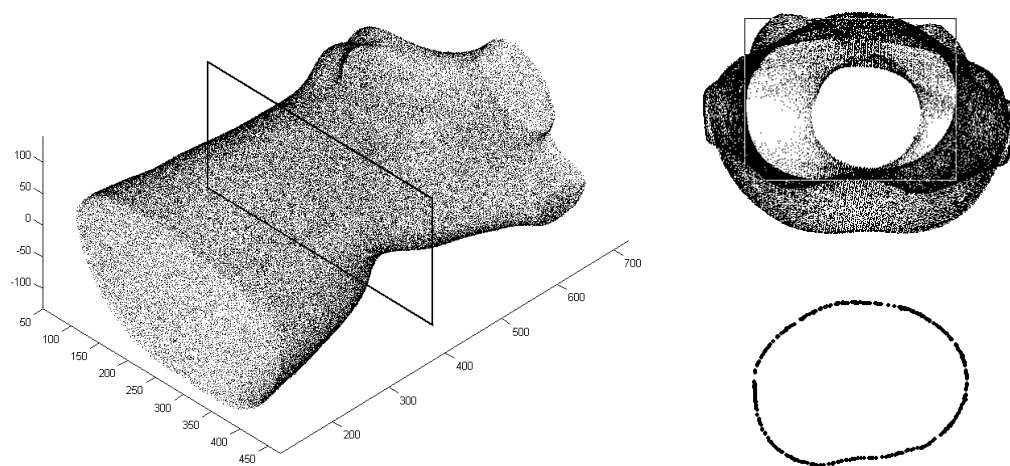


**Figure 5.14 3D model of the entire reconstructed torso mannequin (left), and example cross section profile (right)**

The number of points in the four reconstructed surfaces for this experiment (i.e. June 2009) varied from 14,000 to 20,000. As seen in Table 5.8, this was an improvement compared to the two previous datasets. This improvement was due to that fact that the full image format was used in the current experiment, and also the implemented hierarchical image matching improved the matching reliability. The average normal distances between the matched point-patch pairs in the transformed surfaces were on the order of 0.3mm for both the pairwise and the multiple surface registrations as seen in Table 5.9 and Table 5.10.

**Table 5.8** Number of points in the four reconstructed surfaces for the new dataset compared to the ones published in Chang (2008) and Chang *et al.* (2009)

Dataset	Front $S_1$	Right side $S_2$	Back $S_3$	Left side $S_4$
May 2008	15,240	10,160	15,260	8,600
Sept 2008	11,190	9,040	11,350	6,780
June 2009	<b>18,530</b>	<b>14,810</b>	<b>20,510</b>	<b>14,610</b>

**Table 5.9** Goodness of fit after the pairwise registration for the four reconstructed surfaces in the new dataset compared to the ones published in Chang (2008) and Chang *et al.* (2009); the number of matched point-patch pairs in the overlapping areas is shown in brackets

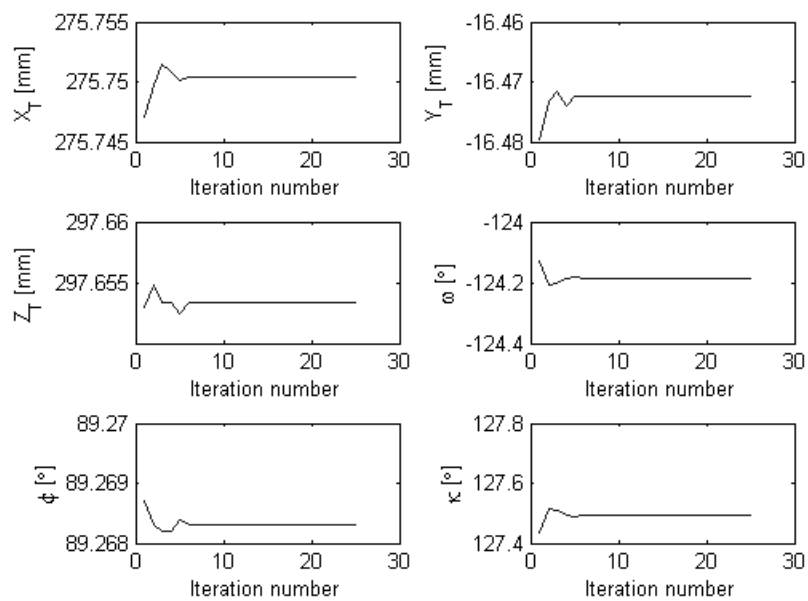
Surface pairs	Average normal distance (mm)		
	May 2008 dataset	Sept 2008 dataset	June 2009 dataset
$S_2$ to $S_1$	0.50 (3,750)	0.70 (3,940)	<b>0.34 (4,850)</b>
$S_3$ to $S_2$	0.51 (4,620)	0.83 (4,000)	<b>0.34 (5,570)</b>
$S_4$ to $S_3$	0.45 (2,000)	0.76 (2,760)	<b>0.32 (5,150)</b>
$S_4$ to $S_1$	0.45 (2,000)	0.84 (2,510)	<b>0.29 (5,260)</b>

**Table 5.10** Goodness of fit after the multiple-surface registration for the four reconstructed surfaces in the new dataset compared to the ones published in Chang (2008) and Chang *et al.* (2009)

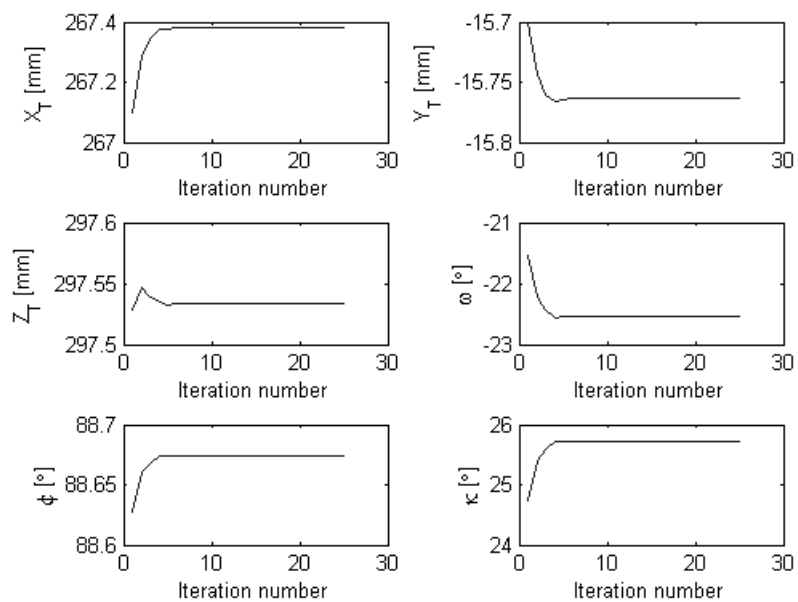
Surface pairs	Average normal distance (mm)		
	May 2008 dataset	Sept 2008 dataset	June 2009 dataset
$S_2$ to $S_1$	0.50	0.70	<b>0.34</b>
$S_3$ to $S_2$	0.58	0.85	<b>0.32</b>
$S_4$ to $S_3$	0.47	0.77	<b>0.32</b>
$S_4$ to $S_1$	0.45	0.85	<b>0.29</b>

As explained at the beginning of this subsection, in both cases the coplanarity constraint method was used in the registration process, because this was the similarity measure implemented for the work published in Chang (2008) and Chang *et al.* (2009). This way the results from the new dataset (i.e. June 2009) were comparable to ones from the previous datasets (i.e. May and September 2008). In this regard, it could be noticed (in Table 5.9 and Table 5.10) that the new dataset had an improved goodness of fit for the four reconstructed surfaces. This could be credited to the much higher number of points in the surface point clouds, causing an increased number of points in the overlapping areas. In addition, Figure 5.15 shows plots of the convergence of the transformation parameters for the four surfaces, and Figure 5.16 shows the overlap areas between them in the pairwise surface registration for the new dataset.

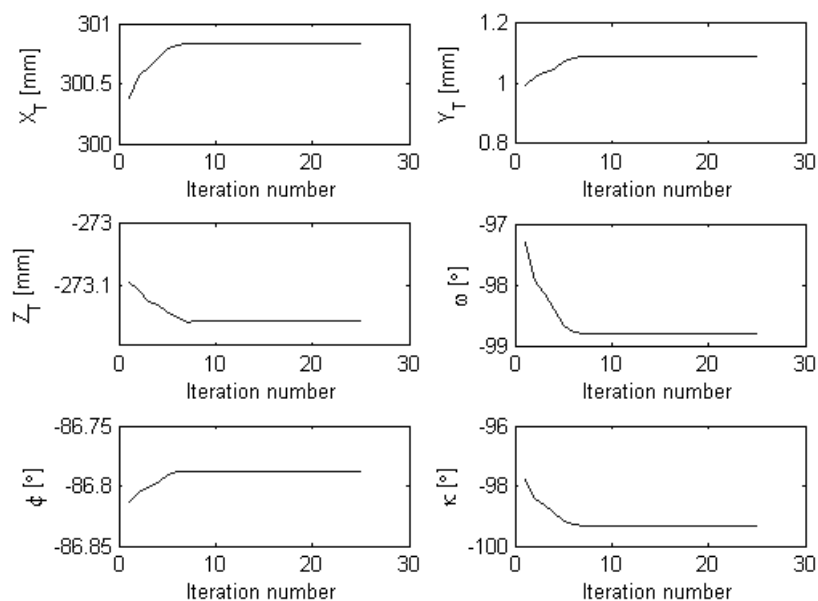
To test the accuracy of the final torso model the centroids of 25 well distributed torso targets (#1 to #16, and #18 to #26) were measured with the FaroArm (25 $\mu$ m measurement accuracy). In addition, using the same robotic coordinate measuring machine, 20 control points were collected on the surface of the targets, and 20 other control points were collected on the surface of the torso around the targets (see Figure 5.17). In this way, there were 41 points defining each of the 25 localized control areas, i.e. one control area for each torso target. The points belonging to these control areas were then registered to the reconstructed torso model using the previously described surface registration technique. The estimated average normal distance was 0.42mm, where 97.8% of the 1025 control points (25 targets x 41 points per target) were matched to the reconstructed torso model (see Figure 5.18).



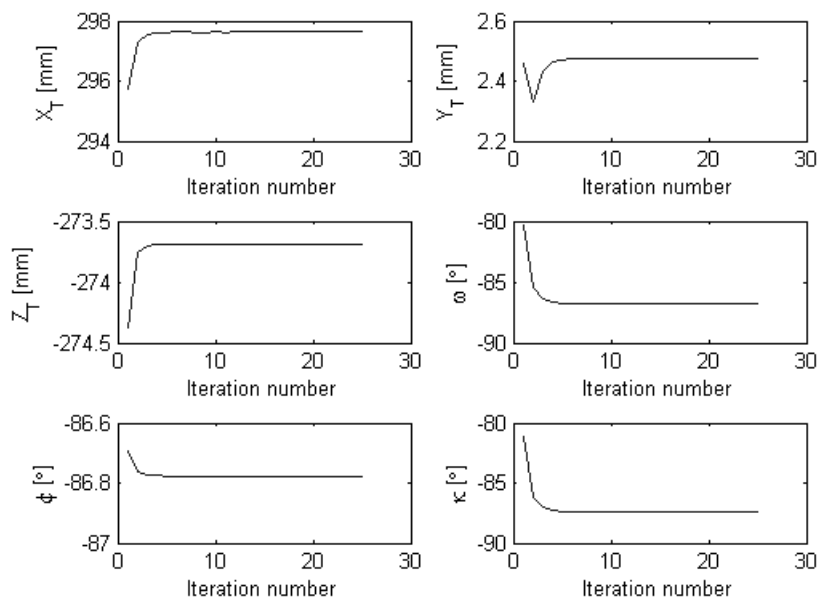
(a)



(b)



(c)



(d)

**Figure 5.15** Iterative solution for the transformation parameters in the pairwise surface registration between  $S_2$  and  $S_1$  (a),  $S_3$  and  $S_2$  (b),  $S_4$  and  $S_3$  (c), and  $S_4$  and  $S_1$  (d) for the new dataset

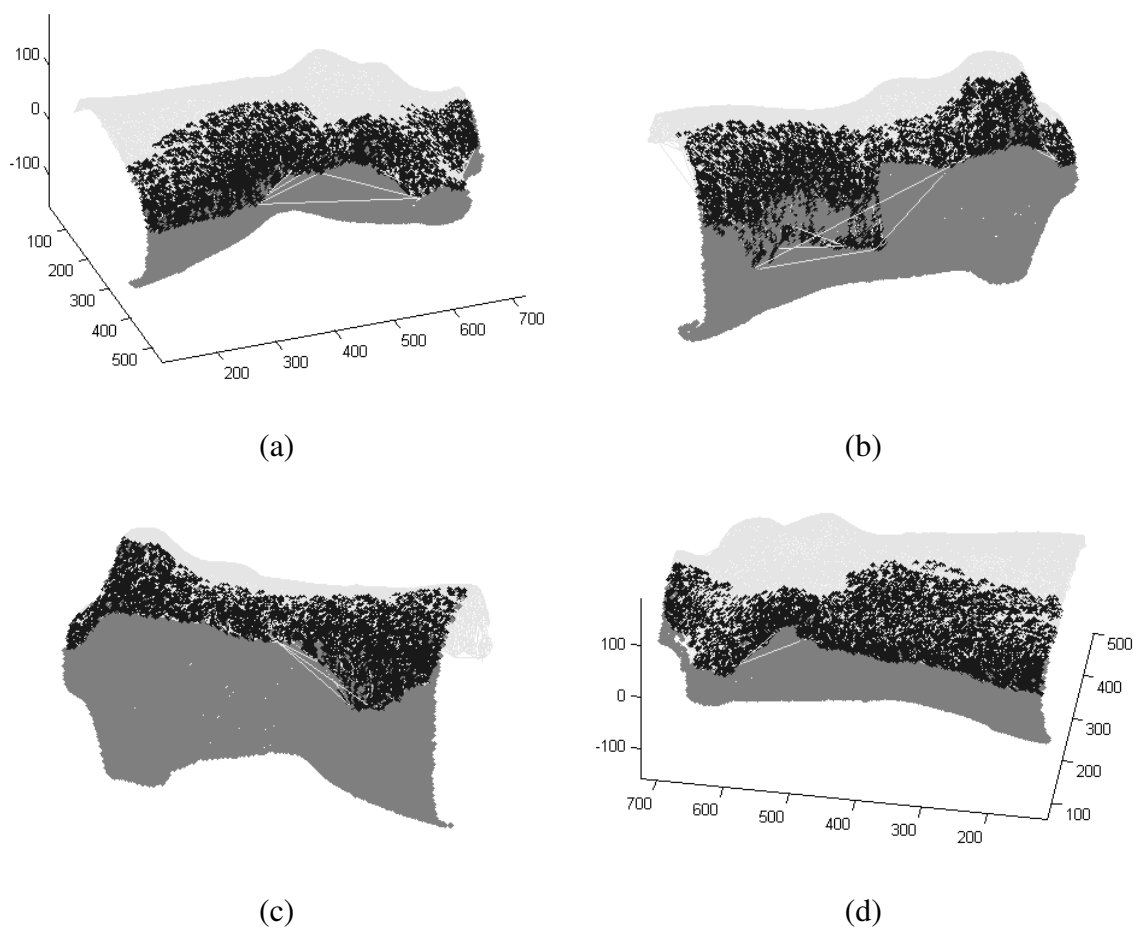


**Figure 5.16** Visual aid for the pairwise surface registration of  $S_2$  and  $S_1$  (a),  $S_3$  and  $S_2$  (b),  $S_4$  and  $S_3$  (c), and  $S_4$  and  $S_1$  (d) for the new dataset (light gray: non-matched area in the TIN surface; black: matched area in the overlap between the point cloud and the TIN surface; dark gray: non-matched area in the point cloud)

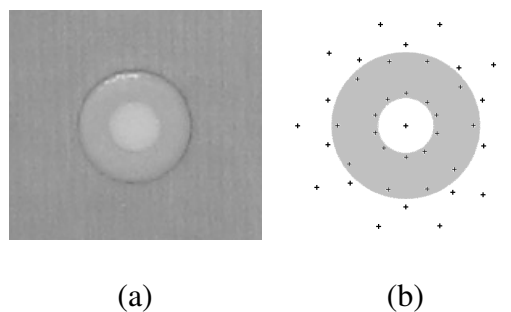


**Figure 5.17** Example of a torso target (a), and the approximate distribution of measured control points (b)

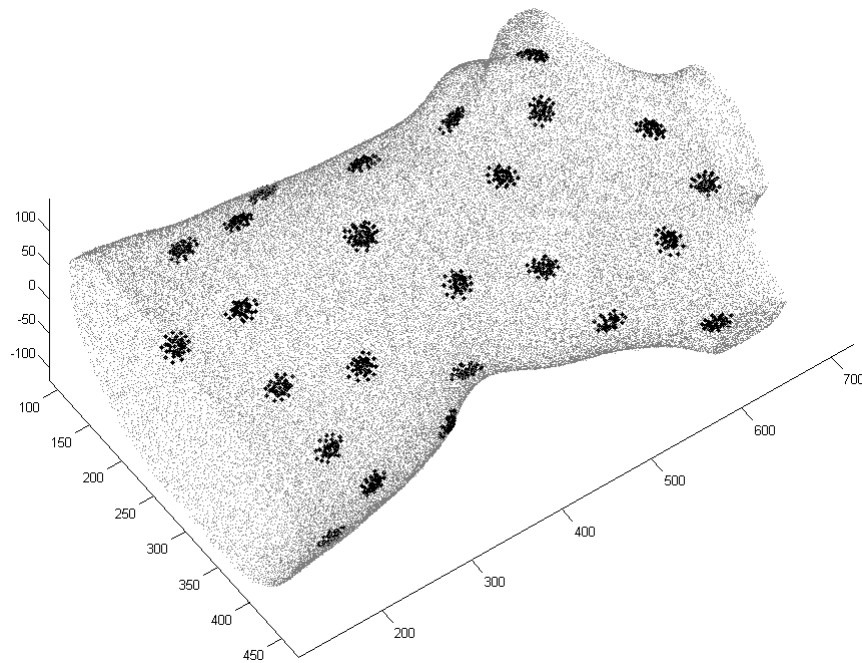


**Figure 5.18 Registration of the FaroArm control points to the fully reconstructed 3D torso model**

Again, this was an improvement compared to the results from the previous datasets, where the average normal distance was 0.52mm for the May 2008 dataset, and 0.58mm for the September 2008 dataset. Also, in the new dataset, one out of the 25 centroid targets did not find a matching patch, and one of them had a normal distance larger than 0.5mm (see Table 5.11). In the previous work, three centroid targets did not find a matching patch in the May 2008 dataset, and two in the September 2008 dataset. Also, in the previous datasets, five from the centroid targets had normal distances of over 1mm (Chang, 2008; Chang et al., 2009). These results are summarized in Table 5.12.

**Table 5.11 Estimated normal distances between the 25 centroid targets and their corresponding patches**

<b>Target ID</b>	<b>Normal distance (mm)</b>	<b>Target ID</b>	<b>Normal distance (mm)</b>
<b>1</b>	0.27	<b>14</b>	0.28
<b>2</b>	0.42	<b>15</b>	0.21
<b>3</b>	0.30	<b>16</b>	0.41
<b>4</b>	0.00		
<b>5</b>	0.25	<b>18</b>	0.36
<b>6</b>	0.21	<b>19</b>	0.27
<b>7</b>	0.37	<b>20</b>	0.26
<b>8</b>	0.58	<b>21</b>	0.15
<b>9</b>	0.36	<b>22</b>	0.31
<b>10</b>	0.03	<b>23</b>	0.37
<b>11</b>	0.02	<b>24</b>	0.06
<b>12</b>	0.10	<b>25</b>	0.25
<b>13</b>	0.15	<b>26</b>	Non-matched

**Table 5.12 Summary of the absolute accuracy evaluation for the new dataset compared to the previous ones published in Chang (2008) and Chang *et al.* (2009)**

<b>Dataset</b>	<b>Average normal distance (mm)</b>	<b>Number of centroid targets with normal distance over 1mm</b>	<b>Number of non-matched centroid targets</b>
<b>May 2008</b>	0.52	5	3
<b>Sept 2008</b>	0.58	5	2
<b>June 2009</b>	<b>0.42</b>	<b>0</b>	<b>1</b>

In addition, Figure 5.19 shows plots for the convergence of the transformation parameters for the registration between the FaroArm control points and the reconstructed torso.

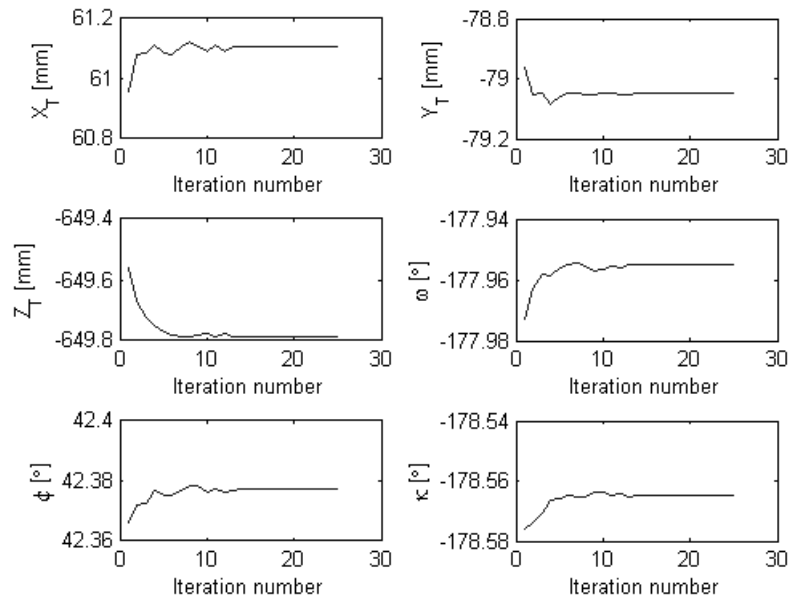


**Figure 5.19 Iterative solution for the transformation parameters in the registration between the FaroArm control points and the fully reconstructed 3D torso model**

In this experiment, the execution time for the reconstruction of a surface model for one sensor arm was two hours on average. The manual part of the processing, i.e. tracing the ROI, took about three minutes per stereo pair or around 15 minutes for each sensor arm. The rest of the surface reconstruction processing was done automatically. The bulk of the processing time, i.e. 15 minutes per stereo pair on average, was spent on the hierarchical image matching.

### **5.6.2 Dual projector torso reconstruction**

The second experiment on the torso reconstruction involved a dual projector setup. So, another DLP BenQ MP522 ST short-throw projector was installed to the side of the previously setup sensor arm (see Figure 5.20), and two datasets were collected and processed in July and October 2009. The purpose of the second projector was to test the effect of the pattern overlap from the two projectors on the quality of the torso

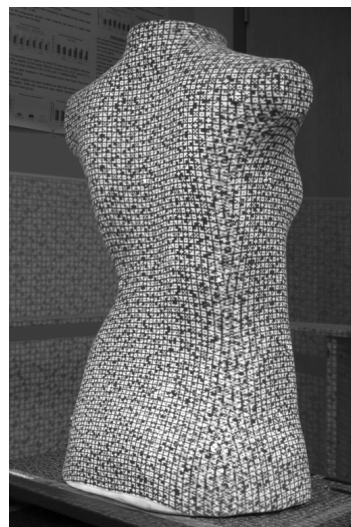
reconstruction. Figure 5.21 shows an example of the presence of this overlap in the collected images.



**Figure 5.20 Dual projector sensor arm setup showing all the cameras pointed towards the torso mannequin**



(a)



(b)

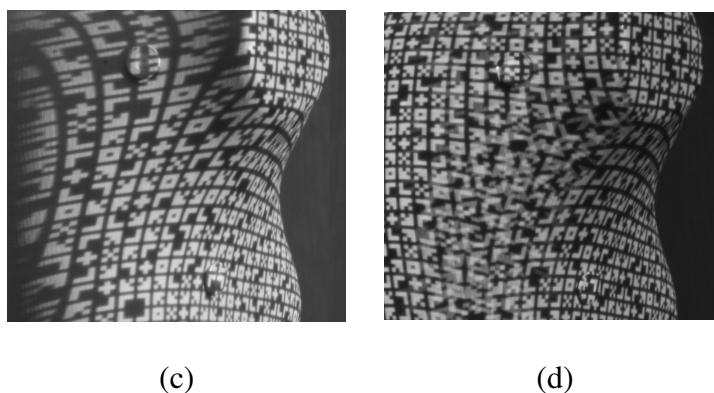


**Figure 5.21 Example images without (a) and with (b) a pattern overlap; zoomed in example view without (c) and with (d) the pattern overlap**

The interference between the patterns projected by the two projectors did not have a negative, but rather a positive effect on the torso reconstruction. Specifically, compared to the single projector dataset there were more points in the reconstructed surfaces in the dual projector datasets (see Table 5.13). Also, there were more points matched in the pattern overlapping areas, which seemed to slightly strengthen the surface registration (see Table 5.14 and Table 5.15).

**Table 5.13 Number of points in the reconstructed surfaces for the datasets with dual projector compared to the one with a single projector**

<b>Dataset</b>	<b>Front S<sub>1</sub></b>	<b>Right side S<sub>2</sub></b>	<b>Back S<sub>3</sub></b>	<b>Left side S<sub>4</sub></b>
<b>Single projector June 2009</b>	18,530	14,810	20,510	14,610
<b>Dual projector July 2009</b>	<b>20,910</b>	<b>17,220</b>	<b>21,870</b>	<b>17,830</b>
<b>Dual projector Oct 2009</b>	<b>20,480</b>	<b>16,910</b>	<b>21,120</b>	<b>17,340</b>

**Table 5.14 Goodness of fit after the pairwise registration for the four reconstructed surfaces in the datasets with dual projector compared to the ones with a single projector; the number of matched point-patch pairs in the overlapping areas is shown in brackets**

Surface pairs	Average normal distance (mm)		
	June 2009 (single projector)	July 2009 (dual projector)	Oct 2009 (dual projector)
S <sub>2</sub> to S <sub>1</sub>	0.34 (4,850)	<b>0.29 (6,700)</b>	<b>0.28 (6,730)</b>
S <sub>3</sub> to S <sub>2</sub>	0.34 (5,570)	<b>0.29 (6,570)</b>	<b>0.30 (6,330)</b>
S <sub>3</sub> to S <sub>4</sub>	0.32 (5,150)	<b>0.29 (6,320)</b>	<b>0.28 (5,890)</b>
S <sub>4</sub> to S <sub>1</sub>	0.29 (5,260)	<b>0.27 (6,540)</b>	<b>0.27 (6,480)</b>

**Table 5.15 Goodness of fit after the multiple-surface registration for the four reconstructed surfaces in the datasets with dual projector compared to the ones with a single projector**

Surface pairs	Average normal distance (mm)		
	June 2009 (single projector)	July 2009 (dual projector)	Oct 2009 (dual projector)
S <sub>2</sub> to S <sub>1</sub>	0.34	<b>0.29</b>	<b>0.28</b>
S <sub>3</sub> to S <sub>2</sub>	0.32	<b>0.28</b>	<b>0.28</b>
S <sub>3</sub> to S <sub>4</sub>	0.32	<b>0.29</b>	<b>0.28</b>
S <sub>4</sub> to S <sub>1</sub>	0.29	<b>0.27</b>	<b>0.28</b>

In terms of absolute accuracy, 98.6% and 98.1% of the 1025 FaroArm control points (25 targets x 41 points per target) found corresponding patches in the July and October 2009 datasets with estimated average normal distances of 0.29mm and 0.32mm, respectively (see Table 5.16). In both cases, there was only one out of the 25 centroid targets with a normal distance of just over 0.5mm (see Table 5.17). Figure 5.22 shows plots for the convergence of the transformation parameters for the registration between the FaroArm

control points and the two reconstructed torso models. In order to check the repeatability, the two torso models were registered to each other and the average normal distance was 0.19mm, where 99.1% of the points from the October 2009 dataset were matched to the patches from the July 2009 dataset. Figure 5.23 shows the plots for the convergence of the transformation parameters for this repeatability test.

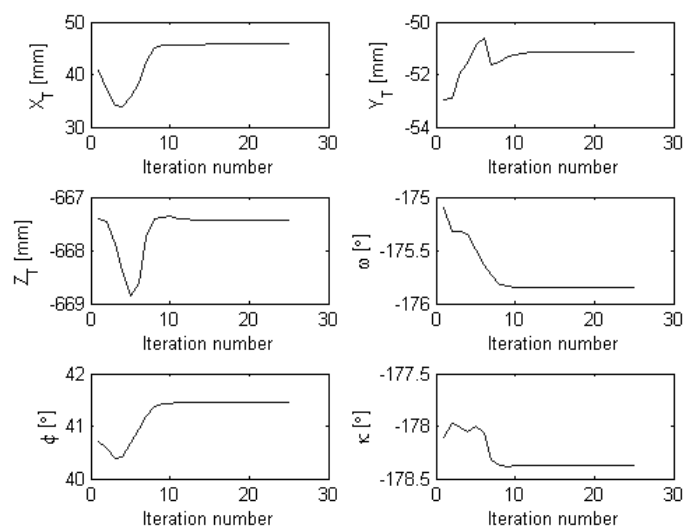
**Table 5.16 Summary of the absolute accuracy evaluation for the dual projector datasets compared to the one with a single projector**

<b>Dataset</b>	<b>Average normal distance (mm)</b>	<b>Number of centroid targets with normal distance over 0.5mm</b>	<b>Percentage of matched control points</b>
<b>June 2009</b>	0.42	1	97.8
<b>July 2009</b>	<b>0.29</b>	<b>1</b>	<b>98.6</b>
<b>Oct 2009</b>	<b>0.32</b>	<b>1</b>	<b>98.1</b>

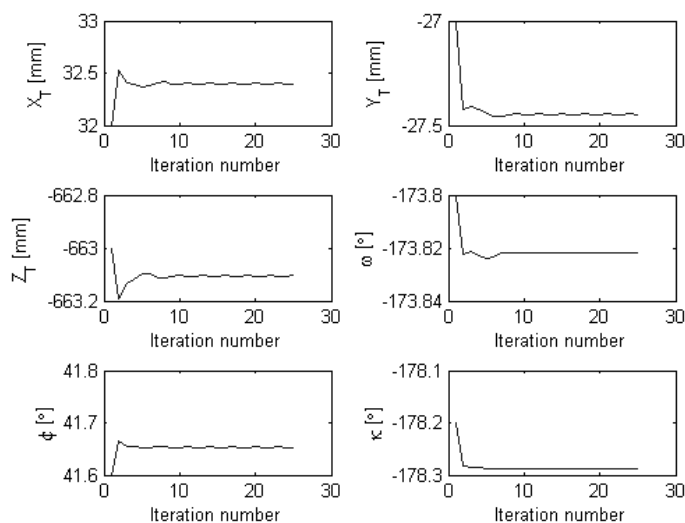
**Table 5.17 Estimated normal distances between the 25 centroid targets and their corresponding patches for the dual projector datasets**

<b>Target ID</b>	<b>Normal distance (mm)</b>		<b>Target ID</b>	<b>Normal distance (mm)</b>	
	July 2009	Oct 2009		July 2009	Oct 2009
<b>1</b>	0.06	0.08	<b>14</b>	0.23	0.06
<b>2</b>	0.16	0.16	<b>15</b>	0.15	0.15
<b>3</b>	0.06	0.40	<b>16</b>	0.10	0.13
<b>4</b>	0.29	0.21			
<b>5</b>	0.14	0.11	<b>18</b>	0.13	0.22
<b>6</b>	0.08	0.27	<b>19</b>	0.20	0.09
<b>7</b>	0.06	0.19	<b>20</b>	0.25	0.04
<b>8</b>	0.28	0.39	<b>21</b>	0.04	0.13
<b>9</b>	0.24	0.24	<b>22</b>	0.28	0.15
<b>10</b>	0.06	0.05	<b>23</b>	0.10	0.55

<b>11</b>	0.46	0.03	<b>24</b>	0.54	0.03
<b>12</b>	0.34	0.23	<b>25</b>	0.01	0.08
<b>13</b>	0.09	0.24	<b>26</b>	0.11	0.16



(a)



(b)

**Figure 5.22 Iterative solution for the transformation parameters in the registration between the FaroArm control points and the fully reconstructed torso models in the July (a) and the October (b) 2009 datasets**

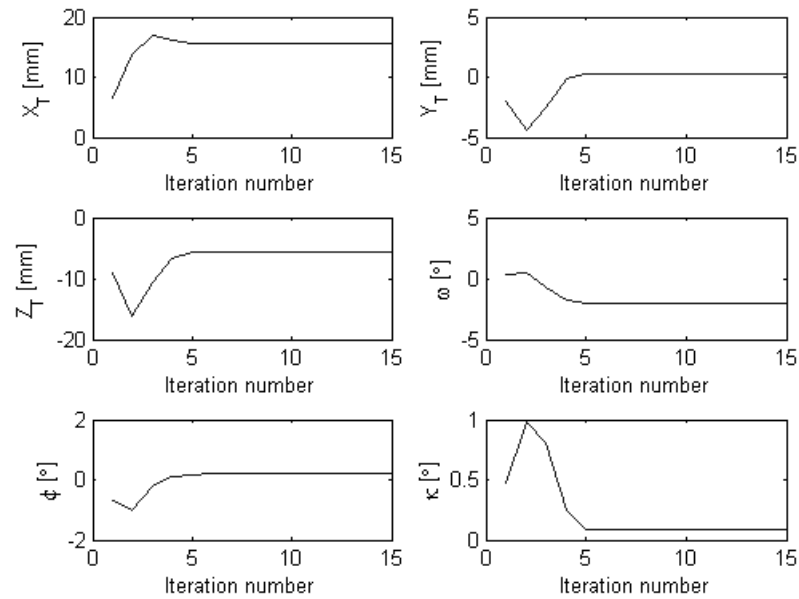


**Figure 5.23** Iterative solution for the transformation parameters in the registration between the July and the October 2009 datasets

### 5.6.3 Test on the coplanarity constraint vs. the modified weight matrix methods

In Chapter Four two approaches for performing pairwise and multiple-surface registration of overlapping point clouds were presented. The two approaches share the same geometric primitives, transformation function and matching strategy, but they differ in the similarity measure. In the coplanarity constraint method, the volume between conjugate points and triangular patches from the overlapping surfaces is minimized. Thus, this is a triangular patch based method. In the modified weight matrix method, for every conjugate point-patch pair, the distance between the point and one of the vertices of the triangular patch is minimized in the direction normal to the patch. Thus, in terms of the implementation, this is a point based method. The previous two experiments only used the coplanarity constraint method so that the results could be comparable to

previously published work. Now, the two approaches were tested with the point clouds from the July and October 2009 datasets in order to verify their equivalency. First, the pairwise registration using the coplanarity constraint and the modified weight matrix methods was performed between all the overlapping surfaces (e.g.  $S_2 \rightarrow S_1$ ,  $S_3 \rightarrow S_2$ ,  $S_3 \rightarrow S_4$ , and  $S_4 \rightarrow S_1$ ) for both datasets. The output from the pairwise registration was the set of transformation parameters between the neighbouring surfaces and the conjugate point-patch pairs in the overlapping regions.

The output from the pairwise-surface registration served as the input for the multiple-surface registration. That is, the final transformation parameters from the pairwise registration were used as the initial transformation parameters for the multiple-surface registration, and the detected conjugate point-patch pairs from the pairwise registration were used for both the coplanarity constraint and modified weight matrix methods for multiple-surface registration. In both datasets, the first surface was chosen as the common reference frame, so its transformation parameters were fixed as zeros for the translations and the rotations. Also, in all cases, the scale for the 3D similarity transformation was fixed as one, so technically a rigid body transformation was implemented. Table 5.18 shows the final transformation parameters and their standard deviations resulted from the multiple-surface registration for the July dataset using the coplanarity constraint method. Table 5.19 shows the same results for the modified weight matrix method. The average normal distances between the matched point-patch pairs for the transformed surfaces were approximately 0.3mm for both methods.

**Table 5.18 Transformation parameters and their standard deviations after multiple surface registration using the coplanarity constraint for the July dataset**

	$X_T$ (mm)	$Y_T$ (mm)	$Z_T$ (mm)	$\omega$ (°)	$\phi$ (°)	$\kappa$ (°)
$S_2$	291.49 $\pm 0.04$	-26.56 $\pm 0.02$	265.07 $\pm 0.02$	93.1381 $\pm 0.1412$	92.8342 $\pm 0.0029$	-87.5881 $\pm 0.1415$
$S_3$	556.89 $\pm 0.02$	-11.38 $\pm 0.02$	-27.01 $\pm 0.03$	8.3861 $\pm 0.0018$	-179.8875 $\pm 0.0056$	2.7046 $\pm 0.0023$
$S_4$	267.31 $\pm 0.05$	14.90 $\pm 0.02$	-290.76 $\pm 0.02$	-89.2218 $\pm 0.0886$	-84.4278 $\pm 0.0029$	-92.1119 $\pm 0.0893$

**Table 5.19 Transformation parameters and their standard deviations after multiple surface registration using the modified weight matrix constraint for the July dataset**

	$X_T$ (mm)	$Y_T$ (mm)	$Z_T$ (mm)	$\omega$ (°)	$\phi$ (°)	$\kappa$ (°)
$S_2$	291.52 $\pm 0.04$	-26.47 $\pm 0.03$	265.08 $\pm 0.02$	92.9025 $\pm 0.1511$	92.8200 $\pm 0.0036$	-87.3628 $\pm 0.1511$
$S_3$	556.91 $\pm 0.03$	-11.31 $\pm 0.03$	-26.93 $\pm 0.05$	8.3631 $\pm 0.0039$	-179.8912 $\pm 0.0081$	2.7045 $\pm 0.0044$
$S_4$	267.36 $\pm 0.05$	15.06 $\pm 0.02$	-290.71 $\pm 0.02$	-89.0894 $\pm 0.0955$	-84.4547 $\pm 0.0034$	-91.9619 $\pm 0.0960$

It could be noticed that, even though quite close, the two sets of transformation parameters were not identical. In order to test their equivalency, the original points of surfaces  $S_2$ ,  $S_3$ , and  $S_4$  were transformed with both sets. Then, the root mean squared error (RMSE) between the resulted pairs of transformed points was calculated. As seen from Table 5.20, the total RMS values were less than the average normal distances of 0.3mm between the transformed surfaces. This means that the RMS values were less than

the measurement noise, and the two sets of transformation parameters were deemed equivalent. Similarly, Table 5.21 shows the final transformation parameters and their standard deviations for the multiple-surface registration using the coplanarity constraint for the October dataset. Table 5.22 shows the same results for the modified weight matrix method. Again, the average normal distances between the transformed surfaces were approximately 0.3mm, and the total RMS values showing the equivalency between the estimated transformation parameters by the coplanarity constraint and the modified weight matrix methods were at the 0.1mm level (see Table 5.23). The only differences between the coplanarity constraint and the modified weight matrix approaches for multiple-surface registration was in terms of computing performance. More specifically, the coplanarity constraint method took about 30 iterations for the a-posteriori variance factor to converge to  $1 \times 10^{-10} \text{mm}^6$ , while the modified weight matrix method took about five iterations for the a-posteriori variance factor to converge to  $1 \times 10^{-15} \text{mm}^2$ . This difference was due to the fact that in the former case the errors minimized were volumetric, while in the latter case the errors were linear.

**Table 5.20 RMSE between point clouds registered by the coplanarity constraint and the modified weight matrix methods for the July dataset**

	<b>RMSE<sub>X</sub></b> <b>(mm)</b>	<b>RMSE<sub>Y</sub></b> <b>(mm)</b>	<b>RMSE<sub>Z</sub></b> <b>(mm)</b>	<b>RMSE<sub>XYZ</sub></b> <b>(mm)</b>
<b>S<sub>2</sub></b>	0.08	0.02	0.09	0.13
<b>S<sub>3</sub></b>	0.03	0.05	0.13	0.14
<b>S<sub>4</sub></b>	0.09	0.20	0.06	0.22

**Table 5.21 Transformation parameters and their standard deviations after multiple surface registration using the coplanarity constraint for the October dataset**

	$X_T$ (mm)	$Y_T$ (mm)	$Z_T$ (mm)	$\omega$ (°)	$\phi$ (°)	$\kappa$ (°)
$S_2$	270.19 $\pm 0.04$	-34.52 $\pm 0.02$	257.08 $\pm 0.02$	-260.4508 $\pm 0.0853$	94.8686 $\pm 0.0030$	268.0451 $\pm 0.0857$
$S_3$	529.99 $\pm 0.02$	-11.16 $\pm 0.02$	-13.09 $\pm 0.03$	12.4952 $\pm 0.0019$	179.6588 $\pm 0.0060$	2.6986 $\pm 0.0025$
$S_4$	259.44 $\pm 0.05$	23.37 $\pm 0.02$	-270.17 $\pm 0.02$	-85.3906 $\pm 0.0709$	-82.4158 $\pm 0.0031$	-90.2563 $\pm 0.0717$

**Table 5.22 Transformation parameters and their standard deviations after multiple surface registration using the modified weight matrix constraint for the October dataset**

	$X_T$ (mm)	$Y_T$ (mm)	$Z_T$ (mm)	$\omega$ (°)	$\phi$ (°)	$\kappa$ (°)
$S_2$	270.24 $\pm 0.04$	-34.64 $\pm 0.03$	256.94 $\pm 0.03$	-260.2167 $\pm 0.0900$	94.8807 $\pm 0.0037$	267.8190 $\pm 0.0902$
$S_3$	529.93 $\pm 0.03$	-11.25 $\pm 0.03$	-13.34 $\pm 0.05$	12.5194 $\pm 0.0041$	179.6655 $\pm 0.0085$	2.7141 $\pm 0.0046$
$S_4$	259.32 $\pm 0.05$	23.46 $\pm 0.02$	-270.33 $\pm 0.02$	-85.4204 $\pm 0.0747$	-82.3940 $\pm 0.0036$	-90.3120 $\pm 0.0755$

**Table 5.23 RMSE between point clouds registered by the coplanarity constraint and the modified weight matrix methods for the October dataset**

	$RMSE_X$ (mm)	$RMSE_Y$ (mm)	$RMSE_Z$ (mm)	$RMSE_{XYZ}$ (mm)
$S_2$	0.07	0.07	0.04	0.11
$S_3$	0.06	0.03	0.08	0.10
$S_4$	0.06	0.03	0.08	0.10

## 5.7 Summary of the experimental results

The experimental results shown in this chapter covered the system calibration, the surface reconstruction and the surface registration procedures. The system calibration included results on the camera calibration, the camera stability analysis, and the estimation of the EOPs. The camera calibration tests consisted of experiments on the type of distortion model, the choice of image space observations and the options for datum definition. It was concluded that a distortion model which only had the first coefficient for radial lens distortion (i.e.  $k_1$ ) was sufficient, and also that when linear features were used together with distance constraints, it was not necessary to use any surveyed target points to define the datum. The IOPs of the cameras were deemed stable after two calibration campaigns, so the cameras were set up on a wooden frame, and together with a projector they were used as one sensor arm. After the EOPs for the cameras were estimated, three different types of objects were reconstructed – a flat metal plate, human faces, and an artificial torso mannequin. The flat metal plate was reconstructed at the sub-millimetre level, the human faces were reconstructed while varying the pattern size, and the torso mannequin was reconstructed with a relative and absolute accuracy of 0.3mm without and with a pattern overlap from a second projector. The torso mannequin experiments also required a registration procedure in order to combine partial pieces of the full surface model into a common reference frame. Two types of similarity measures, namely the coplanarity constraint and the modified weight matrix method, were used for both the pairwise and the multiple surface registration. The results they yielded were equivalent, so in the future any one of them could be used for the registration. Nevertheless, the modified weight matrix method would be the preferred one, because it

takes fewer iterations for the convergence of the transformation parameters, i.e. it is computationally more efficient. At the same time, it is also simpler, because the partial derivatives are easier to implement. All in all, these successful experiments showed that the camera system has the potential to be used for a variety of applications such as change detection, infrastructure deformation monitoring, biomedical imaging, and cultural heritage documentation to name a few.

## **Chapter Six: Conclusions and Recommendations for Future Work**

This thesis started out by defining scoliosis, and some of the risks associated with the disease progression for growing children were described. They included chronic back pain, respiratory problems, and impeded heart function. It was noted that an early detection of abnormal spine curvature is crucial so that the disease could be monitored closely, and an adequate treatment could be assigned to the patient. Then, it was pointed out that the current methodologies for scoliosis assessment and monitoring employ x-ray imaging, which over time exposes the patients to a significant amount of ionizing radiation leading to an increased risk of cancer. Since there is a high correlation between the internal spine curvature and the torso surface deformation, quantifying the scoliotic deformity of the torso surface is an alternative method for scoliosis assessment and monitoring. Some of the most recent work on establishing this correlation was published by Swanson (2008). This was why a brief review of some of the current commercially available systems for 3D reconstruction was carried on. However, it was decided that none of these systems were adequate for torso surface measurements, because they were too expensive, not accurate enough, or too slow in order to be able to measure kinematic objects. On the other hand, off-the-shelf digital cameras are now readily available at low cost. Moreover, they could be rigorously modelled to achieve optimal accuracy, and they could also be set at a fast shutter speed to avoid any motion problems. This was why this research proposed a photogrammetric system as a radiation-free replacement of x-ray imaging for providing 3D surface models of scoliotic torsos. In addition, the system must be designed in such a way that it could reconstruct surfaces with homogenous texture and

entire 3D objects. Ideally, it should also be fairly automated so that the final product could be delivered as quickly as possible, and finally, it should be flexible enough to be used for other 3D reconstruction applications. The ground work on this project, i.e. the initial experiments using a single camera for the proof of concept were published by Chang (2008).

The proposed system is based on a low-cost multiple-camera and multiple-projector setup. The prerequisites for optimal functionality include system calibration (i.e. camera calibration, camera stability analysis and exterior orientation parameter determination), camera synchronization and pattern projection. The processing procedures include semi-automated surface reconstruction, and fully automated surface registration, where the only manual involvement in the surface reconstruction is selecting a region of interest for the corner detection and matching. The performance of the implemented sensor arm as part of the designed system was assessed by repeatedly reconstructing a flat metal plate, two human faces, and a full 360° model of an artificial torso mannequin. The final reconstructed models exhibited sub-millimetre relative and absolute accuracy, which was at the desired quality level. Currently, the pairwise surface registration seems to perform quite well, but the multiple surface registration is still highly recommended so that the registration quality of the final torso model could be trusted in cases of less overlap between the involved surfaces.

The main contributions of the work presented here included improvements in the system calibration, the data collection, the processing, and the results assessment. In terms of the system calibration and the data collection, the major contribution was the actual implementation of one of the sensor arms in the proposed system, i.e. the camera

calibration, the camera stability analysis, the setup, and the operation of multiple cameras. In terms of the data processing, the focus was on improving the system automation and reliability. This was why the hierarchical image matching algorithm, and the pairwise and multiple surface registration techniques using the modified weight matrix method were introduced in the processing workflow. Finally, in terms of improvements in the results assessment, the 1025-set of FaroArm control points were collected, and a repeatability study was also performed.

## 6.1 Conclusions

There were three findings during the camera calibration experiments. The first one was that it was not necessary to solve for all the six lens distortion parameters for the tested camera. This was concluded, because estimating only the first coefficient for radial lens distortion yielded an adequate set of IOPs, i.e. the bundle adjustment had sub-pixel level precision in image space, and sub-millimetre accuracy in object space. The second point was that adding linear features to the calibration procedure improved the precision of the estimated IOPs due to increased redundancy. The last finding was that whether control points or distance constraints were used to define the datum, the output IOP sets were equivalent, especially if linear features were used as observations. This was to say that including linear features in the bundle adjustment with self-calibration improved the robustness of the solution against the datum definition procedure. Thus, it was concluded that the most practical way to do camera calibration as far as choices for a distortion model, image space observations and datum definition, was to solve only for  $k_1$  as

opposed to all the lens distortion parameters, use linear features in addition to points, and use distance constraints as opposed to control points, respectively.

During the data processing, there was a new implementation of a hierarchical image matching procedure. Traditionally, hierarchical image matching for aerial photographs is done by resampling the images from coarse to fine resolution. In this case, the hierarchical image matching was carried out for a close range photogrammetry application. It was done by controlling the density of the corner detection at every matching iteration, and by using a look-up table for the x-parallax.

There was another finding during the comparative analysis of the coplanarity constraint and the modified weight matrix method for irregular point cloud registration. The two methods produced equivalent results, however, the modified weight matrix method was more efficient in terms of computing performance. This was because the coplanarity constraint method was a point-patch approach and the errors that were minimized were volumetric, while the modified weight matrix was effectively a point-to-point approach and the errors that were minimized were linear.

In terms of overall conclusions, the experimental results were quite encouraging, and the proposed system is thought to be sufficiently accurate for clinical applications. Also, since it is economical, it has the potential to be used for scoliosis assessment and monitoring. In addition, since the relative orientation for the cameras in each sensor arm is computed by simply using a target board with measured distances, this part of the system calibration could easily be done by the end user. The proposed system could also be modified so that it could be used for other applications such as structural deformation monitoring or cultural heritage documentation.

## **6.2 Recommendations for future work**

All in all, the implemented system met all original objectives, except that processing the data takes longer than desired. Thus, current work is focusing on optimizing the system, i.e. speeding up the required time for processing. Future work will include building the full four sensor arm prototype of the proposed system, and performing experiments on real subjects in a clinical environment after receiving ethics approval. Also, there will be more involvement in the actual analysis of the reconstructed torso for the purpose of monitoring the disease progression. For example, indices which quantify the torso surface asymmetry well enough to be able to estimate the degree of spinal deformity will be worked on. Finally, the system will be used for the deformation monitoring of beams and trusses during static and dynamic load testing.

## References

- Ackermann, F. and Hahn, M., 1991. Image pyramids for digital photogrammetry. In: H. Ebner, D. Fritsch and C. Heipke (Editors), *Digital Photogrammetric Systems*. Wichmann Verlag, Karlsruhe, Germany, pp. 43-58.
- Adair, V., van Wijk, M.C. and Armstrong, G.W.D., 1977. Moiré Topography in Scoliosis Screening. *Clinical Orthopaedics and Related Research*, 129(6): 165-171.
- Adams, W., 1882. Lectures on the pathology and treatment of lateral and other forms of curvature of the spine. J & A Churchill & Sons, London, Lecture 4.
- Aldelgawy, M., Detchev, I. and Habib, A., 2008. Alternative Procedures for the Incorporation of LiDAR-Derived Linear and Areal Features for Photogrammetric Geo-referencing. Proceedings of the ASPRS 2008 Annual Conference, Portland, Oregon, April 28 - May 2.
- Besl, P.J. and McKay, N.D., 1992. A Method for Registration of 3-D Shapes. *IEEE Transactions on Pattern Analysis and Machine Intelligence*, 14(2): 239-256.
- Blais, F., 2004. Review of 20 years of range sensor development. *Journal of Electronic Imaging*, 13(1): 231-240.
- Brown, D.C., 1971. Close-Range Camera Calibration. *Photogrammetric Engineering & Remote Sensing*, 37(8): 855-866.
- Brown, L.G., 1992. A Survey of Image Registration Technique. *ACM Computing Surveys*, 24(2): 325-376.

- Brown, R.H., Burstein, A.H., Nash, C.L. and Schock, C.C., 1976. Spinal Analysis Using a Three-Dimensional Radiographic Technique. *Journal of Biomechanics*, 9(6): 355-365.
- Bunnell, W.P., 1984. An objective criterion for scoliosis screening. *Journal of Bone and Joint Surgery*, 66-A(9): 1381-1387.
- Chang, Y.-C., 2008. A Photogrammetric System for 3D Reconstruction of a Scoliotic Torso. MSc Thesis, University of Calgary, Calgary, 192 pp.
- Chang, Y.-C., Detchev, I. and Habib, A., 2009. A Photogrammetric System for 3D Reconstruction of a Scoliotic Torso. Proceedings of the ASPRS 2009 Annual Conference, Baltimore, Maryland, March 8 - 13.
- Chen, Y. and Medioni, G., 1992. Object modelling by registration of multiple range images. *Image and Vision Computing*, 10(3): 145-155.
- Cheng, R.W.T. and Habib, A.F., 2007. Stereo photogrammetry for generating and matching facial models. *Journal of Optical Engineering*, 46(6): 067203.
- Cho, W., Schenk, T. and Madani, M., 1992. Resampling digital imagery to epipolar geometry. *International Archives of Photogrammetry and Remote Sensing*, 29(B3): 404-408.
- Chong, A.K., Milburn, P. and Voert, M.t., 2009. High-accuracy Photogrammetric Technique for Human Spine Measurement. *The Photogrammetric Record*, 24(127): 264-279.
- Clarke, T.A. and Fryer, J.G., 1998. The Development of Camera Calibration Methods and Models. *The Photogrammetric Record*, 16(91): 51-66.

- Cobb, J.R., 1948. Outline for the study of scoliosis, instructional course lectures. *American Academy of Orthopaedic Surgeons, Ann Arbor, J. W. Edwards*, 5: 261-275.
- Côté, P.D.C., Kreitz, B.G., Cassidy, J.D., Dzus, A.K. and Martel, J., 1998. A Study of the Diagnostic Accuracy and Reliability of the Scoliometer and Adam's Forward Bend Test. *Spine*, 23(7): 796-802.
- D'Apuzzo, N., 2002. Surface measurement and tracking of human body parts from multi-image video sequences. *ISPRS Journal of Photogrammetry & Remote Sensing*, 56(5-6): 360-375.
- D'Oswaldo, F., Schierano, S. and Cisotti, C., 2002. The evaluation of the spine through the surface. The role of surface measurements in the evaluation and treatment of spine diseases in young patients. *Europa Medicophysica*, 38(3): 147-152.
- Dawson, E.G., Knopf, M.A., Purcell, G., Kabo, J.M., Kanim, L.E.A. and Burt, C., 1993. Optoelectronic Evaluation of Trunk Deformity in Scoliosis. *Spine*, 18(3): 326-331.
- Detchev, I., Ebeling, A. and Habib, A., 2010. Comparative Analysis of Alternative In-Door Calibration Techniques for Off-The-Shelf Digital Cameras. Proceedings of the ASPRS 2010 Annual Conference, San Diego, California, April 26-30.
- Doody, M.M., Lonstein, J.E., Stovall, M., Hacker, D.G., Luckyanov, N. and Land, C.E., 2000. Breast Cancer Mortality after Diagnostic Radiography: Findings from the U.S. Scoliosis Cohort Study. *Spine*, 25(16): 2052-2063.

- Drerup, B. and Hierholzer, E., 1994. Back shape measurement using video rasterstereography and three-dimensional reconstruction of spinal shape. *Clinical Biomechanics*, 9(1): 28-36.
- Fonseca, L.M.G. and Manjunath, B.S., 1996. Registration Techniques for Multisensor Remotely Sensed Imagery. *Photogrammetric Engineering & Remote Sensing*, 62(9): 1049-1056.
- Förstner, W., Wrobel, B., Paderes, F., Craig, R., Fraser, C. and Dolloff, J., 2004. Analytical Photogrammetric Operations. In: J.C. McGlone, E.M. Mikhail and J. Bethel (Editors), *Manual of Photogrammetry*. American Society for Photogrammetry and Remote Sensing, Bethesda, Maryland, pp. 1151.
- Fraser, C.S., 1997. Digital camera self-calibration. *ISPRS Journal of Photogrammetry & Remote Sensing*, 52(4): 149-159.
- Frobin, W. and Hierholzer, E., 1982. Analysis of Human Back Shape Using Surface Curvatures. *Journal of Biomechanics*, 15(5): 379-390.
- Fröhlich, C. and Mettenleiter, M., 2004. Terrestrial Laser Scanning - New Perspectives in 3D Surveying. *International Archives of the Photogrammetry, Remote Sensing and Spatial Information Sciences*, XXXVI(8/W2): 7-13.
- Goldberg, M.S., Poitras, B., Mayo, N.E., Labelle, H., Bourassa, R. and Cloutier, R., 1988. Observer Variation in Assessing Spinal Curvature and Skeletal Development in Adolescent Idiopathic Scoliosis. *Spine*, 13(12): 1371-1377.
- Habib, A., Datchev, I. and Bang, K.I., 2010a. Comparative Analysis of Two Approaches for Multiple-Surface Registration of Irregular Point Clouds. *International*

*Archives of the Photogrammetry, Remote Sensing and Spatial Information Sciences*, Vol. XXXVIII(part 1).

Habib, A., Jarvis, A., Detchev, I., Stensaas, G., Moe, D. and Christopherson, J., 2008.

Standards and Specifications for the Calibration and Stability of Amateur Digital Cameras for Close-Range Mapping Applications. *The International Archives of the Photogrammetry, Remote Sensing and Spatial Information Sciences*, Vol. XXXVII(Part B1): 1059-1064.

Habib, A.F., Bang, K.I., Kersting, A.P. and Lee, D.-C., 2009. Error budget of LiDAR

systems and quality control of the derived data. *Photogrammetric Engineering & Remote Sensing*, 75(9): 1093-1108.

Habib, A.F., Kersting, A.P., Bang, K.I. and Lee, D.-C., 2010b. Alternative

Methodologies for the Internal Quality Control of Parallel LiDAR Strips. *IEEE Transactions on Geoscience and Remote Sensing*, 48(1): 221-236.

Habib, A.F. and Morgan, M.F., 2003. Automatic calibration of low-cost digital cameras.

*Journal of Optical Engineering*, 42(4): 948-955.

Habib, A.F. and Morgan, M.F., 2005. Stability analysis and geometric calibration of off-

the-shelf digital cameras. *Photogrammetric Engineering & Remote Sensing*, 71(6): 733-741.

Habib, A.F., Morgan, M.F. and Lee, Y.-R., 2002. Bundle Adjustment with Self-

Calibration Using Straight Lines. *The Photogrammetric Record*, 17(100): 635-650.

Habib, A.F., Pullivelli, A.M., Mitishita, E.A., Ghanma, M. and Kim, E.-M., 2006.

Stability Analysis of Low-cost Digital Cameras for Aerial Mapping Using

- Different Georeferencing Techniques. *The Photogrammetric Record*, 21(113): 29-43.
- Habib, A.F., Pullivelli, A.M. and Morgan, M.F., 2005. Quantitative measures for the evaluation of camera stability. *Journal of Optical Engineering*, 44(3): 033605.
- Harris, C. and Stephens, M., 1988. A combined corner and edge detector. Proceedings of the 4th Alvey Vision Conference, Manchester, UK,
- Hindmarsh, J., Larsson, J. and Mattson, O., 1980. Analysis of Changes in the Scoliotic Spine Using a Three-Dimensional Radiographic Technique. *Journal of Biomechanics*, 13(3): 279-290.
- Howell, F.R. and Dickson, R.A., 1989. The Deformity of Idiopathic Scoliosis Made Visible by Computer Graphics. *Journal of Bone and Joint Surgery*, 71-B(3): 399-403.
- InSpeck, 2009. 3D Mega Capturor II. InSpeck Inc., Montréal, Québec, pp. 1.
- Ishida, I., Suzuki, S., Imai, S. and Mori, Y., 1982. Scoliosis evaluation utilising truncal cross-sections. *Medical and Biological Engineering and Computing*, 20(2): 181-186.
- Jaremko, J.L., Delorme, S., Dansereau, J., Labelle, H., Ronsky, J., Poncet, P., Harder, J., Dewar, R.D. and Zernicke, R.F., 2000. Use of Neural Networks to Correlate Spine and Rib Deformity in Scoliosis. *Computer Methods in Biomechanics and Biomedical Engineering*, 3(3): 203-213.
- Jaremko, J.L., Poncet, P., Ronsky, J., Harder, J., Dansereau, J., Labelle, H. and Zernicke, R.F., 2001. Estimation of Spinal Deformity in Scoliosis from Torso Surface Cross Sections. *Spine*, 26(14): 1583-1591.

- Jaremko, J.L., Poncet, P., Ronsky, J., Harder, J., Dansereau, J., Labelle, H. and Zernicke, R.F., 2002a. Comparison of Cobb Angles Measured Manually, Calculated from 3-D Spinal Reconstruction, and Estimated from Torso Asymmetry. *Computer Methods in Biomechanics and Biomedical Engineering*, 5(4): 277-281.
- Jaremko, J.L., Poncet, P., Ronsky, J., Harder, J., Dansereau, J., Labelle, H. and Zernicke, R.F., 2002b. Generic Algorithm - Neural Network Estimation of Cobb Angle from Torso Asymmetry in Scoliosis. *Journal of Biomechanical Engineering*, 124(5): 496-503.
- Jaremko, J.L., Poncet, P., Ronsky, J., Harder, J., Dansereau, J., Labelle, H. and Zernicke, R.F., 2002c. Indices of torso asymmetry related to spinal deformity in scoliosis. *Clinical Biomechanics*, 17(8): 559-568.
- Kane, W.J., 1977. Scoliosis Prevalence: A Call for a Statement of Terms. *Clinical Orthopaedics and Related Research*, 126: 43-46.
- Kotwicki, T., 2008. Evaluation of scoliosis today: Examination, X-rays and beyond. *Disability & Rehabilitation*, 30(10): 742-751.
- Kratky, V., 1975. Analytical X-Ray Photogrammetry in Scoliosis. *Photogrammetria*, 31(6): 195-210.
- Kraus, K., 1993. Photogrammetry, Volume 1: Fundamentals and Standard Processes. Ferd. Duemmlers Verlag, Bonn, 397 pp.
- Kraus, K., 1997. Photogrammetry, Volume 2: Advanced Methods and Applications. Ferd. Duemmlers Verlag, Bonn, 466 pp.
- Leica, 2009. Leica HDS6100: Latest generation of ultra-high speed laser scanner. Leica Geosystems AG, Heerbrugg, Switzerland, pp. 4.

- Levy, A.R., Goldberg, M.S., Mayo, N.E., Hanley, J.A. and Poitras, B., 1996. Reducing the Lifetime Risk of Cancer from Spinal Radiographs among People with Adolescent Idiopathic Scoliosis. *Spine*, 21(13): 1540-1547.
- Lewis, J. and Waizenegger, C., 2010. SR4000 Data Sheet. MESA Imaging AG, Zurich, Switzerland, pp. 8.
- Light, D.L., 1992. The New Camera Calibration System at the U.S. Geological Survey. *Photogrammetric Engineering & Remote Sensing*, 58(2): 185-188.
- Minolta, 2007. VIVID 9i Non-Contact 3D Digitizer. Konica Minolta Sensing, Inc., Osaka, Japan, pp. 8.
- Mitchell, H.L. and Newton, I., 2002. Medical photogrammetric measurement: overview and prospects. *ISPRS Journal of Photogrammetry & Remote Sensing*, 56(5-6): 286-294.
- Montgomery, F. and Willner, S., 1993. Screening for idiopathic scoliosis: Comparison of 90 cases shows less surgery by early diagnosis. *Acta Orthopaedica Scandinavica*, 64(4): 456-458.
- Morgan, M.F., Kim, K.-O., Jeong, S. and Habib, A.F., 2006. Epipolar resampling of space-borne linear array scanner scenes using parallel projection. *Photogrammetric engineering and remote sensing*, 72(11): 1255-1263.
- Morrissy, R.T., Goldsmith, G.S., Hall, E.C., Kehl, D. and Cowie, G.H., 1990. Measurement of Cobb Angle on Radiographs of Patients Who Have Scoliosis. Evaluation of Intrinsic Error. *Journal of Bone and Joint Surgery*, 72(3): 320-327.
- Nachemson, A., 1968. A Long Term Follow-Up Study of Non-Treated Scoliosis. *Acta Orthopaedica Scandinavica*, 39(4): 466-476.

- Okutomi, M. and Kanade, T., 1993. A Multiple-Baseline Stereo. *IEEE Transactions on Pattern Analysis and Machine Intelligence*, 15(4): 353-363.
- Patias, P., 2002. Medical imaging challenges photogrammetry. *ISPRS Journal of Photogrammetry & Remote Sensing*, 56(5-6): 295-310.
- Petrie, G. and Toth, C.K., 2009. Introduction to Laser Ranging, Profiling, and Scanning. In: J. Shan and C.K. Toth (Editors), *Topographic Laser Ranging and Scanning: Principles and Processing*. CRC Press, Taylor & Francis Group, Boca Raton, Florida, pp. 590.
- Polhemus, 2008. *FastSCAN Cobra & Scorpion: The Fast and Easy Digital Scanner*. Polhemus, Colchester, Vermont, pp. 2.
- Poncet, P., Delorme, S., Ronsky, J.L., Dansereau, J., Clynch, G., Harder, J., Dewar, R.D., Labelle, H., Gu, P.-H. and Zernicke, R.F., 2000. Reconstruction of Laser-scanned 3D Torso Topography and Stereoradiographical Spine and Rib-cage Geometry in Scoliosis. *Computer Methods in Biomechanics and Biomedical Engineering*, 4(1): 59-75.
- Remondino, F., 2004. 3-D reconstruction of static human body shape from image sequence. *Computer Vision and Image Understanding*, 93(1): 65-85.
- Remondino, F. and El-Hakim, S., 2006. Image-Based 3D Modelling: A Review. *The Photogrammetric Record*, 21(115): 269-291.
- Remondino, F. and Fraser, C., 2006. Digital Camera Calibration Methods: Considerations and Comparisons. Proceedings of the ISPRS Commission V Symposium "Image Engineering and Vision Metrology", Dresden, Germany, September 25-27.

- Roach, J.W., 1999. Adolescent idiopathic scoliosis. *Orthopedic Clinics of North America*, 30(3): 353-365.
- Robu, D., 2006. Assessment of 3D reconstruction of scoliotic human torso using optical imaging techniques. MSc Thesis, University of Calgary, Calgary, 187 pp.
- Rogala, E.J., Drummond, D.S. and Gurr, J., 1978. Scoliosis: Incidence and Natural History. A Prospective Epidemiological Study. *Journal of Bone and Joint Surgery*, 60-A(2): 173-176.
- Schenk, T., 1999. Digital photogrammetry. TerraScience, Laurelville, Ohio, 422 pp.
- Siebert, J.P. and Marshall, S.J., 2000. Human Body 3D Imaging by Speckle Texture Projection Photogrammetry. *Sensor Review*, 20(3): 218-226.
- Smith, W.E., Vakil, N. and Maislin, S.A., 1992. Correction of Distortion in Endoscopic Images. *IEEE Transactions on Medical Imaging*, 11(1): 117-122.
- Suh, C.H., 1974. The Fundamentals of Computer Aided X-Ray Analysis of the Spine. *Journal of Biomechanics*, 7(2): 161-169.
- Swanson, S.L., 2008. Estimating Scoliosis Progression from Three Dimensional Torso Shape. MSc Thesis, University of Calgary, Calgary, 164 pp.
- Torell, G., Nordwall, A. and Nachemson, A., 1981. The Changing Pattern of Scoliosis Treatment Due to Effective Screening. *Journal of Bone and Joint Surgery*, 63-A(3): 337-341.
- Trimble, 2009. Trimble GX 3D Scanner Datasheet. Trimble Navigation Limited, Dayton, Ohio, pp. 2.
- Turner-Smith, A.R., 1988. A Television/Computer Three-Dimensional Surface Shape Measurement System. *Journal of Biomechanics*, 21(6): 515-529.

- Turner-Smith, A.R., Harris, J.D., Houghton, G.R. and Jefferson, R.J., 1988. A Method for Analysis of Back Shape in Scoliosis. *Journal of Biomechanics*, 21(6): 497-509.
- Weinstein, S.L., 1999. Natural History. *Spine*, 24(24): 2592-2600.
- Weisz, I., Jefferson, R.J., Turner-Smith, A.R., Houghton, G.R. and Harris, J.D., 1988. ISIS Scanning: A Useful Assessment Technique in the Management of Scoliosis. *Spine*, 13(4): 405-408.
- Willner, S., 1979. Moiré Topography for the Diagnosis and Documentation of Scoliosis. *Acta Orthopaedica Scandinavica*, 50(3): 295-302.